Development of Porous Graphene Composites and Study on Ionic Behaviors in Energy Storage Device

Li Jing

February 2018

Development of Porous Graphene Composites and Study on Ionic Behaviors in Energy Storage Device

Li Jing

Doctoral Program in Materials Science and Engineering

Submitted to the Graduate School of
Pure and Applied Sciences
in Partial Fulfillment of the Requirements
for the Degree of Doctor of Philosophy in
Engineering

at the
University of Tsukuba

Abstract

Graphene, a kind of materials with hexagonal lattice of sp^2 carbon atoms covalently bonded along two plane directions, is a desired option for the electrode in supercapacitors since its excellent conductivity and large specific surface area. However, the re-stacking between graphene layers lead to smaller specific surface area than the ideal situation. This problem has limited the development of graphene supercapacitors with high energy density, which is proportional to the specific capacitance of electrode materials. Therefore, porous graphene composites, such as carbon nanotube (CNT)/graphene composites are designed to solve the problem by preventing the formation of re-staking.

In the present study, oxidized multi-wall carbon nanotube (MWNT) is preferred as spacers between graphene oxide layers, which are the precursors of graphene materials. The oxidized treatment is used to eliminate the aggregation of CNTs and improve the interface coupling between CNTs and graphene oxide (GO) before reduction. We have synthesized CNT/graphene composites, namely reduced product of oxidized MWNT/GO (RMGO) composites, with different pore structures by adjusting the ratio of oxidized MWNT to GO. As a result, the specific surface area of RMGO composites has increased by 1.5 times compared with graphene synthesized by the same method. The performance of materials in supercapacitors is characterized in EMI-BF_4, a room temperature ionic liquid. The specific capacitance (C) of RMGO with 20% CNTs is 206 F g^{-1} with the best rate capability (79%) at 3.7 V. The value of C has increased by 61% compared with bared graphene. It is worth noting that RMGO-6 doesn't show the largest C even though it has the largest A of 742 m^2 g^{-1}. Considering many reported discussions, we have made a hypothesis that pores with different sizes have different contributions to specific capacitance.

To address this issue, we have taken two kinds of fitting method to analyze the relationship between specific capacitance and specific surface area of different pores. In this study, we have chosen reduced oxidized MWNT/GO composites (RMGO), the materials we have discussed in the previous chapter, as electrode materials and an ionic liquid, 1-ethyl-3-methylimidazolium tetrafluoroborate (EMI-BF_4), as the electrolyte. The results of analysis indicate that pores with radii in the range of two to three times of cation and anion-pairs are the most efficient pores for both cations and anion-pairs. It is due to the changed ion packing configuration in different pores, which is related to the stronger ion-ion correlation in ionic liquids. In addition, pores smaller than the ion sizes could hinder the utilization of larger pores when the ink-bottle structure is present.

Besides enlarging specific capacitance, increase the working voltage (U) is another approach to enhance the energy density. Using an electrolyte with a wider electrochemical stability window is a direct way to reach a larger U. In this study, we has preferred a kind of ionic liquid, 1-methyl-1-propylpiperidinium bis (trifluoromethyl sulfonyl) imide (MPPp-TFSI), since its electrochemical stability window is larger than the ionic liquids, 1-ethyl-3-methylimidazolium tetrafluoroborate (EMI-BF_4) mentioned above. Since ionic behaviors in pores would be different when voltage increases according to several reported discussion, we have taken multiple-linear fittings between specific surface area of different pores and specific capacitance of when supercapacitors are charged to 4.0V and 4.5V respectively. According to the fitting results, the most efficient pores for cations are pores (0.68nm $< r <$ 2.5nm) while those are pores (0.96nm $< r <$ 2.5nm) for anions. It is due to the existence of ion-clusters in MPPp-TFSI electrolyte due to its high viscosity. In addition, more ions can be squeezed into accessible pores by increased voltage. And for anions, some smaller pores can be expanded by anion-clusters forced by higher voltage. The two behaviors above are the reasons for the larger specific capacitance at the higher applied voltage of supercapacitors.

Based on the ionic behaviors figured out above, we have improved the pore structure of CNT/graphene by eliminating the pores accessible for neither cations nor anions, which are supposed to have negative effect on specific capacitance. It is realized by the better dispersion of CNTs in water by using a surfactant. In addition, a greater working voltage has been achieved by the design of an asymmetric configuration of supercapacitors in ionic liquid MPPp-TFSI. When the mass ratio of negative electrode to positive electrode is set to 1.5, the supercapacitor could be charged to 4.7 V and a high energy density of 118 Wh kg^{-1} is obtained at a charging/discharging current density of 1.0 A g^{-1}.

Contents

Chapter 1

Chapter 2

Chapter 3

Chapter 4

Chapter 8

Chapter 1

Introduction

1.1. Supercapacitors

Nowadays, to meet the growing energy demand and issues of the environment, a lot of energy systems have been developed to realize large energy storage and long lifetime without damages on the environment. To evaluate the performance of electrical storage devices, two quantities are commonly used: the energy density and power density. The high energy density will lead to the long service time. And the high power density means the short charging time. Fig. 1 shows the performance comparison of various energy-storing devices. Compared with other electric energy storage devices, the superiorities of supercapacitors are the high power density and long lifetime [1]. However, its energy density has limited the wider applications. So what we are focus on is to enhance the energy density of supercapacitors while keep its high power density with some good electrode materials and suitable electrolytes.

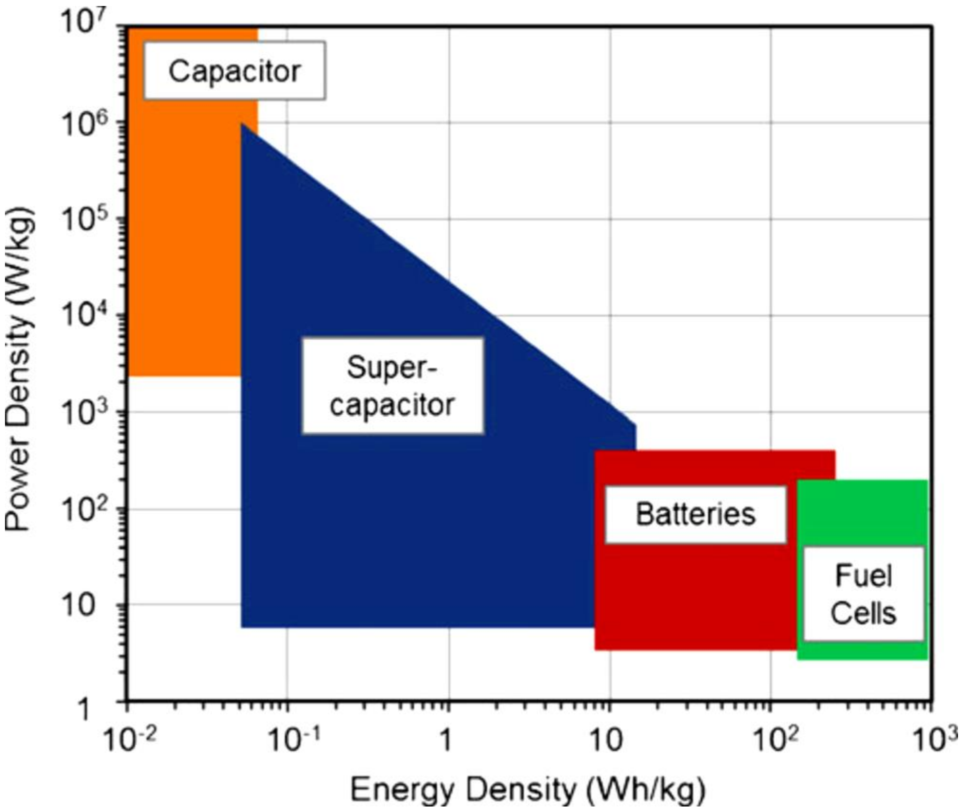

Fig.1 Performance comparison of various energy-storage devices [1].

According to the mechanism of storage of electric energy, the supercapacitors are mainly classified into three types: electrostatic double-layer capacitors (EDLC) and pseudo-capacitors. The details of the three types are discussed in details below.

1.1.1 Electrostatic Double-Layer Capacitors (EDLC)

A basic device of EDLC consists of two electrodes, the electrolyte, and a separator that electrically isolates the two electrodes (Fig. 2). The mechanism of storage of electric energy in EDLC is shown in Fig 2. When the supercapacitor is charged, electric charges is accumulated on the electrode surfaces, and electrolyte ions with counterbalancing charge are built up on the electrolyte side in order to meet electro-neutrality [1, 2]. And the adsorbed ions will be released back to electrolytes when the supercapacitor is discharged. This layer of electric charges and the layer of ions at the interface can be treated as an electrical double-layer. The physical adsorption and desorption of ions are non-faradaic processes, which means no charges are transferred across interface between electrode and electrolyte. Therefore, the charging-discharging process in EDLC is a faster one compared with faradic processes in other electric storage systems, which leads to its higher power density.

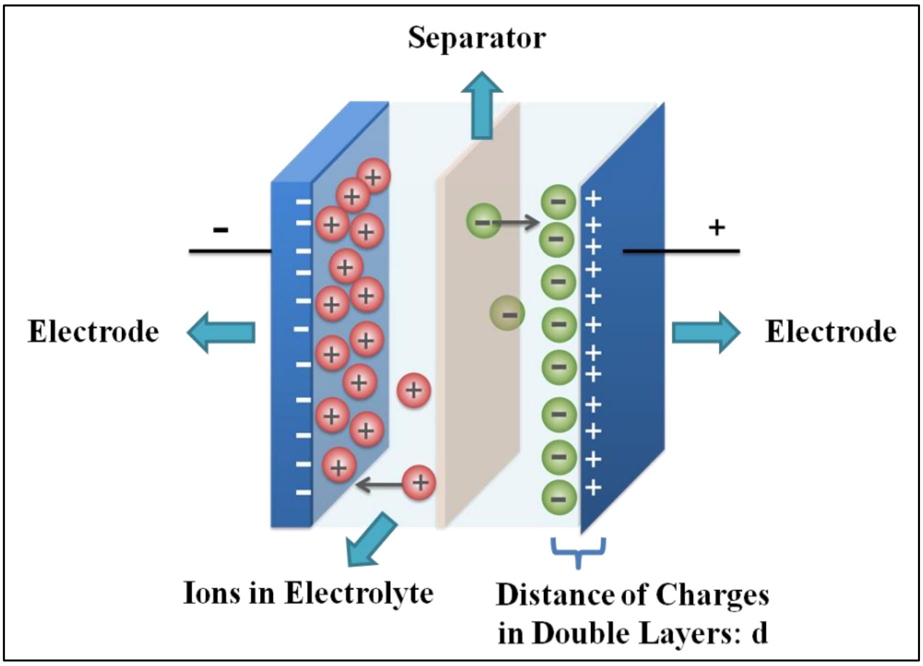

Fig. 2 Structure of electrostatic double-layer capacitors

Since each double-layer structure at the interface can be considered as a capacitor with two parallel plates as electrodes. The capacitance in each double-layer can be expressed as Eqn. 1: $C_{DL} = \frac{\varepsilon A_{Interface}}{d}$, where $A_{Interface}$ is the area of the interface between electrode and electrolyte which can adsorb and desorb ions, ε is the dielectric constant of the electrolyte and d is the distance of charges in the double-layer. In EDLC, the value of d is extremely since it is approximately the radius of the ion or the solvated ion in the range from several angstroms to one nanometer [1-3]. Hence the capacitance is extremely large according to Eqn 1. That’s why it is called the “super” capacitor.

To provide a basis for comparison between different electrode materials, it has become a common practice to provide a specific capacitance of one single electrode, C (F g^{-1}). Therefore, the Eqn 1 can be rewritten as Eqn. 2: $C = \frac{\varepsilon A}{d}$, where A is the specific surface area of electrode materials. In case of a symmetric system, where both electrodes are equal in mass and material, Eqn. 3 can be used to calculate the specific capacitance:

$$C = 4 \cdot \frac{C_{Supercapacitor}}{m} \tag{3}$$

where m is the total mass of active material. The factor 4 is related to normalization to the mass of one electrode for the two identical capacitors in series. It is deduced in details as following.

The relationship between the overall capacitance and the specific capacitance on two electrodes in series is as below:

$$\frac{1}{C_{Supercapacitor}} = \frac{1}{C_1 m_1} + \frac{1}{C_2 m_2} \tag{4}$$

where C_1, C_2 are specific capacitance on the two electrode and m_1, m_2 are mass of the two electrodes. If both specific capacitance and mass are equal for two electrodes, Eqn. 4 can be rewritten as below and it is obvious that Eqn. (5c) is equivalent to Eqn. (3).

$$C = C_1 = C_2 \tag{5a}$$

$$m_1 = m_2 = \frac{m}{2} \tag{5b}$$

$$\frac{1}{C_{Supercapacitor}} = \frac{4}{Cm} \tag{5c}$$

In addition, the stored energy density E (Wh kg^{-1}) in a supercapacitor is given by Eqn.6 :

$$E = \frac{C_{Supercapacitor} \cdot U^2}{2 \cdot m \cdot 3600} = \frac{C \cdot U^2}{8 \cdot 3600} \tag{6}$$

where U (V) is the voltage across the positive and negative electrode. The maximum power density (W kg^{-1}) also depends on the maximal applicable voltage and is given by Eqn.7:

$$P = \frac{U^2}{4 \cdot m \cdot ESR} \tag{7}$$

where ESR (Ω) is the equivalent series resistance of the system. The ESR corresponds to the sum of the resistances related to the ionic resistance of the electrolyte impregnated in the separator, the electronic resistance of electrodes, and interface resistances between electrodes and current collectors [3].

1.1.2 Pseudo-capacitors

Different with EDLC, fast and reversible faradic processes take place in pseudo-capacitors. According to different electrode materials, these faradaic processes are generally classified into two types: redox reactions of transition metal oxides and electrochemical doping-dedoping in conductive polymers [4-6]. It has been reported by several literatures that pseudo-capacitors can provide larger specific capacitance than EDLC since the electrochemical processes occur both on the surface and in the bulk near the surface of the electrode materials [7, 8]. This feature provides more sites to store charges.

However, it should be mentioned that the pseudo-capacitors usually suffer from worse rata capability than EDLC [7]. The reason is that the passage of charges across the interface between electrode and electrolyte in faradaic processes requires more time than the physical adsorption-desorption process. As a result, the capacitance has a larger decline due to increased current density since there is not enough time for faradic processes during faster charging-discharging process. In addition, the power density in pseudo-capacitors is also smaller than that in EDLC, which is also attributed to the slower charge transfer across the interface between the electrode and the electrolyte [7, 8]. Besides, the pseudo-capacitors are more likely to lack stability during cycling due to some irreversible side reactions or the damage of structures due to redox reactions [9, 10].

1.1.3 Hybrid Capacitors.

The hybrid capacitors have attracted a lot of attentions since they are expected to make use of both advantages of the two kinds of supercapacitors discussed above [11, 12]. In this type of supercapacitors, one electrode behaviors as the EDLC while faradaic processes take place on the other at the same time. However, the relative complex configuration attribute to different materials and mechanism makes it more difficult for large-scale production.

1.2. Electrode Materials of EDLC —— Porous Carbon Materials

According to Eqn. 6, there are two apparent strategies have been explored intensively to address the issue of limited energy density. One is enlarging specific capacitance (C) and another is increasing working voltage (U). The previous one is mainly related to the electrode materials. As shown in Fig.2, porous carbon material has been recognized as an attractive electrode due to its good conductivity and large specific surface area. We will introduce several typical porous carbon materials in details. To describe the pores in brief, the pores are generally classified into three type: micropores (diameter is smaller than 2 nm), mesopores (diameter is in the range from 2 to 50 nm), and macropores (diameter is larger than 50 nm) [2].

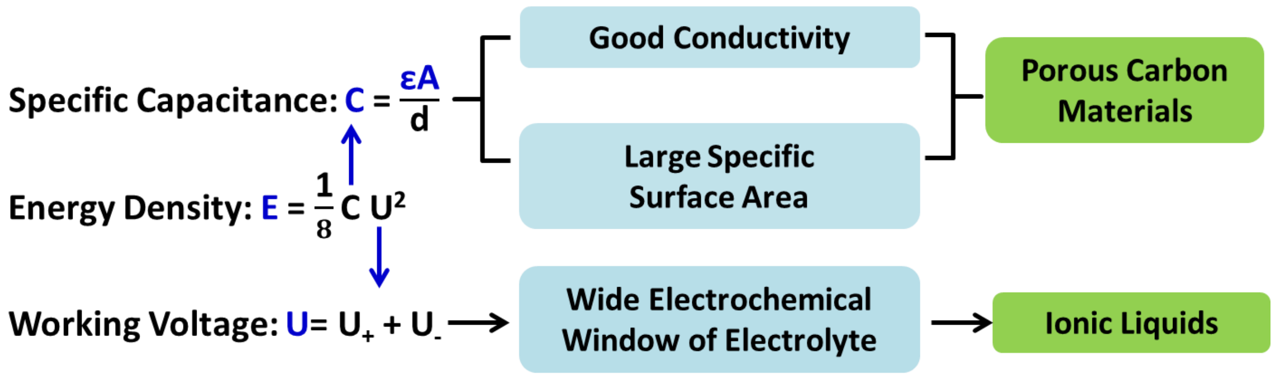

Fig.2. Illustration of required properties of electrode materials and electrolyte for supercapacitors with high energy density.

1.2.1 Activated Carbon (AC)

Activated carbons (ACs) are the mostly widely used electrode materials for supercapacitors due to their affordable sources (such as charcoal and biochar) and large surface area from the high degree of microporosity [13] as shown in Fig. 3. However, with a high surface area up to 3000 m^2/g, only a relatively little pores are effective in charge accumulation [14]. As a result, although the specific surface area is an important parameter for the performance of supercapacitors, some other aspects of the carbon materials can also influence their electrochemical performance, such as pore size distribution, pore shape and structure, electrical conductivity and surface functionality. Since the pore size is mainly distributed at the region with radii smaller than 1nm [15], most area in pores is difficult to be utilized by ions since the pores are too small to be accessed [16, 17]. In addition, the pores in ACs are generated by physical or chemical activation, which introduce many functional groups on the surface of pores [18, 19]. Therefore, this kind of materials is likely to lack cycling stability due to irreversible redox reactions [15].

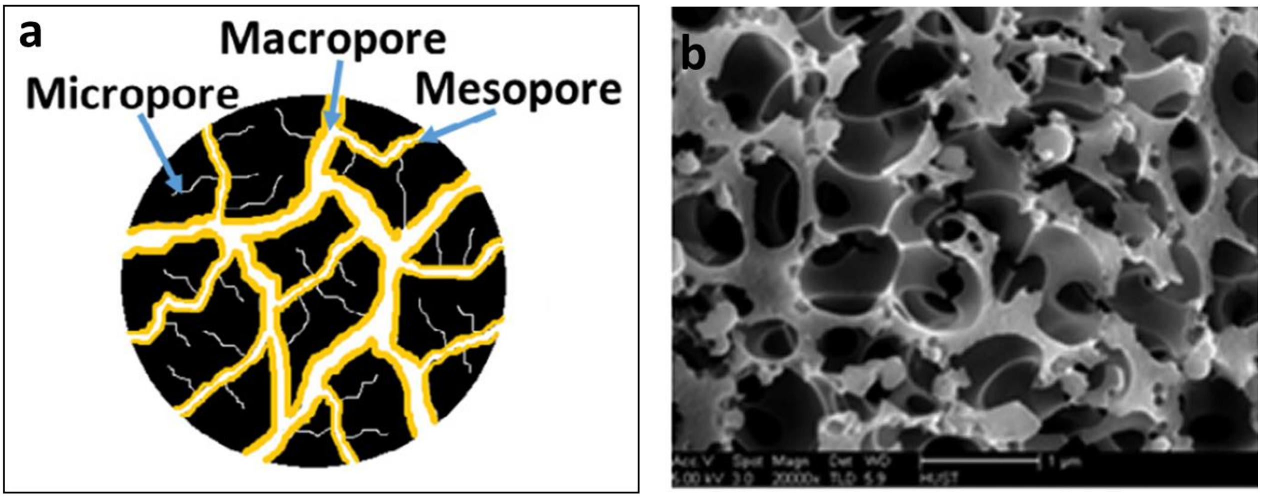

Fig. 3 (a) Schematic of porous structure and (b) SEM image of activated carbon [13].

1.2.2 Carbon Nanotubes (CNTs)

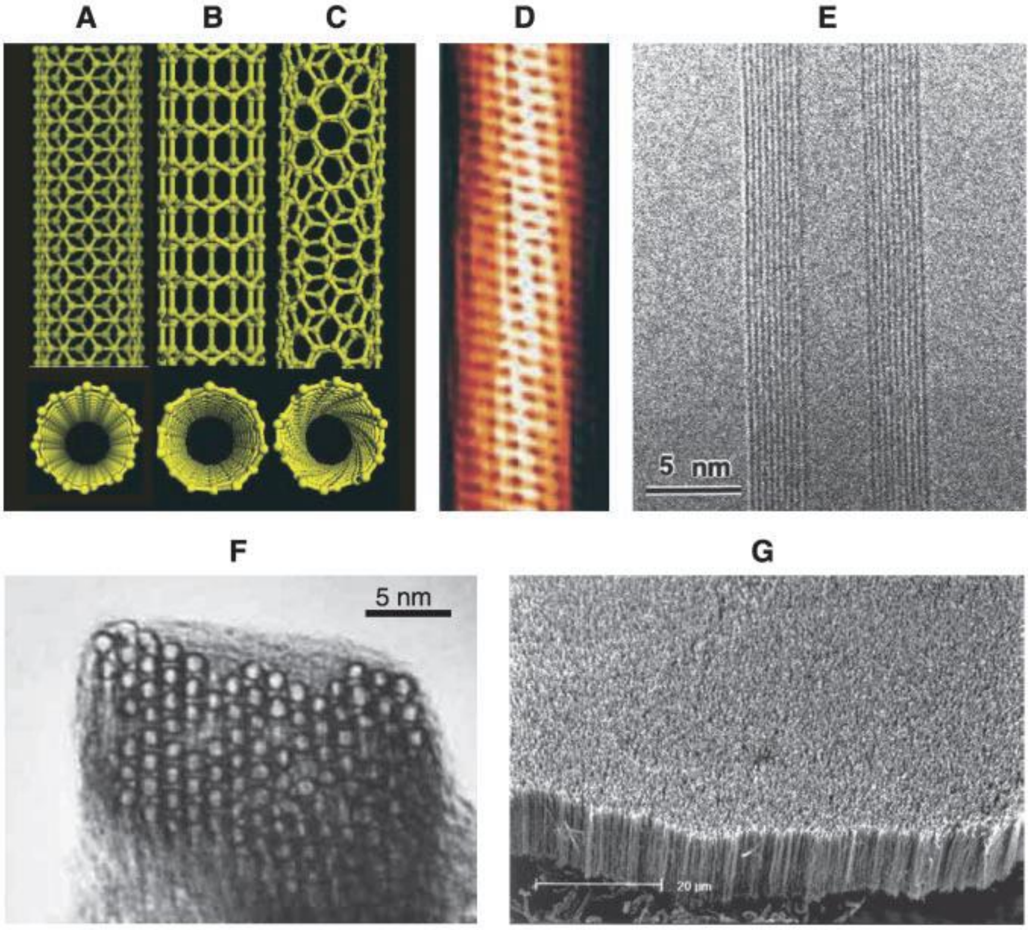

Fig. 4 Schematic illustrations of the structures of (A) armchair, (B) zigzag, and (C) chiral single-wall carbon nanotubes (SWNTs). (D) Tunneling electron microscope image showing the helical structure of a 1.3-nm-diameter chiral SWNT. (E) Transmission electron microscope (TEM) image of a multi-wall carbon nanotube (MWNTs) containing a concentrically nested array of nine SWNTs. (F) TEM micrograph showing the lateral packing of 1.4-nm-diameter SWNTs in a bundle. (G) Scanning electron microscope (SEM) image of an array of MWNTs grown as a nanotube forest [20].

Carbon nanotubes (CNTs) are allotropes of carbon with a cylindrical nanostructure as shown in Fig.4. At the molecular level, CNTs can be viewed as a graphene sheet rolled up into a nanoscale tube. CNTs have attracted attention of the world due to its intriguing and potentially useful structural as well as distinguish electrical and mechanical properties. These elongated nanotubes usually have a diameter in the range from few angstroms to tens of nanometers and a length of several micrometers up to centimeters with both ends of the tubes often capped by fullerene-like structures containing pentagons [20]. CNTs have a narrow distribution of size in the nanometer range, highly surface area, low resistivity, and high stability [21]. These features suggest that CNTs are suitable materials for electrodes in electric storage devices [22]. Pores in the nanotube electrode are mainly the spaces in the entangled nanotube network, thus they are all connected and differ from etched pores in activated carbon [23].The micropore volume is almost negligible for the materials, whereas the mesopore volume is always takes the dominant position. Supercapacitors with carbon nanotube electrodes can be used for applications that require much higher power capabilities than batteries, such as hybrid electric vehicles that can provide rapid acceleration and store braking energy electrically [7, 22]. However, CNTs tend to aggregate into bundles because of their strong intertube van der Waals attraction and axial geometry. As a result, the specific capacitance of this kind of materials has been limited due to the dramatically decreased inter-tube spacing [2]. Besides, their insolubility in most solvents remains a central challenge for their current real-life applications [23].

1.2.3 Carbide-Derived Carbon (CDC)

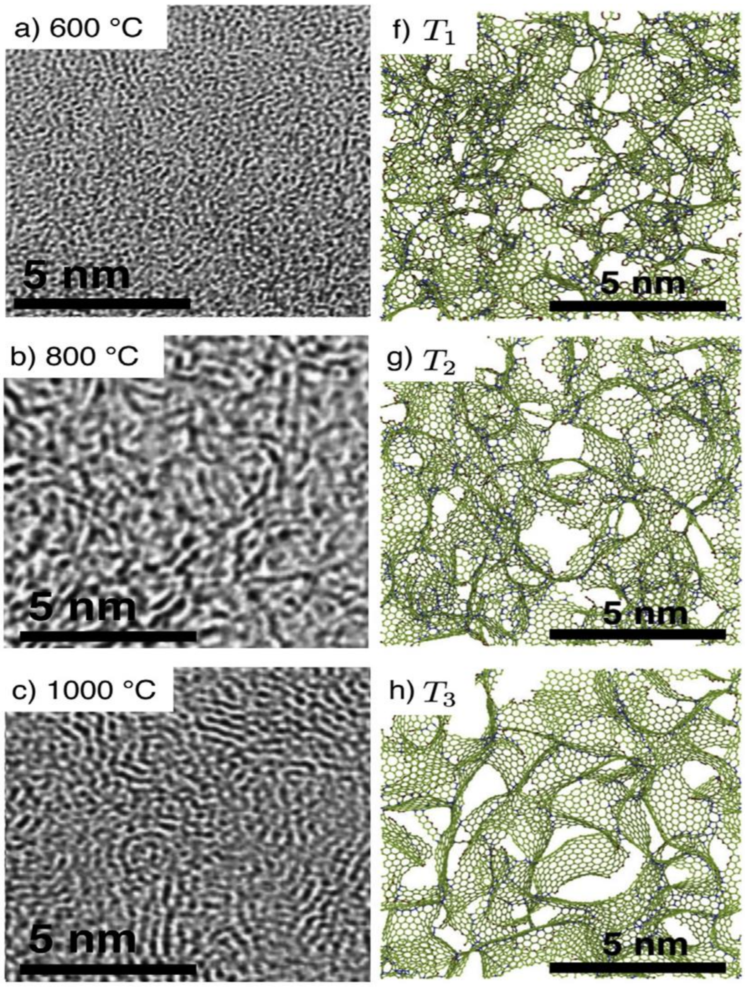

Fig. 5 (a-c) TEM images of TiC-CDCs obtained by chlorination at various temperatures.(f-h) Slab of 2 nm thickness of simulated TiC-CDCs after annealing at T_1 = 1500 K, T_2 = 2000 K, and T_3 = 3000 K. Red, green and blue spheres denote sp, sp2 and sp3 bonding, respectively [27].

Carbide-derived carbon (CDC) is the common term for carbon materials derived from carbide precursors, such as binary (e.g. SiC, TiC), or ternary carbides (e.g., Ti_2AlC, Ti_3SiC_2) [24]. It has stood out among porous carbon materials mainly due to its tunable pore structure. By varying the type of the precursor and the CDC synthesis conditions, microporous and mesoporous structures with controllable average pore size and pore size distributions can be produced with sub-Angstrom accuracy [25, 26]. The tunable pore structure as shown in Fig.5 makes it possible to match the porosity metrics of the porous carbon electrode to a certain electrolyte in supercapacitors [27], which lead to larger specific capacitance. However, the synthesis of CDC always requires special conditions, such as extremely high temperature, high pressure or chlorine treatment [28]. These difficult conditions of synthesis have limited the commercial applications of the material.

1.2.4 Graphene

Graphene is one of the most promising materials with extraordinary properties derived from its unique two-dimensional structure. A single-layer graphene sheet is basically a 2D hexagonal lattice of sp^2 carbon atoms covalently bonded along two plane directions. Compared with CNTs, the superiority of graphene is the further facilitation of electron transport, which results from the one atomically thick graphene sheets with a 2D planar geometry. Hence graphene can be applied as the more effective electrode materials [29]. Pore in graphene materials are most the slit types from space between graphene layers [30].

So far various methods have been developed to generate graphene, such as chemical vapor deposition (CVD), electrochemical exfoliation of graphite, and reduction of graphene oxide [29]. The reduction method is recognized as a facile one. It involves complete exfoliation of graphite oxide into individual graphene oxide (GO) sheets followed by the in situ reduction of these graphene oxide sheets to produce individual graphene-like sheets [31, 32]. Fig. 6 schematically shows the process of the method. The graphite oxide is typically produced by the Hummers method [33]. The reduction methods are classified into chemical and physical one. For chemical reductions, the most common one is using hydrazine monohydrate as the reducing agent. The reason is that most strong reductants have very strong reactivity with water while hydrazine monohydrate does not, making it an attractive option for reducing aqueous dispersions of GOs [34, 35]. For physical reductions, both laser and thermal method can generate graphene materials [34, 36].

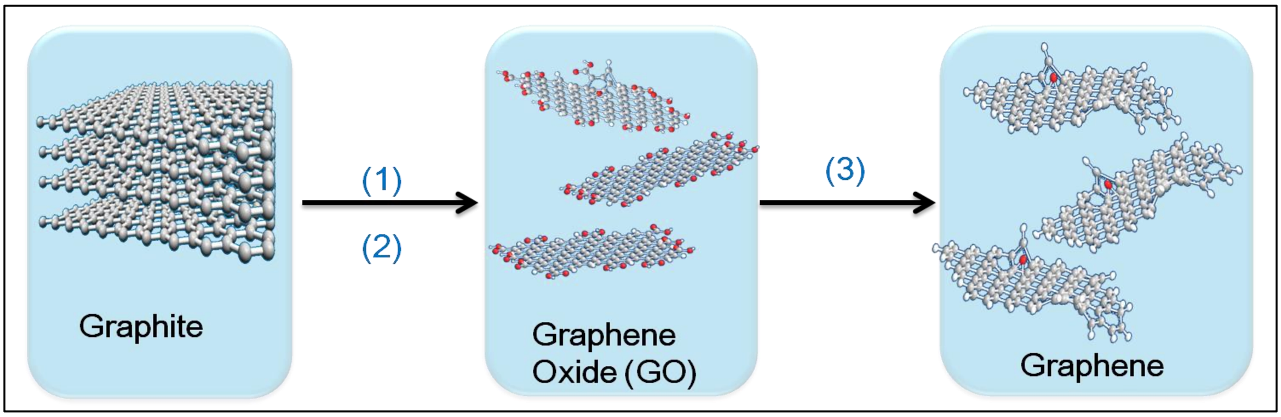

Fig. 6 Schematic of reduction routine: (1) graphite is oxidized to graphite oxide; (2) exfoliation of graphite oxide yields graphene oxide suspended in solution; (3) chemical reduction of graphene oxide yields the conducting graphene. The red points are functional groups which remain on graphene after reduction.

Recently, to realize the porous structure of graphene materials, some templates are used as precursor during synthesis. Shao *et. al* have reported the sphere structure of graphene generated by using polystyrene (PS) spheres as the template (Fig. 7) [37]. The as-prepared graphene spherical shells have more free space in between the spheres, which results in a larger accessible surface area for adsorption of electrolyte ions in supercapacitors .

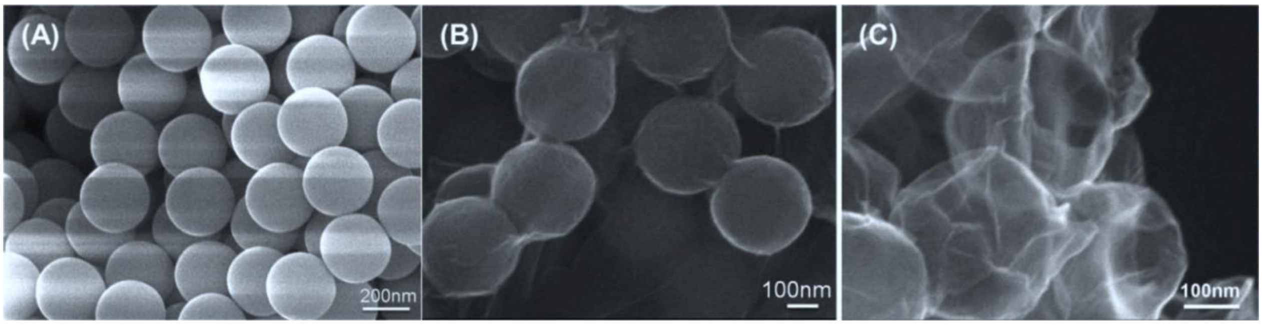

Fig. 7 SEM images of as prepared structures: (A) PS spheres of uniform size, (B) PS @ graphene core–shell spheres, and (C) graphene spherical shells after removal of the PS spheres in the core [37].

1.2.5. CNT / Graphene Composites

It has been commonly recognized that the specific capacitance of graphene materials could be further enlarged by preventing the re-stacking of graphene layers [32, 38-43]. A commonly used way is adding spacers and carbon nanotubes (CNTs) have been demonstrated as an effective one as shown in Fig. 8. In our continuing efforts to develop the CNT and graphene (CNT/graphene) composites for supercapacitor applications, *C* has been enlarged in ionic liquid 1-ethyl-3-methylimidazolium bis(trifluoromethanesulfonyl)imide (EMI-TFSI) by using a method of co-reduction instead of sonication [44, 45]. An even larger *C* in ionic liquid 1-ethyl-3-methylimidazolium tetrafluoroborate (EMI–BF_4) was obtained using a CNT/graphene aerogel prepared by hydrothermal synthesis [39].

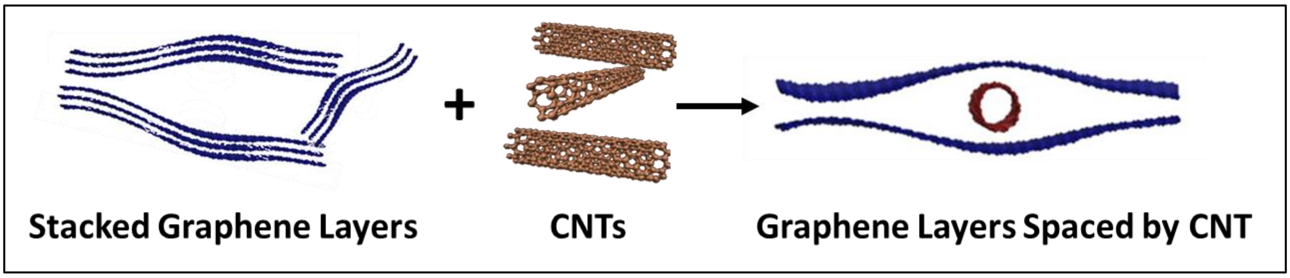

Fig. 8 Schematic of carbon nanotube (CNT)/graphene composite. CNTs serve as spacers between graphene layers.

However, the aggregation of CNTs has limited the further increase of specific surface area as well as specific capacitance [46, 47]. Several research groups have preferred to fabricating covalent bond between GO and CNTs as shown in Fig. 9 [41, 48]. But it requires special conditions, such as extremely low temperature or inert gas atmosphere. Another commonly used way is to oxidize the CNTs since the oxygen-containing groups can reduce the tendency aggregation of CNTs in water [49]. Besides, the oxidation makes the CNTs more hydrophilic so that it is easier to combine CNTs with GO by hydrogen bonds [50].

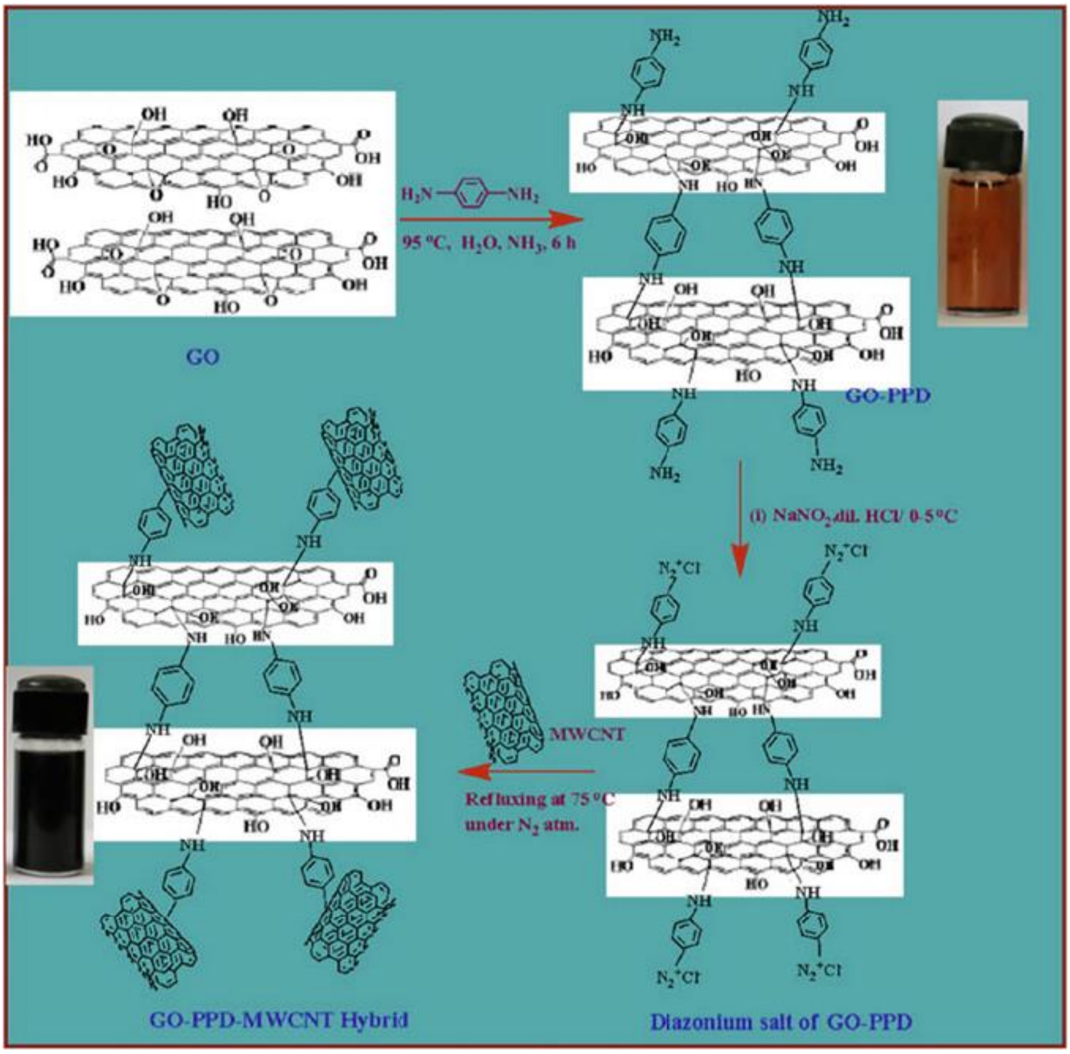

Fig. 9 Schematic Diagram for the Formation of Chemically Bonded graphene−CNT Hybrid [41].

1.3. Electrolytes

Besides electrode materials, the electrolyte will also have a significant influence on the performance of supercapacitors. According to Eqn. 6 and Eqn. 7, a wide voltage window is crucial to achieve high energy density and power density due to the square relationship as shown in Fig. 2 and Fig. 10. In addition, the requirements for an electrolyte in supercapacitors also include high electrochemical stability, high ionic concentration, high conductivity, low viscosity, low solvated ionic radius, low toxicity as well as availability at high purity [51]. The electrolyte used in a supercapacitor can be classified into three types: aqueous electrolyte, organic electrolyte and ionic liquids.

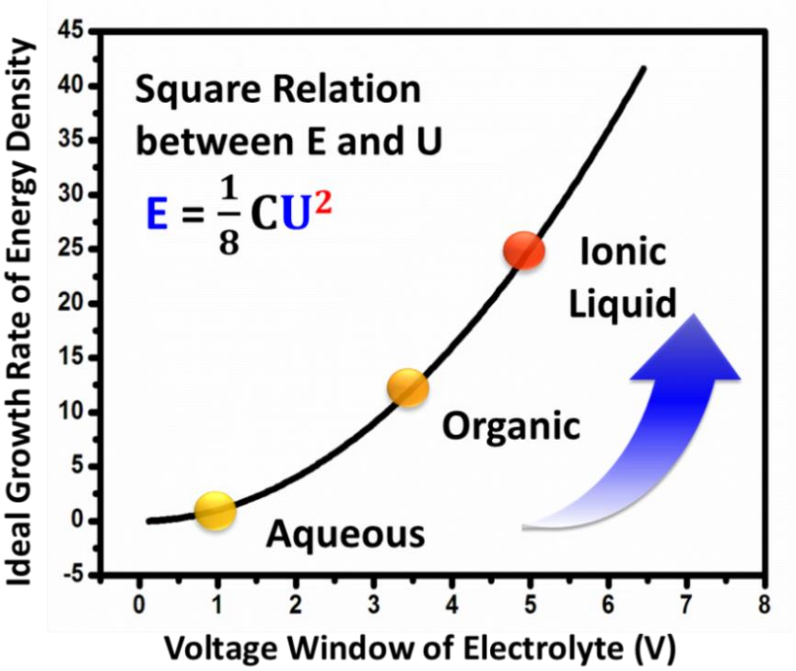

Fig. 10 Schematic of the square relationship between energy density and voltage window of electrolytes.

1.3.1 Aqueous Electrolytes

Compared with other electrolytes, aqueous electrolytes can provide a higher ionic concentration and lower resistance. In addition, the cost of aqueous electrolytes is usually much lower than for suitable organic electrolytes. Unfortunately, a large disadvantage of aqueous electrolytes is their small voltage window as low as about 1 V, which is due to the thermodynamic decomposition of water. Recently, by using the different composition of electrolyte and asymmetric configurations, the voltage window of supercapacitors in aqueous electrolyte has been enlarged to 1.9 V [52], which is still much smaller than that of the other two types. It is the narrow window that result in a large limitation of aqueous electrolyte in terms of improving both energy and power densities.

1.3.2 Organic Electrolytes

The organic electrolytes have the higher achievable voltages than that of aqueous electrolytes. Organic electrolytes allow for a unit cell voltage in the range from 2 to 3.5 V [1, 7, 53]. The cell voltage is most probably limited by the water content of the electrolyte [9]. On the other hand organic electrolytes have a significantly higher specific resistance than aqueous ones. Compared to a concentrated aqueous electrolyte the resistance increases by a factor of tens [7, 9]. In addition, the size of voltage ions in organic electrolytes is usually larger than that in aqueous ones, leading to smaller specific capacitance [16, 17].

1.3.3 Ionic Liquids

Ionic liquids are low-temperature molten salts. In another words, they are liquids composed of ions only.

Superior to organic electrolyte solutions, the boiling point of ionic liquids is higher, which contributes to the possibility of application under high temperatures [54-58].

Ionic liquids are basically composed of organic ions that may undergo almost unlimited structural variations because of the easy preparation of a large variety of their components. Therefore, various kinds of salts can be used to design the ionic liquid that has the desired properties for a given application. For instance, imidazolium, pyrrolidinium as well as quaternary ammonium salts can be used as cations and bis(trifluoromethanesulphonyl)imide, bis(fluorosulphonyl)imide as well as hexafluorophosphate is usually applied as anions [7].

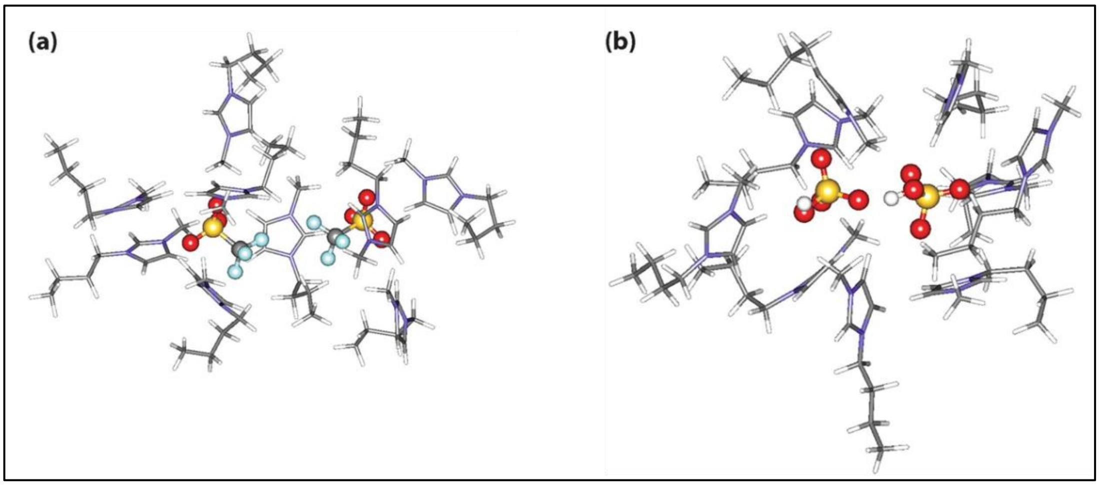

Fig. 11 MD simulation snapshots of (a) 1-butyl-3-methylimidazolium trifuoromethanesulfonate (BMIM OTf) and (b) 1-butyl-3-methylimidazolium hydrogensulfate (BMIM HSO_4) illustrating the anion pairing in both room temperature ionic liquids (RTILs). In both cases, 9 $BMIM^+$ cations surround an anion pair. Cations are shown with stick model whereas anions are shown with ball and stick model. Carbon atoms are shown in grey, nitrogen atoms in blue, oxygen atoms in red, sulfur atoms in orange, fluorine atoms in light blue, and hydrogen atoms in white [57].

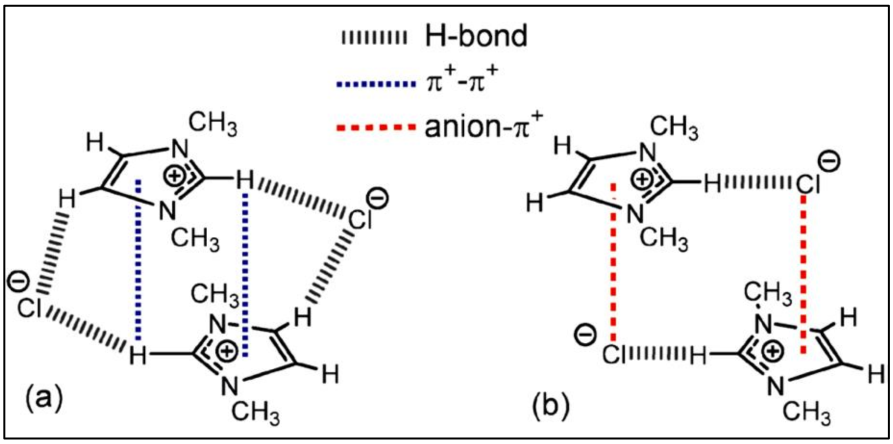

Fig. 12 (a) Stacked ‘‘middle’’ structure of $[C_1C_1im]Cl$ showing C–H positioned in the magnetic cone of the aromatic ring and (b) alternating ‘‘diagonal’’ structure of $[C_1C_1im]Cl$ showing ion-pairs with a dominant front C–H H-bond and weak anion–π^+ interaction. Major H-bonding, anion–π^+ and π^+–π^+ interactions are depicted by dashed lines [58].

For supercapacitors, the two main criteria for selection of an electrolyte are the electrochemical stability window and the ionic conductivity. The first is important to maximize the specific energy values from Eqn. 6, while the second has a major influence on the values of power according to Eqn. 7. What distinguishes ionic liquids from aqueous and organic electrolytes is mainly the wider electrochemical potential window usually larger than 4 V [55, 56]. However, since no solvent molecules exist in ionic liquids, the viscosity is higher than that of the other types due to stronger interactions between ions, which leads to the formation of ions-pairs or ion-clusters as shown in Fig.11[57]. The type of interactions mainly come from hydrogen bonding, anion–π^+ and π^+–π^+ interactions as shown in Fig. 12 [58].

1.4. Relationship between Ionic behaviors and Pore Structures of Electrode Materials in Supercapacitors

In recent decades, a lot of efforts have been paid to enhance the energy density of supercapacitors based on the development of porous carbon materials as electrodes. In order to realize the desired performance, it is of great importance to clarify the pore structures of electrode materials and its relationship with ionic behaviors, which are directly related to the process of charge storage and the capacitance.

1.4.1 Relationships between Ionic behaviors and Surface Chemistry of Pores

The relationship we mentioned here refers in particular to the physical interactions rather than chemical reactions at the interface between ions and functional groups on the surface. Dyatkin *et. al.* have figured out that electrosorption dynamics and ion confinement are relevant to surface oxidization of pores in supercapacitors based on carbon electrodes and ionic liquids [59].They have claimed that oxidized surfaces, specifically the oxygen-rich surface, of porous carbide-derived carbons (CDCs) allow anions to align parallel to pore surfaces and decreased the density of ions in pores before charging. As a result, charges can obtain greater space and mobility during the electrosorption process. Consequently, this kind of pores can provide larger capacitance and better rate capability.

1.4.2 Relationships between Ionic behaviors and Size of Pores

The origins of this kind of relationships can be summarized in two aspects. One is the accessibility of pores. It is a decisive factor in the formation of the double-layer structure. If the pores are too small to be accessed, ions can’t be adsorbed on the internal of pores and subsequently can’t contribute to the capacitance. Another aspect is that the distance between separated charges in the double-layer, namely the d in Eqn 2, could be relevant to the size of pores [17]. It have been commonly recognized that desolvation of ions in aqueous or organic electrolytes will take place when the pore size is in the range from size of bare ion to size of solvated ion [16, 17, 60]. As a result, specific capacitance is enlarged due to the smaller value of *d*, which approximates the size of ions or solvated ions [16, 60]. The size threshold of pores is about 1nm based on the opinions above. However, this conclusion can’t be simply applied in situation of ionic liquids since the ions are not solvated at the beginning. In addition, some simulations have demonstrated that the ion packing will change when the ratio of pore size to ion size is different. The various types of packing as shown in Fig. 13 also lead to the changed value of *d* and subsequently affect the different contribution to specific capacitance [61, 62].The size threshold of pores is difficult to be determined for ionic liquids since the strong interaction between ions result in various types of ion-pairs of ion-clusters.

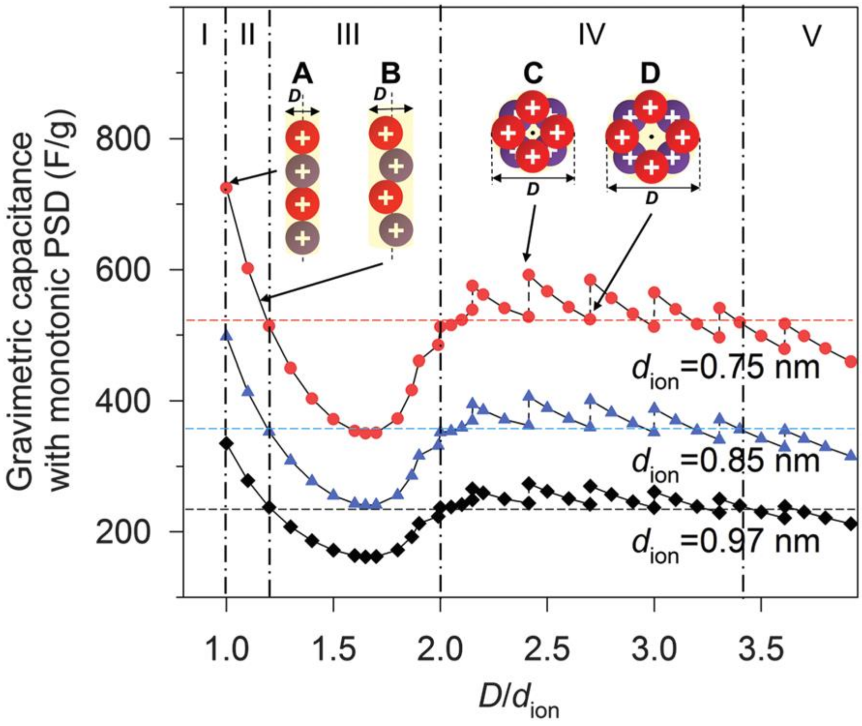

Fig. 13 Theoretical gravimetric capacitance vs. relative pore size D/d_{ion} for a given pore volume of 1.5 cm^3 g^{-1} according to the ion-packing function at three given d_{ion}. The horizontal dashed lines represent the median values of the capacitance between the maximum and minimum capacitances for each single line [61].

1.5 Current Research and Motivation

1.5.1 Current Research of Porous Graphene Composites for Supercapacitors

Recently, the researches of porous graphene composites are mainly focused on three aspects: conducting polymers (CPs)/graphene composites, metal oxides/graphene composites, and carbon nanotubes (CNTs)/graphene composites. The previous two take advantages of the pseudo-capacitance while the last one is mainly based one the electrostatic double-layer structure. The coating of CPs on the surface of graphene can be realized by in-situ polymerization, electrodeposition, chemical, or hydrothermal method [62-67]. The metal oxides can be coated by electrodeposition, chemical precipitation or hydrothermal method [4, 68, 69]. For CNT/grapheme composites, they can be synthesized by chemical vapor deposition (CVD), chemical or hydrothermal method [39-43]. The electrochemical performance of supercapacitors based the materials mentioned above are summarized in Table 1.

Table 1 Current Researches of Porous Graphene Composite for Supercapacitors

Categories	Electrode Materials	Synthesis	Electrolytes	Specific Capacitance (F g^{-1})	Energy Density (Wh kg^{-1})	Ref.
Conductive Polymers/ Graphene Composites	PANI/Graphene	In-situ Polymerization	H_2SO_4	965	35	62
	PANI/Graphene	Hydrothermal	H_2SO_4	532	-	63
	PANI/Graphene	Electrodeposition	PVA/H_2SO_4	261	-	64
	PANI/Graphene	Mixing by Sonication	H_2SO_4	210	-	65
	PEDOT-PSS/ Graphene	Chemical Co-reduction	PVA/H_3PO_4	-	3	66
	PPy/Graphene	Electrodeposition	KCl	237	33	67
Metal Oxides / Graphene Composites	SnO_2/Graphene	Chemical Precipitation	Na_2SO_4	347	-	68
	MnO_2/Graphene	Electrodeposition	KCl	328	11	4
	Mn_3O_4/Graphene	Hydrothermal	Na_2SO_4	121	-	69
Carbon Nanotubes/ Graphene Composites	SWCNT/Graphene Aerogel	Hydrothermal	EMI-BF_4	183	80	39
	SWCNT/Graphene	Mixing by Sonication	TEA-BF_4 in PC	201	63	40
	MWCNT/Graphene	CVD	KOH	286	40	43
	MWCNT/Graphene	Chemical	KCl	150	-	42

1.5.2. Originality of Our Research

The re-stacking between graphene layers is one of the issues which limit the further increase of specific surface area and resulting specific capacitance. Even though carbon nanotubes (CNTs) have been selected as spacers to solve this problem, the aggregation between CNTs still leads to the decreased space in materials (Fig. 14). To address this issue, oxidized multi-wall carbon nanotubes (MWNTs) have been applied to improve the dispersity of spacers. And the specific surface are have been obviously enlarged compared with graphene without spacers.

Fig. 14 Schematic of improved dispersion of CNTs in CNT/graphene composites.

However, some problems still limit the enhancement of energy density. One is the lack of linearity between *C* and *A*. In another word, the larger specific surface area sometimes doesn't lead to larger specific capacitance. It is mainly attributed to the different ionic behaviors in pores with different sizes and geometries (Fig. 15). To address this issue, we have synthesized CNT/graphene composite with different pore structures by adjusting the ratio of the spacer. The pores are classified into three types according to the ratio of pore size to ion size in ionic liquids. And the relationship between pore structure and specific capacitance in an ionic liquid has been analyzed by linear fitting methods. According to the fitting results, the hypothesis of ionic behaviors has been built.

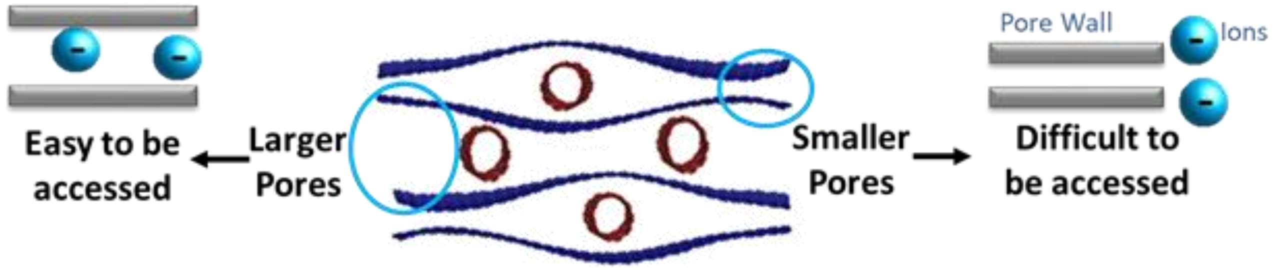

Fig. 15 Influence of pore structures on ionic behaviors in CNT/graphene composites

Moreover, the improvement of porous structure of CNT/graphene composites is conducted, which is based on the influence ionic behaviors figured out in our study. As a result, both specific capacitance and voltage window of supercapacitors have been enlarged by using CNT/graphene materials with improved pore structure and suitable ionic liquids in a designed asymmetric configuration. Consequently, the enhancement of energy of supercapacitors is realized in our study.

References

[1] R. Kötz and M. Carlen, “Principles and applications of electrochemical capacitors,” *Electrochim. Acta*, vol. 45, no. 15–16, pp. 2483–2498, 2000.

[2] Z. Yang. J. Ren, Z. Zhang, X. Chen, G. Guan, L. Qiu, Y. Zhang, and H. Peng, “Recent Advancement of Nanostructured Carbon for Energy Applications,” *Chem. Rev.*, vol. 115, no. 11, pp. 5159–5223, 2015.

[3] M. Z. Bazant, B. D. Storey, and A. A. Kornyshev, “Double layer in ionic liquids: Overscreening versus crowding,” *Phys. Rev. Lett.*, vol. 106, no. 4, pp. 6–9, 2011.

[4] Q. Cheng, J. Tang, J. Ma, H. Zhang, N. Shinya, and L. C. Qin, “Graphene and nanostructured MnO2 composite electrodes for supercapacitors,” *Carbon*, vol. 49, no. 9, pp. 2917–2925, 2011.

[5] Q. Cheng, J. Tang, N. Shinya, and L.-C. Qin, “Polyaniline modified graphene and carbon nanotube composite electrode for asymmetric supercapacitors of high energy density,” *J. Power Sources*, vol. 241, pp. 423–428, 2013.

[6] X. Wu, J. Zhou, W. Xing, Y. Zhang, P. Bai, B. Xu, S. Zhuo, Q. Xue, and Z. Yan “Insight into high areal capacitances of low apparent surface area carbons derived from nitrogen-rich polymers,” *Carbon N. Y.*, vol. 94, pp. 560–567, 2015.

[7] G. Wang, L. Zhang, and J. Zhang, “A review of electrode materials for electrochemical supercapacitors,” *Chem. Soc. Rev.*, vol. 41, no. 2, pp. 797–828, 2012.

[8] W. Ai, X. Cao, Z. Sun, J. Jiang, Z. Du, L. Xie, Y. Wang, X. Wang, H. Zhang, W. Huang, and T. Yu “Redox-crosslinked graphene networks with enhanced electrochemical capacitance,” *J. Mater. Chem. A*, vol. 2, no. 32, p. 12924, 2014.

[9] P. Azaïs, L. Duclauxa, P. Florian, D. Massiot, M.-A. Lillo-Rodenas, A. Linares-Solanoc, J.-P. Peresd, C. Jehoulet, and F. Beguin, “Causes of supercapacitors ageing in organic electrolyte,” *J. Power Sources*, vol. 171, no. 2, pp. 1046–1053, 2007.

[10] S. Roldán, D. Barreda, M. Granda, R. Menéndez, R. Santamaría, and C. Blanco, “An approach to classification and capacitance expressions in electrochemical capacitors technology,” *Phys. Chem. Chem. Phys.*, vol. 17, no. 2, pp. 1084–1092, 2015.

[11] M. Yu, Z. Wang, Y. Han, Y. Tong, X. Lu, and S. Yang, “Recent progress in the development of anodes for asymmetric supercapacitors,” *J. Mater. Chem. A*, vol. 4, no. 13, pp. 4634–4658, 2016.

[12] J. Zhang and X. S. Zhao, “On the configuration of supercapacitors for maximizing electrochemical

performance," *ChemSusChem*, vol. 5, no. 5, pp. 818–841, 2012.

[13] A. Alabadi, H. A. Abbood, Q. Li, N. Jing, and B. Tan, "Imine-Linked Polymer Based Nitrogen-Doped Porous Activated Carbon for Efficient and Selective CO2 Capture," *Sci. Rep.*, vol. 6, no. 1, p. 38614, 2016.

[14] P. S. Kumara, T. Prot, L. Korving, K. J. Keesman, I. Dugulan, M. C.M. van Loosdrecht, G.-J. Witkamp, "Effect of pore size distribution on iron oxide coated granular activated carbons for phosphate adsorption – Importance of mesopores," *Chem. Eng. J.*, vol. 326, pp. 231–239, 2017.

[15] I. Mochida, Y. Korai, M. Shirahama, S. Kawano, T. Hada , Y. Seo, M. Yoshikawa, and A. Yasutake, "Removal of SOx and NOx over activated carbon fibers," *Carbon N. Y.*, vol. 38, no. 2, pp. 227–239, 2000.

[16] J. Chmiola, C. Largeot, P. L. Taberna, P. Simon, and Y. Gogotsi, "Desolvation of ions in subnanometer pores and its effect on capacitance and double-layer theory," *Angew. Chemie - Int. Ed.*, vol. 47, no. 18, pp. 3392–3395, 2008.

[17] J. Huang, B. G. Sumpter, and V. Meunier, "A universal model for nanoporous carbon supercapacitors applicable to diverse pore regimes, carbon materials, and electrolytes," *Chem. - A Eur. J.*, vol. 14, no. 22, pp. 6614–6626, 2008.

[18] S. Biniak, G. Szymański, J. Siedlewski, and A. Światkoski, "The characterization of activated carbons with oxygen and nitrogen surface groups," *Carbon N. Y.*, vol. 35, no. 12, pp. 1799–1810, 1997.

[19] A. Ahmadpour and D. D. Do, "The preparation of activated carbon from macadamia nutshell by chemical activation," *Carbon N. Y.*, vol. 35, no. 12, pp. 1723–1732, 1997.

[20] R. H. Baughman, A. a Zakhidov, and W. a de Heer, "Carbon nanotubes --- the route toward applications," *Science*, vol. 297, no. 5582, pp. 787–92, 2002.

[21] X. Wang, Q. Li, Jing Xie, Z. Jin, J. Wang, Y. Li, K. Jiang, and S. Fan, "Fabrication of ultralong and electrically uniform single-walled carbon nanotubes on clean substrates," *Nano Lett.*, vol. 9, no. 9, pp. 3137–3141, 2009.

[22] C. Niu, E. K. Sichel, R. Hoch, D. Moy, and H. Tennent, "High power electrochemical capacitors based on carbon nanotube electrodes High power electrochemical capacitors based on carbon nanotube electrodes," vol. 1480, no. 1997, pp. 9–12, 2016.

[23] D. N. Futaba, ,K. Hata,T. Yamada, T. Hiraoka, Y. Hayamizu, Y. Kakudate, O. Tanaike, H. Hatori, ,M. Yumura, and S. Ijima, "Shape-engineerable and highly densely packed single-walled carbon nanotubes and their application as super-capacitor electrodes," *Nat. Mater.*, vol. 5, no. 12, pp. 987–994, 2006.

[24] Y. Gogotsi, A. Nikitin, H. Ye ,W. Zhou, J. E. Fischer, B. Yi, H. C. Folet, and M. W.Barsoum, “Nanoporous carbide-derived carbon with tunable pore size,” *Nat. Mater.*, vol. 2, no. 9, pp. 591–594, 2003.

[25] V. Presser, M. Heon, and Y. Gogotsi, “Carbide-derived carbons - from porous networks to nanotubes and graphene,” *Adv. Funct. Mater.*, vol. 21, no. 5, pp. 810–833, 2011.

[26] E. N. Hoffman, G. Yushin, T. El-Raghy, Y. Gogotsi, and M. W. Barsoum, “Micro and mesoporosity of carbon derived from ternary and binary metal carbides,” *Microporous Mesoporous Mater.*, vol. 112, no. 1–3, pp. 526–532, 2008.

[27] C. de Tomas, I. Suarez-Martinez, F. Vallejos-Burgos, M. J. López, K. Kaneko, and N. A. Marks, “Structural prediction of graphitization and porosity in carbide-derived carbons,” *Carbon*, vol. 119, pp. 1–9, 2017.

[28] J. Chmiola, G. Yushin, Y. Gogotsi, C. Portet, P. Simon, and P. L. Taberna, “Anomalous Increase in Carbon Capacitance at Pore Sizes Less Than 1 Nanometer,” *Science*, vol. 313, no. 5794, pp. 1760–1763, 2006.

[29] J. Hou, Y. Shao, M. W. Ellis, R. B. Moore, and B. Yi, “Graphene-based electrochemical energy conversion and storage: fuel cells, supercapacitors and lithium ion batteries.,” Phys. Chem. Chem. Phys., vol. 13, no. 34, pp. 15384–15402, 2011.

[30] X. Li and B. Wei, “Supercapacitors based on nanostructured carbon,” *Nano Energy*, vol. 2, no. 2. pp. 159–173, 2013.

[31] C. Liu, Z. Yu, D. Neff, A. Zhamu, and B. Z. Jang, “Graphene-based supercapacitor with an ultrahigh energy density,” *Nano Lett.*, vol. 10, no. 12, pp. 4863–4868, 2010.

[32] F. Zhang, J. Tang, N. Shinya, and L. C. Qin, “Hybrid graphene electrodes for supercapacitors of high energy density,” *Chem. Phys. Lett.*, vol. 584, pp. 124–129, 2013.

[33] W. S. Hummers and R. E. Offeman, “Preparation of Graphitic Oxide,” *J. Am. Chem. Soc.*, vol. 80, no. 6, pp. 1339–1339, 1958.

[34] D. R. Dreyer, S. Park, C. W. Bielawski, and R. S. Ruoff, “The chemistry of graphene oxide,” *Chem. Soc. Rev.*, vol. 39, no. 1, pp. 228–240, 2010.

[35] K. P. Loh, Q. Bao, P. K. Ang, and J. Yang, “The chemistry of graphene,” *J. Mater. Chem.*, vol. 20, no. 12, p. 2277, 2010.

[36] W. Gao, N. Singh, L. Song, Z. Liu, A. L. M. Reddy, L. Ci, R. Vajtai, Q. Zhang, B. Wei, and P. M. Ajayan, “Direct laser writing of micro-supercapacitors on hydrated graphite oxide films,” *Nat.*

Nanotechnol., vol. 6, no. 8, pp. 496–500, 2011.

[37] Q. Shao, J. Tang, Y. Lin, F. Zhang, J. Yuan, H. Zhang, N. Shinya, and L.-C. Qin, “Synthesis and characterization of graphene hollow spheres for application in supercapacitors,” *J. Mater. Chem. A*, vol. 1, no. 48, pp. 15423–15428, 2013.

[38] Q. Cheng, J. Tang, N. Shinya, and L.-C. Qin, “$Co(OH)_2$ nanosheet-decorated graphene–CNT composite for supercapacitors of high energy density,” *Sci. Technol. Adv. Mater.*, vol. 15, no. 1, p. 14206, 2014.

[39] Q. Shao, J. Tang, Y. Lin, . Li, F. Qin, J. Yuan, L.-C. Qin, “Carbon nanotube spaced graphene aerogels with enhanced capacitance in aqueous and ionic liquid electrolytes,” *J. Power Sources*, vol. 278, pp. 751–759, 2015.

[40] Q. Cheng, J. Tang, J. Ma, H. Zhang, N. Shinya, and L.-C. Qin, “Graphene and carbon nanotube composite electrodes for supercapacitors with ultra-high energy density,” *Phys. Chem. Chem. Phys.*, vol. 13, no. 39, pp. 17615–17624, 2011.

[41] M. Kotal and A. K. Bhowmick, “Multifunctional Hybrid Materials Based on Carbon Nanotube Chemically Bonded to Reduced Graphene Oxide,” *J. Phys. Chem. C*, vol. 117, no. 48, pp. 25865–25875, 2013.

[42] L. Peng, Y. Feng, P. Lv, Y. Shen, Y. Li, and W. Feng, “Transparent , Conductive and Flexible Multi Walled Carbon Nanotube / Graphene Hybrid Electrodes with Two Three-Dimensional Microstructures,” *J. Phys. Chem. C*, vol. 116, pp. 4970–4978, 2012.

[43] W. Wang, S. Guo, M. Penchev, I. Ruiz, K. N. Bozhilov, D. Yan, M. Ozkan,and C. S. Ozkan, “Three dimensional few-layer graphene – carbon nanotube foam architectures for high fidelity supercapacitors,” *Nano Energy*, no. 2012, pp. 294–303, 2012.

[44] L. L. Zhang and X. S. Zhao, “Carbon-based materials as supercapacitor electrodes,” *Chem. Soc. Rev.*, vol. 38, no. 9, p. 2520, 2009.

[45] L. Dai, D. W. Chang, J.-B. Baek, and W. Lu, “Carbon Nanomaterials for Advanced Energy Conversion and Storage,” *Small*, vol. 8, no. 8, pp. 1130–1166, 2012.

[46] M. Liang, F. Jin, R. Liu, R. Su, W. Qi, Y. Yu, L. Wang, and Z. He, “Enhanced electrochemical detection performance of multiwall carbon nanotubes functionalized by aspartame,” *J. Mater. Sci.*, vol. 48, no. 16, pp. 5624–5632, 2013.

[47] L. Vaisman, H. D. Wagner, and G. Marom, “The role of surfactants in dispersion of carbon nanotubes,” *Adv. Colloid Interface Sci.*, vol. 128–130, no. 2006, pp. 37–46, 2006.

[48] F. Du, D. Yu, L. Dai, S. Ganguli, V. Varshney, and A. K. Roy, “Preparation of Tunable 3D Pillared Carbon Nanotube Graphene Networks for High Performance Capacitance,” *Chem. Mater.*, pp. 4810–4816, 2011.

[49] B. You, L. Wang, L. Yao, and J. Yang, “Three dimensional N-doped graphene-CNT networks for supercapacitor.,” *Chem. Commun.*, vol. 49, no. 44, pp. 5016–8, 2013.

[50] N. V. Medhekar, A. Ramasubramaniam, R. S. Ruoff, and V. B. Shenoy, “Hydrogen bond networks in graphene oxide composite paper: Structure and mechanical properties,” *ACS Nano*, vol. 4, no. 4, pp. 2300–2306, 2010.

[51] F. Béguin, V. Presser, A. Balducci, and E. Frackowiak, “Carbons and electrolytes for advanced supercapacitors,” *Adv. Mater.*, vol. 26, no. 14, pp. 2219–2251, 2014.

[52] J. H. Chae and G. Z. Chen, “1.9 V Aqueous Carbon-Carbon Supercapacitors With Unequal Electrode Capacitances,” *Electrochim. Acta*, vol. 86, pp. 248–254, 2012.

[53] D. Cericola, R. Kötz, and A. Wokaun, “Effect of electrode mass ratio on aging of activated carbon based supercapacitors utilizing organic electrolytes,” *J. Power Sources*, vol. 196, no. 6, pp. 3114–3118, 2011.

[54] G. B. Appetecchi, M. Montanino, D. Zane, M. Carewska, F. Alessandrini, and S. Passerini, “Effect of the alkyl group on the synthesis and the electrochemical properties of N-alkyl-N-methyl-pyrrolidinium bis(trifluoromethanesulfonyl)imide ionic liquids,” *Electrochim. Acta*, vol. 54, no. 4, pp. 1325–1332, 2009.

[55] I. Piñeiro-Prado, D. Salinas-Torres, R. Ruiz-Rosas, E. Morallón, and D. Cazorla-Amorós, “Design of Activated Carbon/Activated Carbon Asymmetric Capacitors,” *Front. Mater.*, vol. 3, no. March, pp. 1–12, 2016.

[56] C. Kong, W. Qian, C. Zheng, Y. Yu, C. Cui, and F. Wei, “Raising the performance of a 4 V supercapacitor based on an EMIBF4–single walled carbon nanotube nanofluid electrolyte,” *Chem. Commun.*, vol. 49, no. 91, p. 10727, 2013.

[57] B. Schwenzer, S. N. Kerisit, and M. Vijayakumar, “Anion pairs in room temperature ionic liquids predicted by molecular dynamics simulation, verified by spectroscopic characterization,” *RSC Adv.*, vol. 4, no. 11, pp. 5457–5464, 2014.

[58] R. P. Matthews *et al.*, “A structural investigation of ionic liquid mixtures,” *Phys. Chem. Chem. Phys.*, vol. 18, no. 12, pp. 8608–8624, 2016.

[59] B. Dyatkin, E. Mamontov, K. M. Cook, and Y. Gogotsi, “Capacitance, charge dynamics, and electrolyte-surface interactions in functionalized carbide-derived carbon electrodes,” *Prog. Nat. Sci.*

Mater. Int., vol. 25, no. 6, pp. 631–641, 2015.

[60] X. Wang, H. Zhou, E. Sheridan, J. C. Walmsley, D. Ren, and D. Chen, “Geometrically confined favourable ion packing for high gravimetric capacitance in carbon–ionic liquid supercapacitors,” *Energy Environ. Sci. Energy Environ. Sci*, vol. 232, no. 9, pp. 232–239, 2016.

[61] D. T. L. Galhena, B. C. Bayer, S. Hofmann, and G. A. J. Amaratunga, “Understanding capacitance variation in subnanometer pores by in situ tuning of interlayer constrictions,” *ACS Nano*, vol. 10, no. 1, pp. 747–754, 2016.

[62] M. Moussa, M. F. El-Kady, H. Wang, A. Michimore, Q. Zhou, J. Xu, P. Majeswki, and J. Ma, “High-performance supercapacitors using graphene/polyaniline composites deposited on kitchen sponge,” *Nanotechnology*, vol. 26, no. 7, p. 75702, 2015.

[63] R. Wang, M. Han, Q. Zhao, Z. Ren, X. Guo, C. Xu, N. Hu, and Li Lu, “Hydrothermal synthesis of nanostructured graphene/polyaniline composites as high-capacitance electrode materials for supercapacitors,” *Sci. Rep.*, vol. 7, no. 174, p. 44562, 2017.

[64] Y. Xie, Y. Liu, Y. Zhao, Y. H. Tsang, S. P. Lau, H. Huang, and Y. Chai, “Stretchable all-solid-state supercapacitor with wavy shaped polyaniline/graphene electrode,” *J. Mater. Chem. A*, vol. 2, no. 24, pp. 9142–9149, 2014.

[65] Q. Wu, Y. Xu, Z. Yao, A. Liu, and G. Shi, “Supercapacitors based on flexible graphene/polyaniline nanofiber composite films,” *ACS Nano*, vol. 4, no. 4, pp. 1963–1970, 2010.

[66] Y. Liu, B. Weng, J. M. Razal, Q. Xu, C. Zhao, Y. Hou, S. Seyedin, R. Jalili, G. G. Wallace1, and J. Chen, “High-Performance Flexible All-Solid-State Supercapacitor from Large Free-Standing Graphene-PEDOT/PSS Films,” *Sci. Rep.*, vol. 5, no. 1, p. 17045, 2015.

[67] A. Davies, P. Audette, B. Farrow, F. Hassan, and Z. Chen, “Graphene-based Flexible Supercapacitors : Pulse- Electropolymerization of Polypyrrole on Free- standing Graphene Films,” *J. Phys. Chem. C*, vol. 115, no. 35, pp. 3–5, 2011.

[68] Y. Wang, Y. Liu, and J. Zhang, “Colloid electrostatic self-assembly synthesis of SnO2/graphene nanocomposite for supercapacitors,” *J. Nanoparticle Res.*, vol. 17, no. 10, 2015.

[69] J. W. Lee and J. Kim, “S5P16-02 Mn 3 O 4 Nanorods on Graphene Sheets for Advanced Supercapacitor Electrode,” p. 19445, 2012.

Chapter 2

Experimental Technique

2.1. Characterization of Electrode Materials

2.1.1 X-ray Photoelectron Spectroscopy (XPS)

The X-ray photoelectron spectra are obtained by irradiating a material with a beam of X-rays while simultaneously measuring the kinetic energy and number of electrons that escape from the top 0 to 10 nm of the material being analyzed [1, 2]. According to its mechanism, it is obvious that XPS is a surface-sensitive quantitative spectroscopic technique. A lot of information on chemical structure can be achieved via XPS, such as the elemental composition at the parts per thousand range, chemical state and electronic state of the elements that exist within a material.

2.1.2 Raman Spectroscopy

Raman spectroscopy is a spectroscopic technique used to observe structure of materials. Its mechanism relies on inelastic scattering, or Raman scattering, of monochromatic light, usually from a laser in the visible, near infrared, or near ultraviolet range. For graphene, there are two characteristic bands: G band and D band [3-6]. The G band can reflects some information about the thickness of graphene sheets [4, 5]. As the layer thickness increases, the position of G band will shift to lower energy. In addition, since D band results from the single phonon process induced by defects and edges of graphene, the ratio of G band to D band is used to characterize the level of defects in graphene [3-5].

2.1.3 Scanning Electron Microscope (SEM)

The scanning electron microscope is a type of electron microscope using a focused beam of electron beam of electrons to characterize the morphology of conductive samples. The images in SEM are produced by scanning the surface of samples. The signals used to produce images are generated from interactions of the electron beam with atoms at various depths within the sample. The types of signals include secondary electrons (SE), reflected or back-scattered electrons (BSE), characteristic X-rays and cathodoluminescence, absorbed current and transmitted electrons [7, 8]. Among these signals, secondary electrons are the most commonly used one and its detector is the standard equipment in all SEMs. During imaging, the secondary electrons are emitted from very close to the specimen surface. Consequently, images of a sample surface are produced with high resolution, revealing details in the grade of nanometers.

2.1.4 Nitrogen Adsorption Method

The nitrogen adsorption method is used to characterize the pore distribution and specific surface area of porous carbon materials. It is a kind of physical adsorption method, which is based on the phenomenon of gas molecules adhering to a surface via physical interactions at a pressure less than the vapor pressure. The interactions between the adsorbed molecules and the surface are relatively weak and not covalent or ionic. The determination of specific surface area and pore distribution is realized by the analysis of the adsorption isotherm, which is reflected as the plot of amount adsorbate versus adsorptive pressure at a constant temperature. The changes in the shape of the plotted isotherm can indicate particular surface features. Analyses of physical adsorption isotherm data can reveal the pore distribution and surface area. Among the molecules available as adsorbate for the measurement, nitrogen has been a commonly used way since it is easy to be obtained with good chemical stability. Nitrogen is generally employed at liquid nitrogen conditions (i.e. 77 K) [9, 10].

In order to calculate the distribution of pore sizes according to the experimental data, it is necessary to develop a model for pore filling which reflect the relationship between the pore width and the condensation pressure. Historically, the Kelvin equation is the most commonly used one for completely wet slit-shaped pores. It is shown as below [11]:

$$\ln\left(\frac{P_C}{P_0}\right) = -2\frac{\gamma_l}{RTH\rho_l} \tag{2}$$

in which P_C is the pressure at which a pore of width H condenses, P_O is the saturation pressure of the bulk fluid, R is the ideal gas constant, and ρ_l and γ_l are the liquid density and surface tension of nitrogen at absolute temperature T, respectively**.** The Kelvin equation is derived from classical thermodynamics and assumes that surface tension can be defined and the gas phase is ideal. Since the equation does not take into account the thickness of the layers formed on the porous surface prior to condensation, it is difficult to be applied in narrow pores. Considering the limitation, several modified models have been developed the interpretation of nitrogen adsorption isotherms and the calculation of pore distribution [11]. Recently, density functional theory (DFT) has become an important tool for the characterization of pore structure of materials [12-16]. This method is based on the established principles of statistical mechanics and a model solid structure and pore topology is necessary [9-11]. Firstly, the pores are assumed to be all of the same regular shape, such as cylinders or slits. In addition, each pore is assumed to behave independently. Nowadays, the calculation of pore distribution based on DFT can be realized by commercial software.

2.2. Electrochemical Evaluation of Electrode Materials

2.2.1 Cyclic Voltammetry (CV)

The cyclic voltammetry is a type of potentiodynamic electrochemical measurement. In a cyclic voltammetry experiment for supercapacitors, the voltage across between positive and negative electrode is varied linearly versus time as shown in Fig 1a. The rate of voltage change over time is known as the experiment's scan rate (V s^{-1}). When the voltage is applied between the two electrodes, the current is measured at the same time. Fig 1b shows the curve achieved from the measurement, which is plotted as current vs. applied voltage.

The specific capacitance of electrode materials, C, can be calculated from the cyclic voltammograms according to Eqn. 3:

$$C = \frac{Q}{m\,|E_1 - E_2|} \tag{3}$$

In which m is the total mass of two electrodes and Q is the charge accumulated inside the electrode layer. The value of Q is measured using the area under the cyclic voltammogram in either direction in a voltage window from E_1 to E_2.

Moreover, the CV curves can also be used to study the redox processes in electrodes as well as electrolytes. When there are chemically reactive sites in the system, the faradic current will increase when the reactive potential is reached. Subsequently, the faradic current at some point will decrease as the concentration of active sites are depleted when the reactive potential pass by. If the redox couple is reversible, the reduced sites will start to be re-oxidized during the reverse scan, giving rise to a current of reverse polarity to before. The more reversible the redox couple is, the more similar the oxidation peak will be in shape to the reduction peak. Therefore, CVs can provide information about redox potentials and electrochemical reaction rates [9].

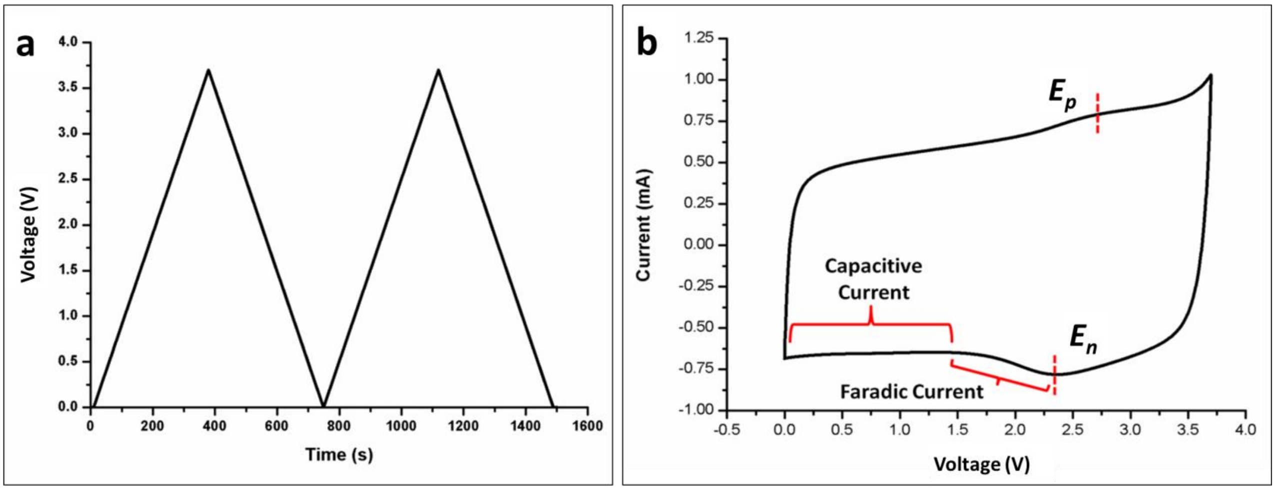

Fig. 1 (a) Cyclic voltammetry waveform and (b) typical cyclic voltammogram where E_p and E_n show redox potentials for a reversible reaction.

2.2.2 Testing Configuration

The testing configurations are two types in our study. They are two-electrode and three-electrode one. The two-electrode configuration is shown in Fig. 2. The two-electrode configuration is in the form of a sealed coin cell, which consist of two pieces of current collector, a separator, two electrodes and two metal shell used to connect the circuit. It is used for the measurement of supercapacitors.

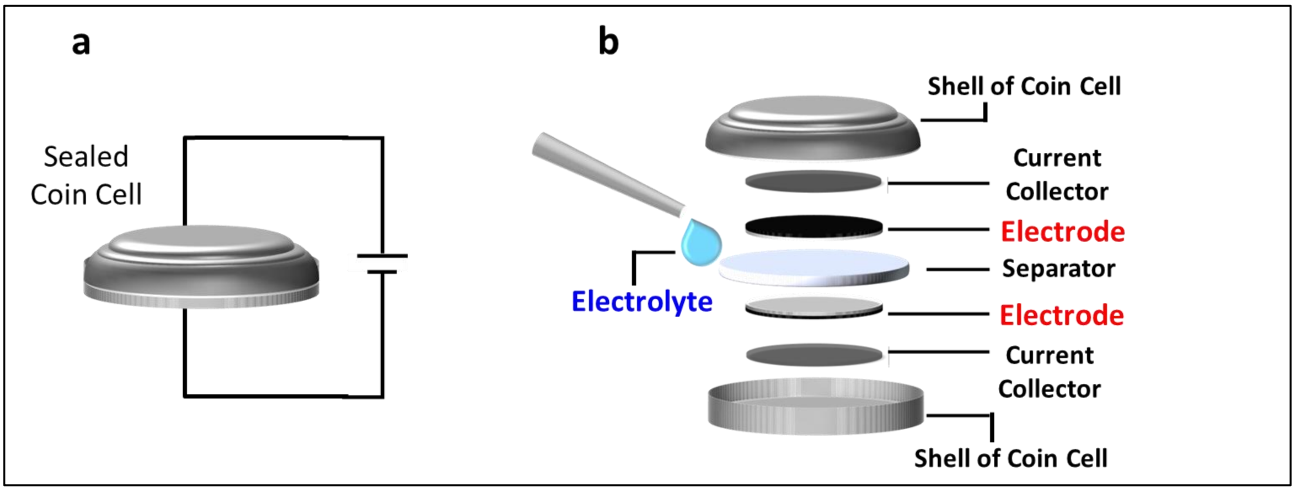

Fig. 2 Schematic of (a) the two-electrode configuration in the form of a sealed coin cell and (b) its inside structure.

The three-electrode configuration is shown in Fig.3. A specific voltage can be applied between positive and negative electrode. At the same time, the potential of positive electrode vs. reference electrode, which is silver-silver ion electrode in our study, is detected by the voltmeter and the current through positive and negative electrode is detected by the amperemeter. The potential of negative electrode is calculated from the difference between applied voltage and the potential of positive electrode. The three-electrode configuration is mainly used to evaluate the performance of positive and negative electrode separately, which can reflect the behaviors of anions and cations, respectively.

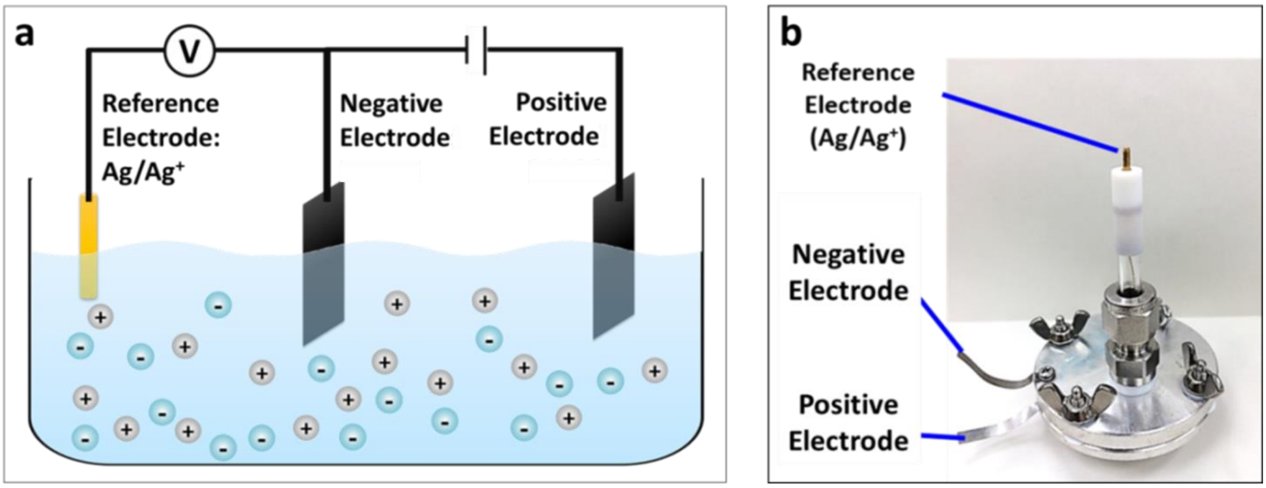

Fig. 3 (a) Schematic and (b) photograph of three-electrode configuration for the measurement of specific capacitance on two electrodes.

2.2.3 Galvanostatic Charge-Discharge Curves (GCC) in Two-Electrode Configuration

In a galvanostatic charging-discharging experiment, a supercapacitor is charged to a specific voltage and then discharged to 0V at a constant current. From the experiment, a GCC is plotted as voltage vs. time, in which the slope of the curve ($\frac{dU}{dt}$) is constant and is defined by Eqn. 4:

$$\frac{dU}{dt} = \frac{I}{C} \tag{4}$$

In which I is the constant current density and C is the specific capacitance of the supercapacitor. Thus the capacitance can be calculated from GGC with a known current and it is one of the most commonly used to achieve the capacitance as well as evaluate the energy density according to Eqn. 6 in Chapter 1.

2.2.4 Galvanostatic Charge-Discharge Curves (GCC) in Three-Electrode Configuration

The measurement of GCC three-electrode configuration, which consist of positive, negative and reference electrode, is similar with that in two-electrode one. It is a charge-discharge process with a constant current. The difference is that we can simultaneously detect the variation of potential versus the reference electrode on positive and negative electrode separately as shown in Fig. 4.

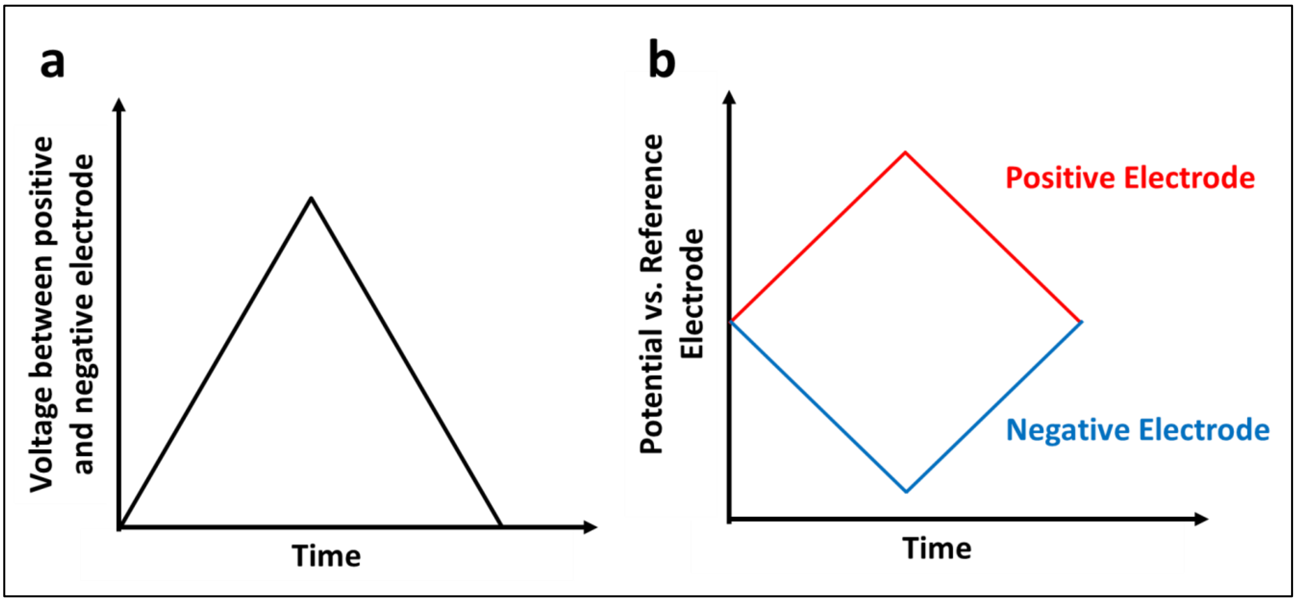

Fig. 4 (a) Variation of voltage between positive and negative electrodes and (b) simultaneously detected variation of potential on positive (red) and negative (blue) electrode. When the supercapacitor is charged, the positive electrode is charged to positive potential while the negative electrode is charged to negative potential.

References

[1] H.-L. Lee and N. T. Flynn, “X-RAY PHOTOELECTRON SPECTROSCOPY,” in *Handbook of Applied Solid State Spectroscopy*, D. R. Vij, Ed. Boston, MA: Springer US, 2006, pp. 485–507.M. S. Dresselhaus, A. Jorio, M. Hofmann, G. Dresselhaus, and R. Saito, “Perspectives on carbon nanotubes and graphene Raman spectroscopy,” *Nano Letters*, vol. 10, no. 3. pp. 751–758, 2010.

[2] C. S. Fadley, “X-ray photoelectron spectroscopy: Progress and perspectives,” *J. Electron Spectros. Relat. Phenomena*, vol. 178–179, no. C, pp. 2–32, 2010.

[3] L. W. D. Graf, F. Molitor, K. Ensslin, C. Stampfer, A. Jungen, C. Hierold, “Spatially Resolved Raman Spectroscopy of Single- and Few-Layer Graphene,” *Nano Lett.*, vol. 7, no. 2, pp. 238–242, 2007.

[4] I. Calizo, I. Bejenari, M. Rahman, G. Liu, and A. A. Balandin, “Ultraviolet Raman microscopy of single and multilayer graphene,” *J. Appl. Phys.*, vol. 106, no. 4, 2009.

[5] M. Yudasaka, T. Ichihashi, D. Kasuya, H. Kataura, and S. Iijima, “S tructure changes of single-wall carbon nanotubes and single-wall carbon nanohorns caused by heat treatment,” *Carbon N. Y.*, vol. 41, pp. 1273–1280, 2003.

[6] R. Reichelt, “Scanning Electron Microscopy,” in *Science of Microscopy*, P. W. Hawkes and J. C. H. Spence, Eds. New York, NY: Springer New York, 2007, pp. 133–272.

[7] H. Seiler, “Secondary electron emission in the scanning electron microscope,” *J. Appl. Phys.*, vol. 54, no. 11, 1983.

[8] K. Sing, “The use of nitrogen adsorption for the characterisation of porous materials,” *Colloids Surfaces A Physicochem. Eng. Asp.*, vol. 187–188, pp. 3–9, 2001.

[9] M. Lawrence and Y. Jiang, *Bio-aggregates Based Building Materials* (2017), Chapter 2.

[10] C. Lastoskie, K. E. Gubbins, and N. Quirke, “Pore size distribution analysis of microporous carbons: a density functional theory approach,” *J. Phys. Chem.*, vol. 97, no. 18, pp. 4786–4796, 1993.

[11] B. Schwenzer, S. N. Kerisit, and M. Vijayakumar, “Anion pairs in room temperature ionic liquids predicted by molecular dynamics simulation, verified by spectroscopic characterization,” RSC Adv., vol. 4, no. 11, pp. 5457–5464, 2014.

[12] R. P. Matthews et al., “A structural investigation of ionic liquid mixtures,” Phys. Chem. Chem. Phys., vol. 18, no. 12, pp. 8608–8624, 2016.

[13] B. Dyatkin, E. Mamontov, K. M. Cook, and Y. Gogotsi, “Capacitance, charge dynamics, and

electrolyte-surface interactions in functionalized carbide-derived carbon electrodes," Prog. Nat. Sci. Mater. Int., vol. 25, no. 6, pp. 631–641, 2015.

[14] X. Wang, H. Zhou, E. Sheridan, J. C. Walmsley, D. Ren, and D. Chen, "Geometrically confined favourable ion packing for high gravimetric capacitance in carbon–ionic liquid supercapacitors," Energy Environ. Sci. Energy Environ. Sci, vol. 232, no. 9, pp. 232–239, 2016.

[15] D. T. L. Galhena, B. C. Bayer, S. Hofmann, and G. A. J. Amaratunga, "Understanding capacitance variation in subnanometer pores by in situ tuning of interlayer constrictions," ACS Nano, vol. 10, no. 1, pp. 747–754, 2016.

[16] B. E. Conway, Electrochemical Supercapacitors: Scientific Fundamentals and Technological (1999)

Chapter 3

Carbon Nanotube/Graphene Composite with Adjustable Porous Structures as Electrode Materials in Supercapacitors

3.1. Introduction

Recently, graphene has been recognized as an attractive material as a supercapacitor electrode material due to its excellent conductivity and large specific surface area [1, 2]. The importance of specific surface area A is well demonstrated in the equation: $C = \varepsilon A/d$, in which C is specific capacitance, ε is permittivity, and d is the separation between the double layers formed by the electric charges at the interface between the electrode surface and electrolyte. In our continuing efforts to develop graphene supercapacitors with high energy density, many methods have been explored to enlarge the specific surface area of graphene materials by preventing the re-stacking of graphene layers. For example, one approach is to fabricate a spherical structure of graphene by using a polystyrene template [3]. Another approach is to insert spacers, such as manganese dioxide [4], polyaniline [5], and/or carbon nanotubes (CNTs) [6-8] between graphene layers. CNTs have been demonstrated as an effective spacer.

To further enlarge the specific surface area of CNT/graphene composites, it is necessary to eliminate the aggregation of CNTs and to improve the interfacial coupling between CNTs and graphene oxide (GO) before co-reduction. Several research groups have preferred to introducing covalent bonds between GO and CNTs [9]. But it requires special conditions, such as extremely low temperature or an inert gas atmosphere. Another commonly used method is to oxidize the CNTs since the oxygen-containing functional groups can reduce the tendency for aggregation of CNTs in water [10]. Besides, the oxidation makes the CNTs more hydrophilic so that it is easier to combine CNTs with GO by hydrogen bonds in water [11]. In the present study, we have selected the oxidation method to improve the dispersity of multi-wall carbon nanotubes (MWNTs). Porous CNT/graphene materials have been obtained by co-reduction of oxidized MWNT/GO composites. We have designed and synthesized CNT/graphene composites by reducing oxidized MWNT/GO (RMGO) composites and introduced various controlled pore structures by adjusting the ratio of oxidized MWNTs to GO. As a result, the specific surface area A has been increased by 153 % compared with prepared graphene.

According to the mechanism of energy storage in supercapacitors, the energy density E can be expressed by the equation $E = CU^2/2$, in which U is the working voltage across the anode and cathode. In this section, the C has been enlarged by the using of oxidized MWNTs as spacers. To further boost the value of E, we have preferred a kind of ionic liquids as the electrolyte due to its higher electrochemical stable window than aqueous and organic ones [2, 12]. The electrochemical performance of prepared CNT/graphene composites as supercapacitor electrodes were investigated in 1-ethyl-3-methylimidazolium tetrafluoroborate (EMI-BF_4) electrolyte. With an optimized spacer content of 20%, the prepared CNT/graphene composite shows a high specific capacitance of 206 F g^{-1} as well as an excellent rate capability.

3.2. Experimental

3.2.1. Synthesis of Materials

Graphite was purchased commercially from Alfa Aesar and MWNTs were purchased from Cheap Tubes Inc. Other chemicals were purchased from Wako Pure Chemical Industries, Ltd. Graphite oxide was generated from the oxidation of graphite by a modified Hummers' method [8,13], in which sodium nitrate ($NaNO_3$), sulfuric acid (H_2SO_4), potassium permanganate ($KMnO_4$), and hydrogen peroxide (H_2O_2) were used as oxidizing agents. After sonication in water, the graphite oxide was exfoliated and an aqueous suspension of graphene oxide (GO) was obtained [14].

The multiwall carbon nanotubes (MWNTs) were oxidized by a mixture of nitric acid (HNO_3) and sulfuric acid (H_2SO_4) (1:3) [15]. In detail, 120 mg of MWNTs were first added in 100 mL of the mixed acid. After refluxing at 80°C for 24 hours, the obtained suspension was diluted with deionized water and dialyzed in deionized water until it became neutral. The pore size of the dialysis tube was 1 nm. The suspensions of GO and oxidized MWNTs were then mixed by sonication and further reduced by hydrazine at 98 °C for 24 hours. After rinsing with deionized water for several times and drying under vacuum overnight, the final product of reduced oxidized MWNT/GO (RMGO) composite was obtained as black powders. The mass ratio of oxidized MWNTs to GO was adjusted to 1/12, 1/10, 1/8, 1/6, and 1/4 to obtain corresponding product designated as RMGO-12, RMGO-10, RMGO-8, RMGO-6, and RMGO-4, respectively. As a reference, reduced GO (RGO) without CNT was also synthesized by the same process. Fig.1 shows a schematic of the synthesis process.

3.2.2. Characterizations

The morphology of materials was examined by scanning electron microscope (SEM, JEOL JSM-6500F). Raman spectroscopy (λ= 532 nm, Nanophoton Raman Plus) was used to characterize the structural features of the materials. The specific surface area and pore distribution were measured by the nitrogen adsorption-desorption method (Quantachrome autosorb *i*Q). Surface chemistry of the materials was characterized by X-ray photoelectron spectroscopy (XPS, ULVAC-PHI Quantera SXM) with a twin anode Al Kα X-ray source and hemispherical energy analyzer. The energies were calibrated against the aliphatic carbon C1s peak at 284.5 eV.

To fabricate an electrode the suspension in ethanol was filtered onto a porous filter membrane (0.2 μm, PTFE). After vacuum drying, the filtered films were cut into circular disks with a diameter of 15 mm and a weight of about 0.8 mg for each electrode. Performance of supercapacitors was characterized in the form of a coin cell. All electrochemical characterization was carried out using an electrochemical workstation (Biologic VSP-300). The ionic liquid electrolyte used in our study, 1-ethyl-3-methylimidazolium tetrafluoroborate (EMI-BF_4) with purity 99.9%, was purchased commercially from Toyo-Gosei. The chemical structure of ions in EMI-BF_4 is shown in Fig.2.

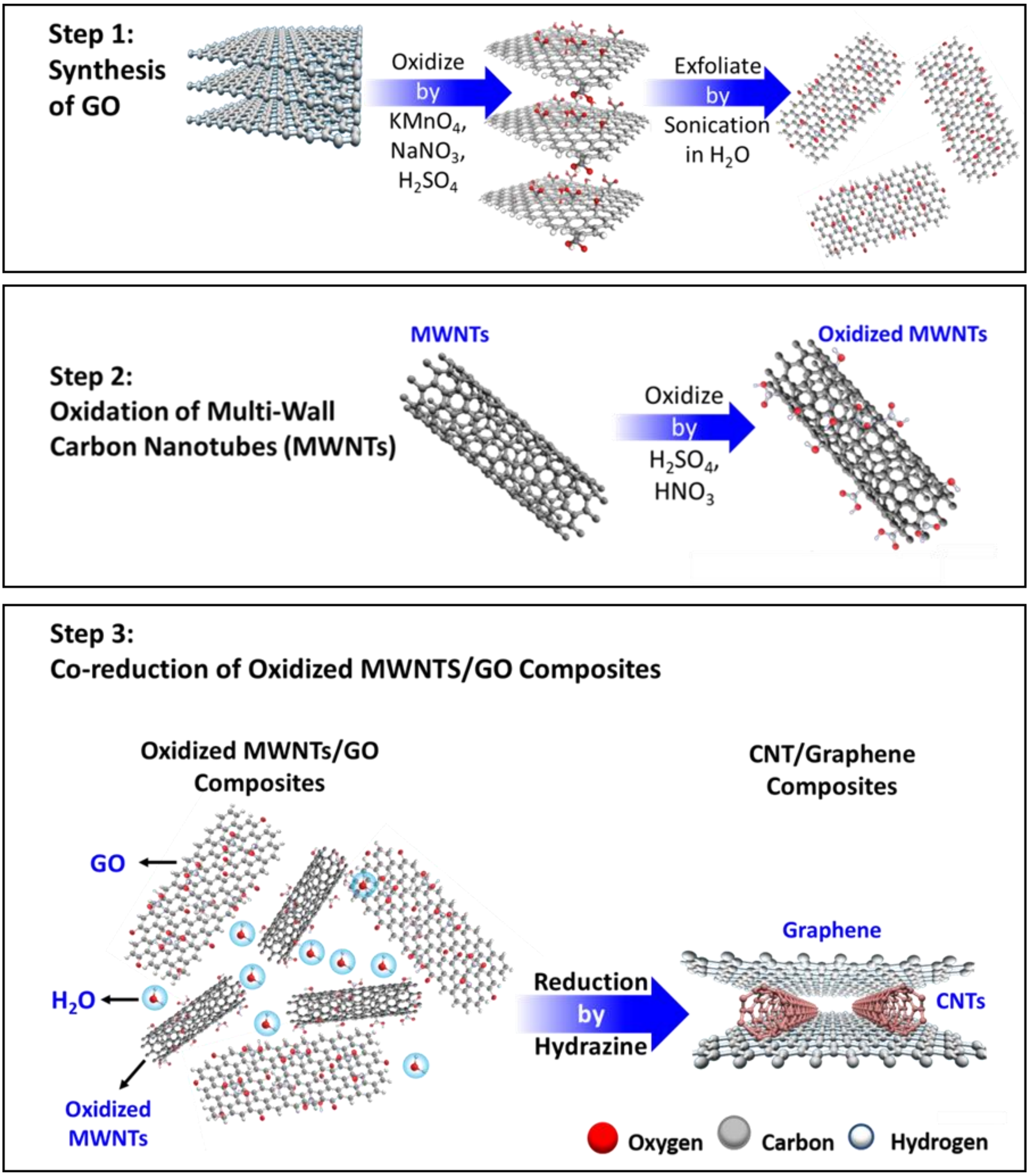

Fig.1 The schematic of synthesis of graphene oxide, oxidized MWNTs, and reduced oxidized MWNT/GO composite.

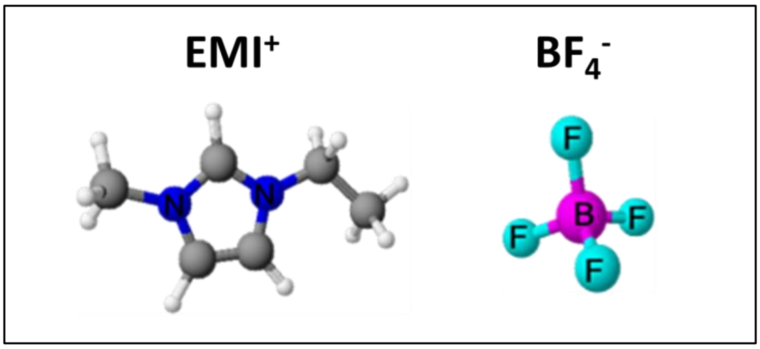

Fig.2 Chemical structures of ions in EMI-BF_4 electrolyte.

3.3. Results and Discussion

3.3.1. Effect of Oxidation on MWNTs

Fig. 3 shows a photograph of the suspension of oxidized MWNTs. The Tyndall effect can be observed clearly, indicating that it is indeed a uniform colloid. The dominant types of functional groups generated during the oxidation process are C=O and C-N as revealed by XPS characterization shown in Fig. 4. It is the hydrophilic functional groups that improve the dispersity of oxidized MWNTs in water. Raman spectra given in Fig. 5 show that the graphitic defects in oxidized MWNTs are much more than the pristine MWNTs because the intensity of the D peak increased significantly after oxidation [16]. Since the structure of carbon nanotubes is retained after oxidization as shown in Fig. 6, we suggest the increased defective structures are mainly due to the covalent bonding between carbon and heteroatoms rather than the damaged graphitic structure [17].

Fig.3 Photograph of aqueous suspension of oxidized MWNTs. The Tyndall effect is observed, indicating that the suspension is a uniform colloid.

Table 1. Ratio of oxygen to carbon in materials characterized by XPS

Materials	Ratio of O to C (%)
MWNT	3.1
Oxidized MWNT	69.8
RGO	10.5
RMGO-4	11.7

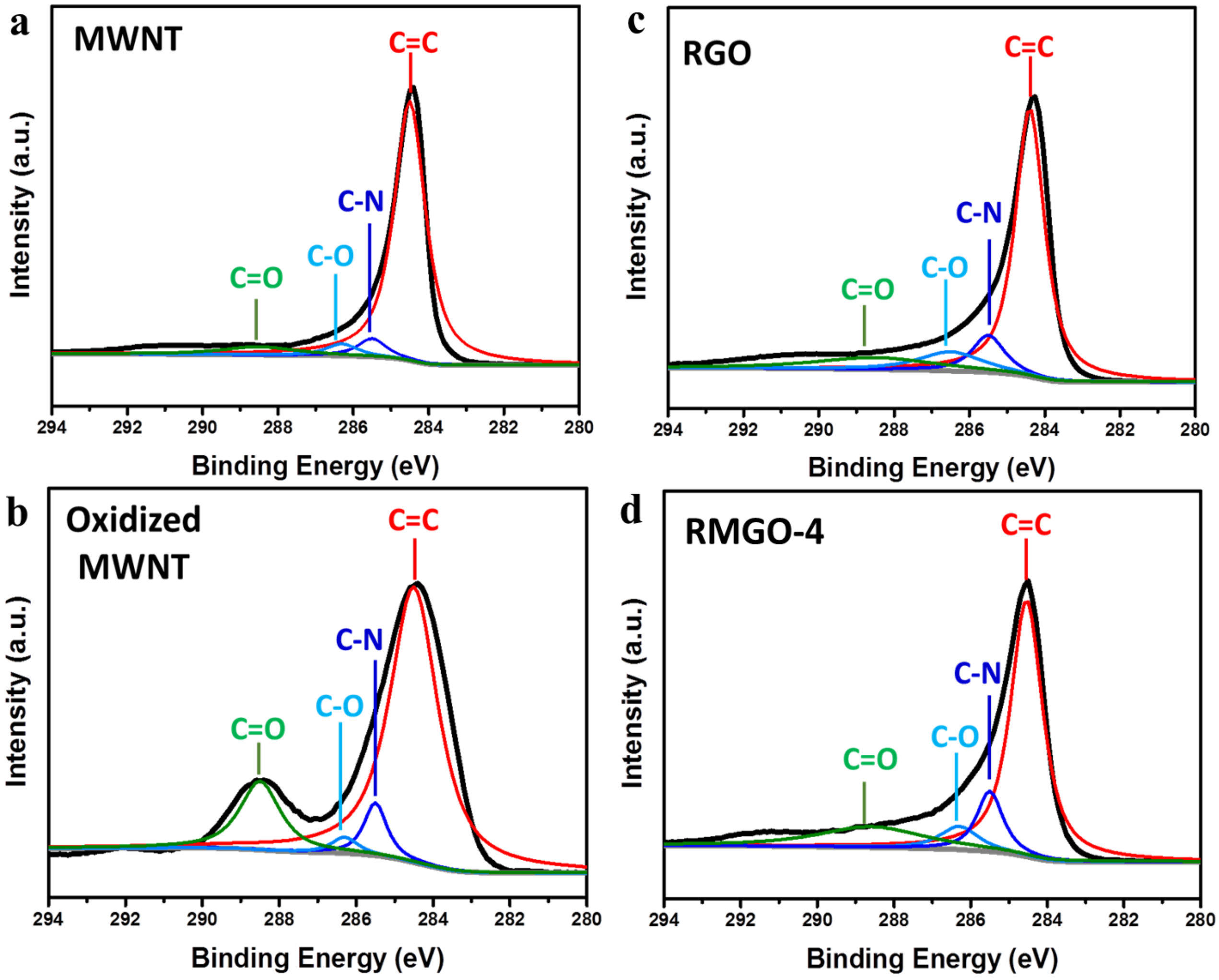

Fig.4 XPS spectra of (a) MWNTs, (b) oxidized MWNTs, (c) CRGO, and (d) RMGO-4 composite. After oxidation, the peaks due to C=O and C-N in oxidized MWNTs have a significant increase compared with pristine MWNTs. These hydrophilic functional groups contribute to the better dispersion of oxidized MWNTs in water. The XPS spectra of RMGO-4 (d) is similar to that of RGO (c) and it indicates that most functional groups on oxidized MWNTs can be removed during reduction.

3.3.2. Characterization of Reduced Materials

After chemical reduction, most C=O functional groups are removed (Fig. 4) and the ratio of oxygen to carbon is similar in RGO and RMGO-4 (Table 1). It indicates that the oxidized MWNTs do not introduce additional oxygen into the composite, which could trigger redox reactions in subsequent electrochemical processes [18–20]. The similar chemical structure also leads to the similar Raman spectra for RGO and RMGO-4 since the defects are mainly from the functional groups. The intensity ratio of the D peak and G peak (I_D/I_G) is 1.23 and 1.27 in RGO and RMGO-4, respectively. The similar value of I_D/I_G shows that CNTs in prepared composites have the similar defects with RGO since the reduction process is the same.

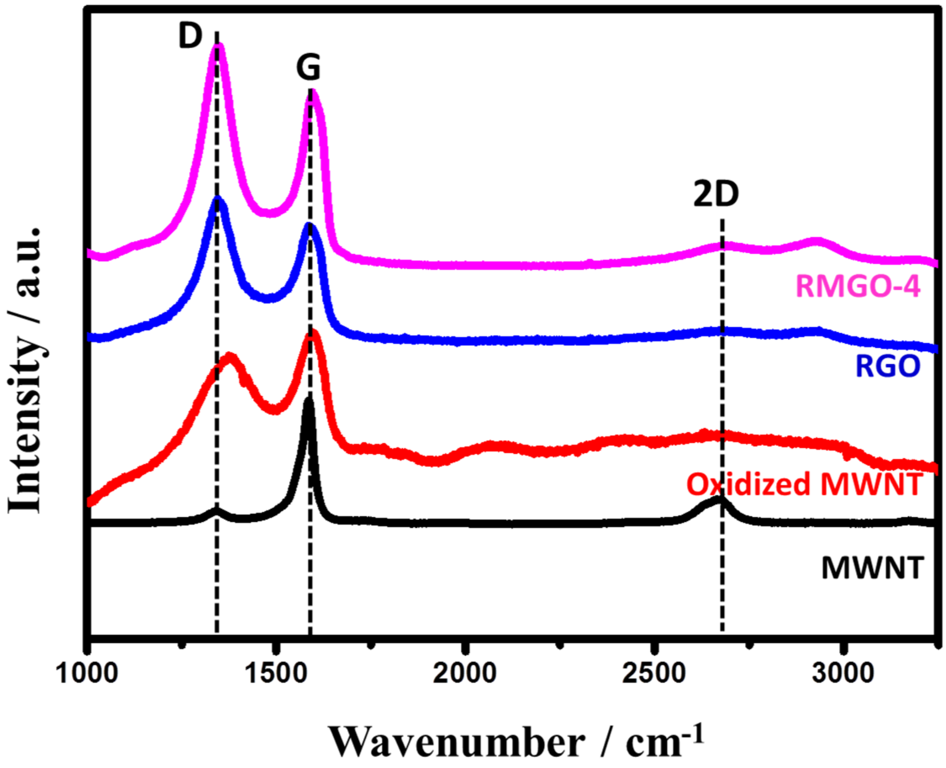

Fig.5 Raman spectra of MWNTs, oxidized MWNTs, RGO, and RMGO-4. The spectra of MWNTs and oxidized MWNTs show that oxidation of MWNTs produced more defects on nanotubes. The similar intensity ratio of D peak to G peak (I_D/I_G) in RGO and RMGO-4 indicates that the CNTs in prepared composites have similar defects with RGO since the reduction process is the same. The I_D/I_G ratios are 1.23 and 1.27, respectively.

Fig. 7 shows the pore distribution and specific surface area (*A*) of the reduced materials. For pores smaller than 1nm, namely micropores [23], the value of *A* increases with the ratio of spacers until the ratio reaches 1/6. On the other hand, the largest *A* of pores larger than 1nm, namely mesopore, is achieved when the ratio is 1/8 (Table 2). We discuss the variation trend of *A* in detail. Firstly, we suppose that the micropores mainly come from the partially-spaced graphene layers while mesopores are from the fully-spaced pores and slit between flakes (Fig.8a). At the beginning, the *A* of both micropores and mesopores increases with oxidized MWNTs since both stacked graphene layers and partially spaced ones are further spaced (Fig. 8b).

However, when the ratio is larger than 1/8, more micropores instead of mesopores are formed due to smaller distance between neighboring nanotubes (Fig.8c). When the ratio further increases, the excessive amount of oxidized MWNTs tends to aggregate again after reduction, leading to the decrease of pores [7, 21]. As a result, we have achieved the largest *A*, 742 $m^2\ g^{-1}$, when the ratio of oxidized MWNTs is 1/6.

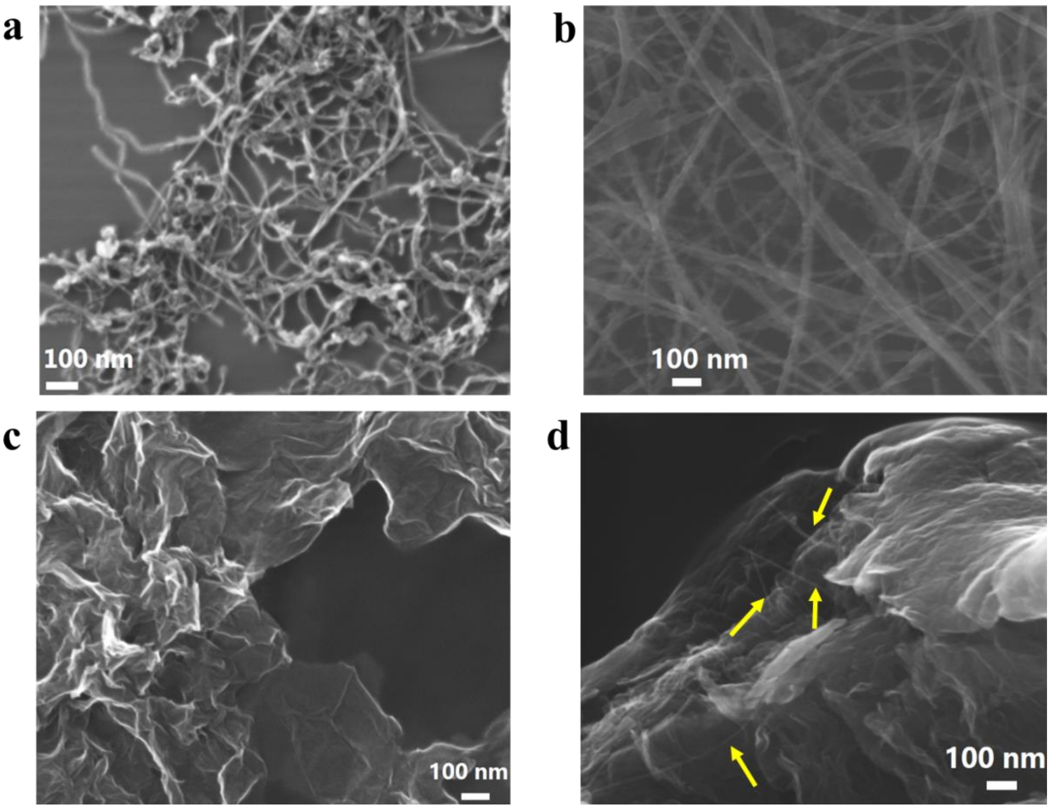

Fig. 6 SEM image of (a) pristine MWNTs, (b) oxidized MWNTs, (c) CRGO, and (d) RMGO-4 composite. The CNTs can be clearly observed in the composite (indicated by arrow in d).

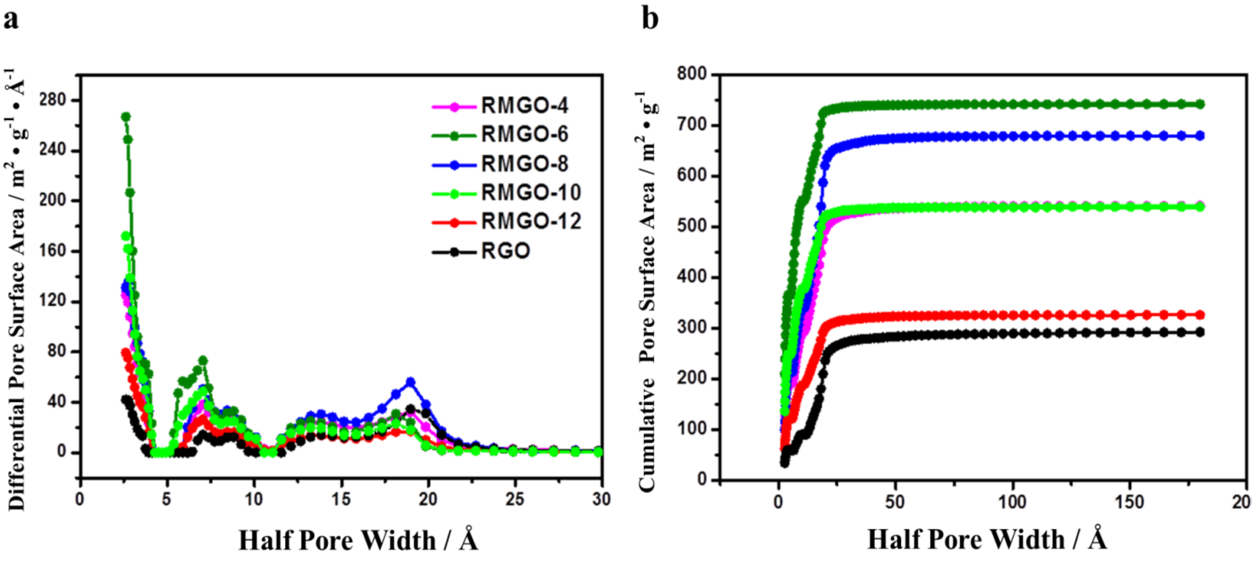

Fig. 7 Pore distribution of graphene electrode. (a) Differential pore surface area and (b) cumulative pore surface area. The radius of pores in graphene electrode is smaller than 2.5 nm.

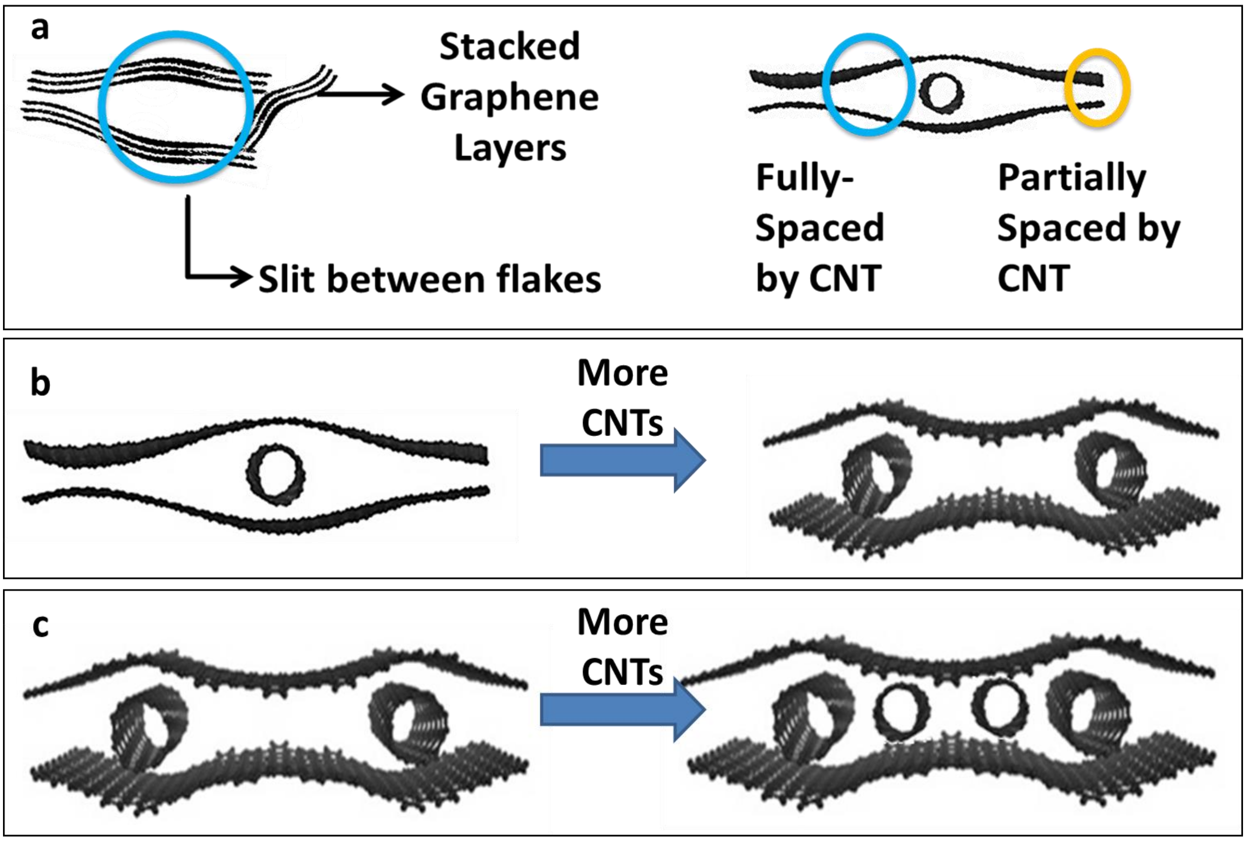

Fig.8 Schematic of variation trend of pore distribution with ratio of CNTs. (a) shows the generation of mesopores and micropores. (b) shows the further spaced graphene layers due to increased spacers. (c) shows the smaller distance between CNTs when we continue increasing the spacers.

Table 2. Specific Surface Area of Electrode Materials

Electrode Materials	Specific Surface Area (A) / $m^2\ g^{-1}$	$A_{(r < 1\ nm)}$/ $m^2\ g^{-1}$	$A_{(r > 1\ nm)}$/ $m^2\ g^{-1}$
RGO	293	90	203
RMGO-12	327	189	138
RMGO-10	540	379	161
RMGO-8	680	341	339
RMGO-6	742	553	189
RMGO-4	542	293	249

3.3.3. Performance of Reduced Materials in Supercapacitors

The performance of materials in supercapacitors is characterized by the charge-discharge process at constant current and the cyclic voltammetry (CV) from 0 to 3.7 V. The CV curves of reduced materials (Fig. 9) are rectangular, indicating that the capacitance of material comes from physical adsorption-desorption of ions rather than the faradic process [22].

Table 3 shows the specific capacitance (*C*) and energy density calculated from the charge-discharge curves at 0.2 A g^{-1}. The value of *C* is enlarged significantly compared with RGO when the ratio of oxidized MWNTs is greater than 1/12 and RMGO-8 exhibits the largest *C* of 213 F g^{-1}, increased by 61% compared with RGO. However, RMGO-4 has the largest *C*, 162 F g^{-1}, at 6.0 A g^{-1} (Table 4) and the second largest *C*, 206 F g^{-1}, at 0.2 A g^{-1}. Therefore, RMGO-4 has the best rate capability at 3.7 V and the capacity retention ratio is 79% as shown in Fig.10.

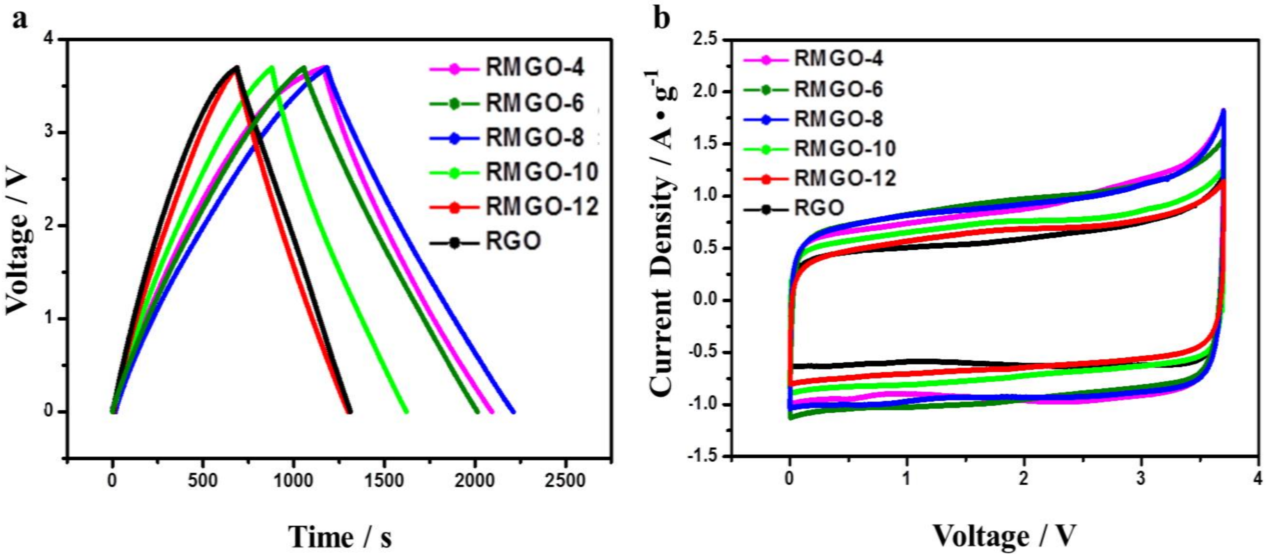

Fig.9 (a) Charge-discharge curves and (b) cyclic voltammetry (CV) curves of supercapacitors with different electrode materials in EMI-BF_4. The current density of charge-discharge process is 0.2 A g^{-1} and the scan rate of CV is 20 mV s^{-1}. The supercapacitors are charged from 0 to 3.7V and RMGO-8 has the largest specific capacitance at 0.2 A g^{-1}.

Table 3. Electrochemical Performance of Supercapacitors in EMI-BF_4 at 0.2 A g^{-1}

Electrode Materials	Specific Capacitance (*C*) / F g^{-1}	Energy Density / Wh kg^{-1}
RGO	132	63
RMGO-12	130	62
RMGO-10	160	76
RMGO-8	213	101
RMGO-6	204	97
RMGO-4	206	98

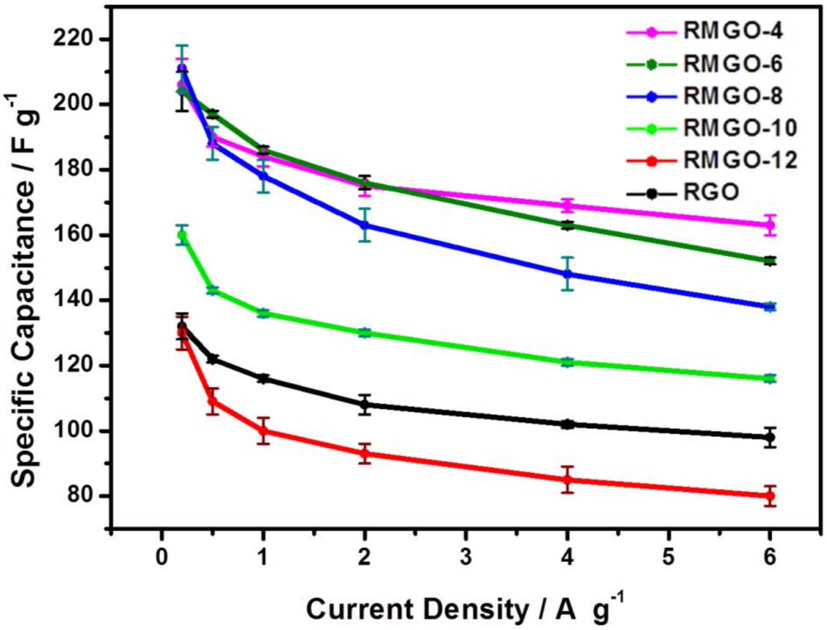

Fig.10 Rate capability of electrode materials in EMI-BF$_4$. The current density is from 0.2 to 6.0 A g^{-1}. RMGO-4 has better rate capability than RMGO-6 and RMGO-8 even though RMGO-8 has the largest specific capacitance at 0.2 A g^{-1}. The retention of RMGO-4 is 79% and the error bat is the standard deviation.

Table 4. Electrochemical Performance of Supercapacitors in EMI-BF$_4$ at 6.0 A g^{-1}

Electrode Materials	Specific Capacitance (C) / F g^{-1}	Energy Density / Wh kg^{-1}
RGO	98	47
RMGO-12	80	38
RMGO-10	116	55
RMGO-8	137	65
RMGO-6	152	72
RMGO-4	163	77

It is worth noting that RMGO-6 does not give the largest specific capacitance C even though it has the largest specific surface area A of 742 m^2 g^{-1}. As already discussed in the literature [23–28], the lack of linearity between C and A is mainly due to the mechanism that the capacitance from the double layers in various pores is different. In another word, the pores with different sizes have different contributions to the total value of specific capacitance C. The relationship between pore structure and specific capacitance will be discussed in details in the next section.

3.4. Conclusions

In summary, we have designed and prepared CNT/graphene composites with various CNT/graphene mass ratios through a facile solution synthesis method. The improved dispersity of oxidized MWNTs in water contributes to the enlarged specific surface area (*A*). The value of *A* increases with the ratio of spacers until 1/16 and largest one from RMGO-6 is 742 m^2 g^{-1}. The excessive amount of CNT tends to aggregate again and leads to the decreased *A* when the ratio increases to 1/4. Meanwhile, RMGO-4 shows a high specific capacitance of 206 F g^{-1} at current density of 0.2 A g^{-1} and the best rate capability with 79% capacitance retention at 6.0 A g^{-1} in an EMI-BF_4 electrolyte, even though its specific surface area is smaller than that of RMGO-6. An explanation of this phenomenon has been built that the capacitance in different pores is not the same. Therefore, the pore distribution will also affect the specific capacitance except for the specific surface area of total pores.

References

[1] G. Wang, L. Zhang, and J. Zhang, "A review of electrode materials for electrochemical supercapacitors," *Chem. Soc. Rev.*, vol. 41, no. 2, pp. 797–828, 2012.

[2] J. Hou, Y. Shao, M. W. Ellis, R. B. Moore, and B. Yi, "Graphene-based electrochemical energy conversion and storage: fuel cells, supercapacitors and lithium ion batteries.," *Phys. Chem. Chem. Phys.*, vol. 13, no. 34, pp. 15384–15402, 2011.

[3] Q. Shao, J. Tang, Y. Lin, F. Zhang, J. Yuan, H. Zhang, N. Shinya, and L.-C. Qin, "Synthesis and characterization of graphene hollow spheres for application in supercapacitors," *J. Mater. Chem. A*, vol. 1, no. 48, pp. 15423–15428, 2013.

[4] Q. Cheng, J. Tang, J. Ma, H. Zhang, N. Shinya, and L.-C. Qin, "Graphene and nanostructured MnO2 composite electrodes for supercapacitors," *Carbon*, vol. 49, no. 9, pp. 2917–2925, 2011.

[5] Q. Cheng, J. Tang, N. Shinya, and L.-C. Qin, "Polyaniline modified graphene and carbon nanotube composite electrode for asymmetric supercapacitors of high energy density," *J. Power Sources*, vol. 241, pp. 423–428, 2013.

[6] Q. Cheng, J. Tang, J. Ma, H. Zhang, N. Shinya, and L.-C. Qin, "Graphene and carbon nanotube composite electrodes for supercapacitors with ultra-high energy density," *Phys. Chem. Chem. Phys.*, vol. 13, no. 39, pp. 17615–17624, 2011.

[7] Q. Shao, J. Tang, Y. Lin, J. Li, J. Yuan, H. Zhang, N. Shinya, and L.-C. Qin, "Carbon nanotube spaced graphene aerogels with enhanced capacitance in aqueous and ionic liquid electrolytes," *J. Power Sources*, vol. 278, pp. 751–759, 2015.

[8] F. Zhang, J. Tang, N. Shinya, and L.-C. Qin, "Hybrid graphene electrodes for supercapacitors of high energy density," *Chem. Phys. Lett.*, vol. 584, pp. 124–129, 2013.

[9] M. Kotal and A. K. Bhowmick, "Multifunctional Hybrid Materials Based on Carbon Nanotube Chemically Bonded to Reduced Graphene Oxide," *J. Phys. Chem. C*, vol. 117, no. 48, pp. 25865–25875, 2013.

[10] B. You, L. Wang, L. Yao, and J. Yang, "Three-dimensional N-doped graphene-CNT networks for supercapacitor.," *Chem. Commun. (Camb).*, vol. 49, no. 44, pp. 5016–8, 2013.

[11] N. V. Medhekar, A. Ramasubramaniam, R. S. Ruoff, and V. B. Shenoy, "Hydrogen bond networks in graphene oxide composite paper: Structure and mechanical properties," *ACS Nano*, vol. 4, no. 4, pp. 2300–2306, 2010.

[12] R. Hayes, G. G. Warr, and R. Atkin, “Structure and Nanostructure in Ionic Liquids,” *Chemical Reviews*, vol. 115, no. 13. pp. 6357–6426, 2015.

[13] W. S. Hummers and R. E. Offeman, “Preparation of Graphitic Oxide,” *J. Am. Chem. Soc.*, vol. 80, no. 6, pp. 1339–1339, 1958.

[14] J. Song, X. Wang, and C.-T. Chang, “Preparation and characterization of graphene oxide paper,” *J. Nanomater.*, vol. 448, no. 7152, pp. 457–60, 2007.

[15] Y. K. Kim and D. H. Min, “Preparation of scrolled graphene oxides with multi-walled carbon nanotube templates,” *Carbon*, vol. 48, no. 15, pp. 4283–4288, 2010.

[16] M. S. Dresselhaus, A. Jorio, M. Hofmann, G. Dresselhaus, and R. Saito, “Perspectives on carbon nanotubes and graphene Raman spectroscopy,” *Nano Lett.*, vol. 10, no. 3. pp. 751–758, 2010.

[17] K. N. Kudin, B. Ozbas, H. C. Schniepp, R. K. Prudhomme, I. A. Aksay, and R. Car, “Raman spectra of graphite oxide and functionalized graphene sheets,” *Nano Lett.*, vol. 8, no. 1, pp. 36–41, 2008.

[18] P. Azaïs, L. Duclaux, P. Florian, D. Massiot, M.-A. Lillo-Rodenas, A. Linares-Solano, J.-P. Peres, C. Jehoulet, and F. Beguin, “Causes of supercapacitors aging in organic electrolyte,” *J. Power Sources*, vol. 171, no. 2, pp. 1046–1053, 2007.

[19] W. Ai, W. Cao, Z. Sun, J. Jiang, Z. Du, L. Xie, Y. Wang, X. Wang, H. Zhang, W. Huang, and T. Yu, “Redox-crosslinked graphene networks with enhanced electrochemical capacitance,” *J. Mater. Chem. A*, vol. 2, no. 32, pp. 12924–12930, 2014.

[20] H. Tateishi, M. Koinuma, S. Miyamoto, Y. Kamei, K. Hatakeyama, C. Ogata, T. Taniguchi, A. Funatsu, and Y. Matsumoto, “Effect of the electrochemical oxidation/reduction cycle on the electrochemical capacitance of graphite oxide,” *Carbon*, vol. 76, pp. 40–45, 2014.

[21] Y. Wang, Y. Wu, Y. Huang, F. Zhang, X. Yang, Y. Ma, and Y. Chen, “Preventing graphene sheets from restacking for high-capacitance performance,” *J. Phys. Chem. C*, vol. 115, no. 46, pp. 23192–23197, 2011.

[22] Y. He, J. Huang, B. G. Sumpter, A. a Kornyshev, and R. Qiao, “Dynamic Charge Storage in Ionic Liquids-Filled Nanopores: Insight from a Computational Cyclic Voltammetry Study,” *J. Phys. Chem. Lett.*, vol. 6, pp. 22–30, 2015.

[23] N. Jackel, M. Rodner, A. Schreiber, J. Jeongwook, M. Zeiger, M. Aslan, D. Weingarth, and V. Presser, “Anomalous or regular capacitance? The influence of pore size dispersity on double-layer formation,” *J. Power Sources*, vol. 326, pp. 660–671, 2016.

[24] W. Hsieh, T.-L. A. Horng, H.-C. Huang, and H. Teng, “Facile simulation of carbon with wide pore size distribution for electric double-layer capacitance based on Helmholtz models,” *J. Mater. Chem. A*, vol. 3, no. 32, pp. 16535–16543, 2015.

[25] O. Barbieri, M. Hahn, A. Herzog, and R. Kötz, “Capacitance limits of high surface area activated carbons for double layer capacitors,” *Carbon*, vol. 43, no. 6, pp. 1303–1310, 2005.

[26] J. Chmiola, C. Largeot, P. L. Taberna, P. Simon, and Y. Gogotsi, “Desolvation of ions in subnanometer pores and its effect on capacitance and double-layer theory,” *Angew. Chem. Int. Ed.*, vol. 47, no. 18, pp. 3392–3395, 2008.

[27] G. Gryglewicz, J. Machnikowski, E. Lorenc-Grabowska, G. Lota, and E. Frackowiak, “Effect of pore size distribution of coal-based activated carbons on double layer capacitance,” *Electrochim. Acta*, vol. 50, no. 5, pp. 1197–1206, 2005.

[28] J. Chmiola, G. Yushin, R. Dash, and Y. Gogotsi, “Effect of pore size and surface area of carbide derived carbons on specific capacitance,” *J. Power Sources*, vol. 158, no. 1, pp. 765–772, 2006.

Chapter 4

Ionic behaviors in Different Pores and Their Different Contributions to Specific Capacitance

4.1. Introduction

It is well known that the large specific capacitance of supercapacitors requires the large specific surface area of electrode materials according to the equation: $C = \varepsilon A/d$, where C is specific capacitance, ε is permittivity, and d is the separation between the double layers formed by the electric charges at the interface between the electrode surface and electrolyte. That's why we have preferred porous CNT/graphene composites. However, there have been reports reporting that a greater specific surface area does not always lead to larger specific capacitance [1–3]. The characteristic structural features of the pores, i.e., the size and distribution of pores, have affected strongly whether the pores can successfully adsorb and desorb ions, which is of fundamental importance for supercapacitors [3]. In another word, the specific capacitance is proportional to the specific surface area of accessible pores rather than that of total pores. Besides, the specific capacitance provided by accessible pores could be different in pores with structures. It depends on the different ionic behaviors in different pores. According to several reported discussions [4-6], the pores in the range of ion size and solvated size could contribute the most to specific capacitance in aqueous or organic electrolytes. The additional capacitance in this type of pores is suggested to be due to the desolvation of ions. Unfortunately, this conclusion is difficult to be applied in supercapacitors based on ionic liquid since no solvent is used in this kind of electrolyte. Namely, ions are not solvated at all in ionic liquids.

To address this issue, we have taken a linear fitting between capacitance per area and the surface area ratio of different pores. In this study, we have chosen reduced oxidized MWNT/GO composites (RMGO), the materials we have discussed in the previous chapter, as electrode materials and an ionic liquid, 1-ethyl-3-methylimidazolium tetrafluoroborate (EMI-BF_4), as the electrolyte. The various pore structures are realized by different ration of oxidized MWNTs. The classification of pores is based on the ratio of pore size to ion size. Considering the larger size of EMI^+ (0.43 × 0.76 nm) than $BF4^-$ (0.48 × 0.48 nm) [7, 8], we have preferred the size of EMI^+ as the standard to classify the pores. It is found that pores with radius larger than 0.76nm, namely twice the size of ions, can make greater contributions to the specific capacitance.

The fitting method above is based on the assumption that the capacitance on positive electrode is equal to that on negative electrode in symmetric supercapacitors. However, the behavior of cation and anion in supercapacitors are usually different in supercapacitors [9-11]. Therefore, we have measured the specific capacitance in positive and negative electrodes separately in a three-electrode system. And the multi-linear fitting method is used to analyze the behaviors of cation and anion in different pores, respectively. Similarly, the pores are also classified by the ratio of pores size to ion size.

4.2. Experimental

The specific surface area and pore distribution were measured by the nitrogen adsorption-desorption method (Quantachrome autosorb *i*Q). All electrochemical characterization was carried out using an electrochemical workstation (Biologic VSP-300). The ionic liquid electrolyte used in our study, 1-ethyl-3-methylimidazolium tetrafluoroborate (EMI-BF_4) with purity 99.9%, was purchased commercially from Toyo-Gosei.

For the linear fitting analysis, the performance of supercapacitors was characterized in the form of a coin cell. And in order to figure out the specific capacitance on both positive and negative electrodes at the same time, the charging-discharging process was performed using a three-electrode system with Ag/Ag+ as the reference electrode and RMGO composite as both the positive and negative electrode.

4.3. Results and Discussion

4.3.1 Ionic behaviors in Different Pores

The specific capacitance (*C*) and specific surface area (*A*) of electrode materials we use for analysis are shown Table 1 and Table 2. They are calculated from charging-discharging curves and diagrams of pore distributions shown in Chapter 3.The lack of linearity is obviously shown in Fig.1, indicating the capacitance is not the same in all kinds of pores.

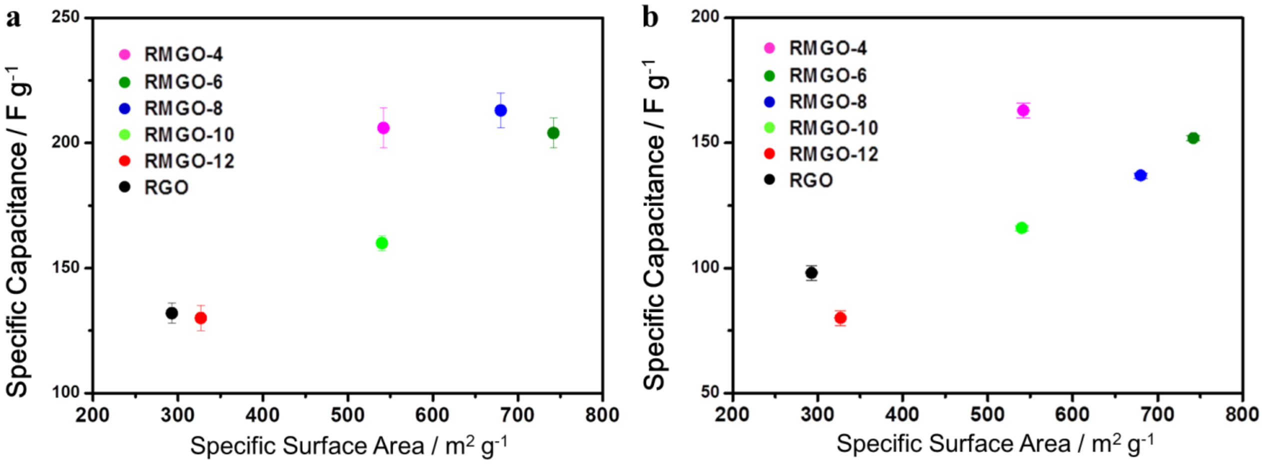

Fig.1 Plot of specific capacitance at (a) 0.2 A g^{-1} and (b) 6.0 A g^{-1} vs. specific surface area. The error bar is the standard deviation.

In electrochemical studies utilizing aqueous and organic electrolytes, the pores are usually classified into micropores ($r < 1$ nm) and mesopores (1 nm $< r <$ 25 nm) since 1 nm, the size of a fully solvated ion [12-14]. The pores smaller than the solvated ion may contribute to an excessive capacitance due to desolvation of ions [7, 13]. A simple model considering the different contributions of micropores and mesopores has been proposed as follows [15, 16]:

$$C = C_{mic}\,A_{mic} + C_{mes}\,A_{mes} \tag{1a}$$

$$\frac{C}{A_{mic}} = C_{mic} + C_{mes}\,\frac{A_{mes}}{A_{mic}} \tag{1b}$$

where C_{mic} and C_{mes} are the capacitance per unit surface area of micropores and the capacitance per unit surface area of mesopores, respectively; A_{mic} and A_{mes} are the specific surface area of micropores and mesopores, respectively.

Table 1. Electrochemical Performance of Supercapacitors in EMI-BF_4 at 0.2 and 6.0 A g^{-1}

Electrode Materials	Specific Capacitance at 0.2 A g^{-1} / F g^{-1}	Specific Capacitance at 6.0 A g^{-1} / F g^{-1}
RGO	132	98
RMGO-12	130	80
RMGO-10	160	116
RMGO-8	213	137
RMGO-6	204	152
RMGO-4	206	163

In the present study, the aforementioned model must be modified because there is no solvent is used in the ionic liquid electrolyte, which means that the electrolyte ions are not surrounded by molecules of solvent. Considering the size of EMI^+ (0.43 × 0.76 nm) and $BF4^-$ (0.48 × 0.48 nm) [7, 17], pores with r smaller than 0.38 nm are difficult to be accessed by EMI^+. And according to several simulations reported in the literature, the capacitance is almost independent of pore size when the ratio of pore size to ion size is greater than 2 [14, 18, 19]. Therefore, we classify the pores into the following two types: One is pores with r in the range between 0.38 and 0.76 nm and the other is pores with r greater than 0.76 nm. As a result, Eqn. 1 is revised correspondingly as follows

$$C = C_{(0.38nm<r<0.76nm)}\,A_{(0.38nm<r<0.76nm)} + C_{(r>0.76nm)}\,A_{(r>0.76nm)} \tag{2a}$$

$$\frac{C}{A_{(0.38nm<r<0.76nm)}} = C_{(0.38nm<r<0.76nm)} + C_{(r>0.76nm)}\,\frac{A_{(r>0.76nm)}}{A_{(0.38nm<r<0.76nm)}} \tag{2b}$$

where $A_{(r > 0.76\ \mathrm{nm})}$ and $A_{(0.38\ \mathrm{nm} < r < 0.76\ \mathrm{nm})}$ are the specific surface area of the two types of pores described above, $C_{(r > 0.76\ \mathrm{nm})}$ and $\mathrm{C}_{(0.38\ \mathrm{nm} < r < 0.76\ \mathrm{nm})}$ are capacitance per unit surface area of the corresponding type of pores. By performing a linear fitting between $C/A_{(0.38\ \mathrm{nm} < \mathrm{r} < 0.76\ \mathrm{nm})}$ and $A_{(\mathrm{r} > 0.76\ \mathrm{nm})} / A_{(0.38\ \mathrm{nm} < r < 0.76\ \mathrm{nm})}$, we obtain $C_{(0.38\ \mathrm{nm} < r < 0.76\ \mathrm{nm})}$ and $C_{(r > 0.76\ \mathrm{nm})}$ from the intercept and slope, respectively.

Table 2. Specific Surface Area of Electrode Materials.

Electrode Material	Specific Surface Area (A) / $\mathrm{m}^2\ \mathrm{g}^{-1}$	$A_{(r < 0.38\ \mathrm{nm})}$ / $\mathrm{m}^2\ \mathrm{g}^{-1}$	$A_{(r > 0.76\ \mathrm{nm})}$ / $\mathrm{m}^2\ \mathrm{g}^{-1}$	$A_{(0.3\ 8\mathrm{nm} < r < 0.76\ \mathrm{nm})}$ / $\mathrm{m}^2\ \mathrm{g}^{-1}$
RGO	293	60	219	14
RMGO-12	327	118	168	41
RMGO-10	540	240	206	94
RMGO-8	680	207	396	77
RMGO-6	742	351	245	146
RMGO-4	542	188	298	56

Fig. 2 shows the results of linear fitting when the current density is 0.2 A g^{-1}. The coefficient of determination (R^2) is 0.984. According to the fitting equation, $C_{(0.38\ \mathrm{nm} < r < 0.76\ \mathrm{nm})}$ and $C_{(r > 0.76\ \mathrm{nm})}$ are 0.441 and 0.572 F m^{-2}, respectively. The smaller capacitance per unit surface area of for pores (0.38 nm < r < 0.76 nm) is attributed to the existence of ion pairs due to stronger ion-ion correlation in ionic liquids [33-36]. In this situation, pores smaller than twice the ionic size are difficult to be utilized by the ion pairs and therefore result in little contribution to the capacitance.

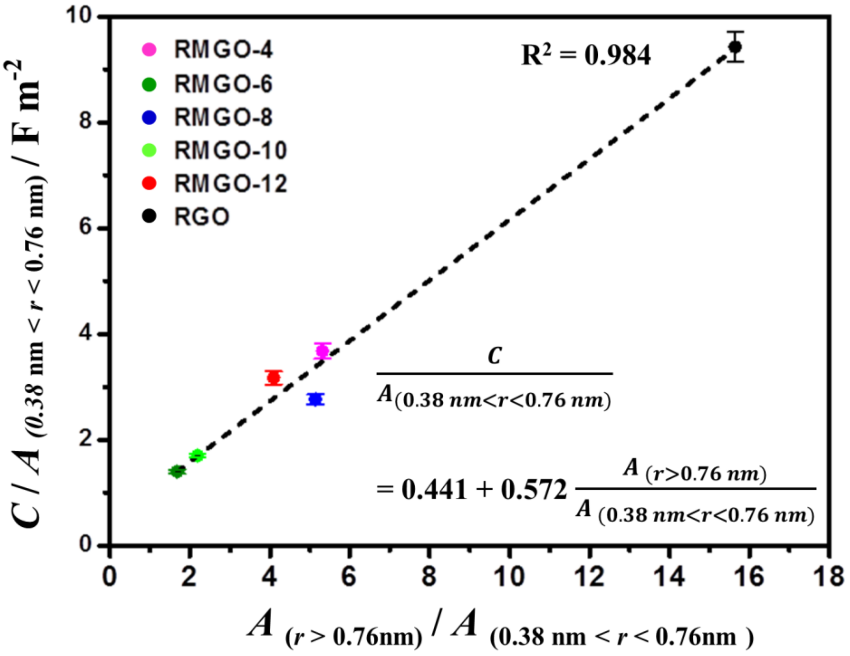

Fig.2 Relationship between pore surface area and specific capacitance at 0.2 A g^{-1}. Dashed line shows linear fitting of $C/A_{(0.38\ \mathrm{nm} < r < 0.76\ \mathrm{nm})}$ vs. $A_{(r > 0.76\ \mathrm{nm})} / A_{(0.38\ \mathrm{nm} < r < 0.76\ \mathrm{nm})}$. The error bar is the standard deviation.

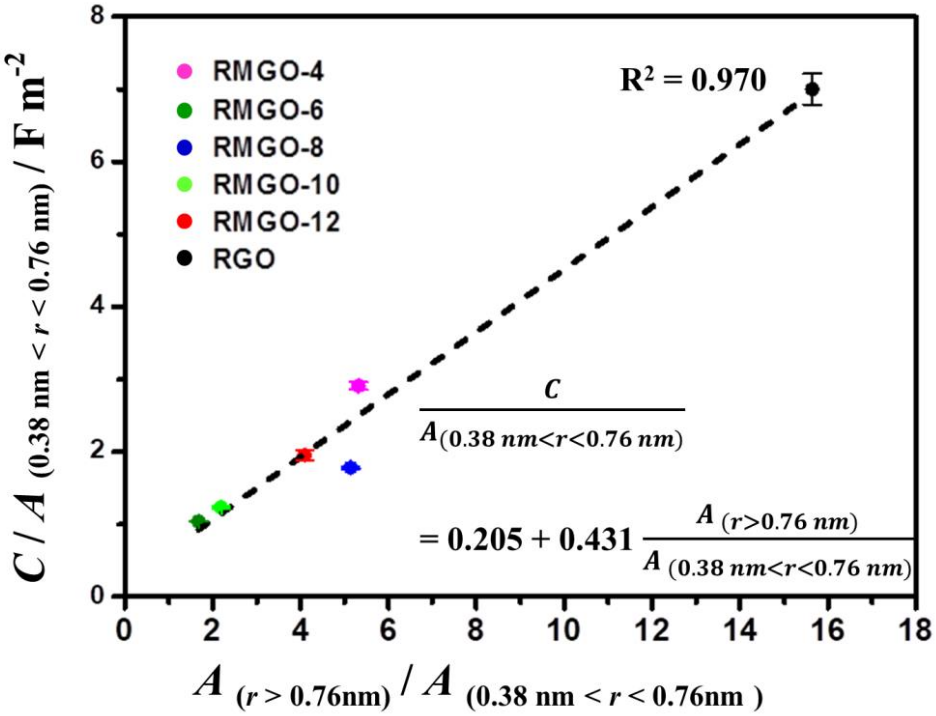

Fig. 3 Relationship between pore surface area and specific capacitance at 6.0 A g^{-1}. Dashed line shows linear fitting of $C/A_{(0.38\text{ nm} < r < 0.76\text{ nm})}$ vs. $A_{(r > 0.76\text{ nm})} / A_{(0.38\text{ nm} < r < 0.76\text{ nm})}$. The error bar is the standard devitation.

However, it should be noted that certain deviations from linear fitting are observed. Both $A_{(0.38\text{ nm} < r < 0.76\text{ nm})}$ and $A_{(r > 0.76\text{ nm})}$ of RMGO-8 are larger than those of RMGO-4 (especially $A_{(r > 0.76\text{ nm})}$, *c.f.* Table 2). Consequently, the value of C at 2.0 A g^{-1} of RMGO-8 is not much greater than that of RMGO. Moreover, the value of C at 6.0 A g-1 of RMGO-8 is actually smaller (Table 1). Since behaviors of s and anions are assumed to be the same in this analysis, we suggest that behaviors of cation and anions are likely to be different in the real situation.

4.3.2 Behaviors of Cation and Anion in Different Pores

According to the mechanism of charge storage of supercapacitors, the capacitance on the negative electrode comes from the adsorption-desorption of cations while the capacitance on the positive one comes from adsorption-desorption of anions. Therefore, the analysis of relationship between specific surface area of different pores and specific capacitance on two electrodes can reflect the behaviors of cations and anions. The specific capacitances calculated from the charging-discharging curves at 0.2 A g^{-1} are shown in Table 3 and Fig. 4. The voltage across positive and negative electrode is from 0 to 3.7 V.

It is worth noting that the specific capacitance of EMI^+ (C_{cation}) is larger than that of BF_4^- (C_{anion}). According to Eqn. (3), $C = \frac{\varepsilon A}{d}$, in which ε is the dielectric constant, A is the specific surface area, and d is the separation between the electric double layers. Since d can be approximated as the ion size in ionic liquids [25] and the size of EMI^+ is actually larger than that of $BF4^-$ [4,8], C_{cation} should be the smaller one if the capacitance on the two electrodes are solely due to the adsorption of isolated cations and anions, respectively. Considering the result we discussed in previous section, this seemingly contradictory phenomenon is because the ions behaved in the form of ion-pair or ion-cluster in pores [26-29]. To clarify the ionic behaviors and their effects on specific capacitance, we have taken the multi-linear fitting between *C* and *A* in different pores.

Table 3. Electrochemical Performance of Cation and Anion in EMI-BF$_4$ at 0.2 A g^{-1}

Electrode Materials	Specific Capacitance of EMI$^+$/ F g^{-1}	Specific Capacitance of BF$_4^-$/ F g^{-1}
RGO	153	130
RMGO-12	139	122
RMGO-10	191	139
RMGO-8	234	194
RMGO-6	228	180
RMGO-4	233	170

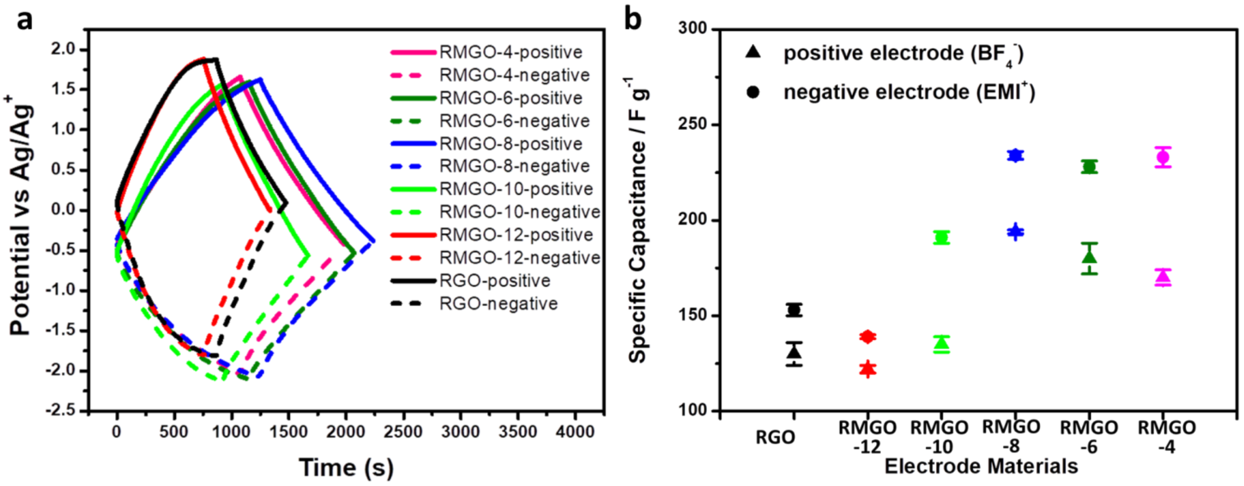

Fig.4. (a) Charging-discharging curves of materials at 0.2 A g^{-1} in EMI-BF$_4$ and (b) specific capacitance of cation and anion in different materials. The solid lines indicate processes on the positive electrode while the dashed lines indicated processes on negative electrodes. The triangle indicates specific capacitance of BF$_4^-$ while the circle indicates specific capacitance of EMI$^+$. The error bar is the standard deviation.

Similarly, the pores are still classified by times of size of cation or anion. For analysis of EMI$^+$, the pores are classified in three types: 0.38 nm < *r* < 0.76 nm, 0.76 nm < *r* < 1.14 nm, and *r* > 1.14 nm. Considering the smaller C_{anion} which may result from larger *d*, we suppose that ion-pairs or ion-cluster are more likely to be formed among anions. Therefore, the pores are classified in three types based on twice size of BF$_4^-$: 0.48 nm < *r* < 0.96 nm, 0.96 nm < *r* < 1.44 nm, and *r* > 1.44 nm when we analyze C^-. As a result, a modified model considering the different ionic behaviors in different pores has been proposed as follows:

$$C_{cation}=C_{(0.38nm<r<0.76nm)}\ A_{(0.38nm<r<0.76nm)}\ +\ C_{(0.76nm<r<1.14nm)}\ A_{(0.76nm<r<1.14nm)}\ +\ C_{(r>1.14nm)}\ A_{(r>1.14nm)} \quad (4a)$$

$$C_{anion}=C_{(0.48nm<r<0.96nm)}\ A_{(0.48nm<r<0.96nm)}\ +\ C_{(0.96nm<r<1.44nm)}\ A_{(0.96nm<r<0.1.44nm)}+\ C_{(r>1.44nm)}\ A_{(r>1.44nm)} \quad (4b)$$

in which $A_{(range\ of\ r)}$ are the specific surface area of different types of pores described above, $C_{(range\ of\ r)}$ are capacitance per unit surface area of the corresponding type of pores. The specific surface areas of different pores are shown in Table 4 and Table 5, which are calculated from the pore distribution shown in Fig. 6 (Chapter 3).

Table 4. Specific Surface Area of Different Pores for Analysis of C_{cation}

Electrode Material	$A_{(r < 0.38\text{ nm})}$ / m^2 g^{-1}	$A_{(0.38\text{nm} < r < 0.76\text{ nm})}$ / m^2 g^{-1}	$A_{(0.76\text{nm} < r < 1.14\text{ nm})}$ / m^2 g^{-1}	$A_{(r > 1.14\text{ nm})}$ / m^2 g^{-1}
RGO	60	14	16	203
RMGO-12	118	41	34	134
RMGO-10	240	94	50	156
RMGO-8	207	77	62	334
RMGO-6	351	146	61	184
RMGO-4	188	56	56	242

Table 5. Specific Surface Area of Different Pores for Analysis of C_{anion}

Electrode Material	$A_{(0.48\text{nm} < r < 0.96\text{ nm})}$ / m^2 g^{-1}	$A_{(0.96\text{nm} < r < 0.1.44\text{ nm})}$ / m^2 g^{-1}	$A_{(r > 1.44\text{ nm})}$ / m^2 g^{-1}
RGO	30	32	171
RMGO-12	63	44	98
RMGO-10	125	62	104
RMGO-8	121	88	257
RMGO-6	196	76	119
RMGO-4	95	76	179

Fig.5 shows the fitting results for EMI$^+$. According to the fitting equation, $C_{(0.38\text{ nm} < r < 0.76\text{ nm})}$, $C_{(0.76\text{ nm} < r < 01.14\text{ nm})}$, and $C_{(r > 1.14\text{ nm})}$ are 0.447, 1.221 and 0.488 F m^{-2}, respectively (Table 6). The largest capacitance per unit surface area is achieved in pores (0.76 nm < r < 1.14 nm). It is important to note that the crest value of capacitance per unit area doesn't come from the largest type of pores. This phenomenon cannot be explained only by the accessibility of pores. According to some reported simulations, the ion packing configuration also has influence on the contribution to capacitance. The ion packing configurations could be different due the different pore sizes [19, 30-32]. The coulombic repulsion between ions with the same charge makes ions away from each other. However, ions are also constrained by pore walls and the electric force. Therefore, the ions would prefer different packing configurations due to the combined action of the three kinds of forces.

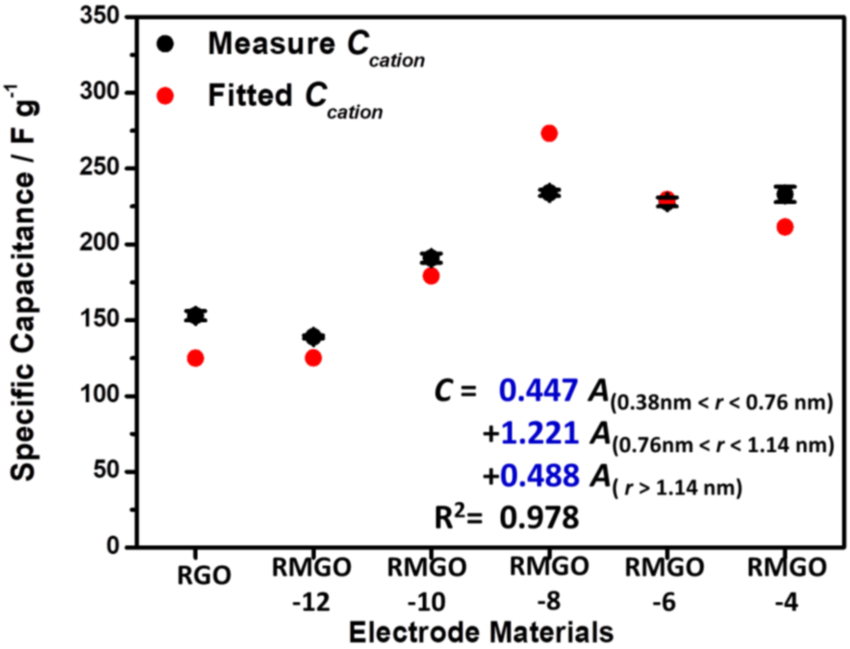

Fig.5 Measured specific capacitance (black) and fitted specific capacitance (red) of EMI$^+$ by multi-linear fitting method. The coefficient of determination (R^2) is 0.978. The error bar is the deviation.

Table 6 Fitted Specific Capacitance of EMI$^+$

Electrode Materials	Fitted Specific Capacitance / F g^{-1}	Deviation from Measure Value / F g^{-1}
RGO	125	25
RMGO-12	125	15
RMGO-10	179	9
RMGO-8	273	38
RMGO-6	229	2
RMGO-4	212	16

To explain the effect of ion configuration on capacitance in our study, a schematic is given in Fig 6. For pores (0.38 nm < r < 0.76 nm), ions can access the pores but the narrow space leads to stronger coulombic repulsion. Therefore, the distance between ions can’t be very close and some regions of surface area are wasted, resulting in smaller capacitance. When the pores are in the range of two to three times of size of EMI$^+$, namely (0.76 nm < r < 1.14 nm), the ions packing changed to the two abreast type since the pores are larger than twice size and electric force aligns the ions along the pore walls. This packing configuration realizes the high density of charge and the full utilization of surface area in pores. Hence this type of pores has the largest capacitance per unit area. For the pores larger than 1.14 nm, the ion packing tends to be loose again since the constraint of pore walls becomes weaken. At the same time, some anions are likely to enter into the space between cations (the purple ones shown in Fig 6). As a result, the density of effective cations decreases and leads to less contribution to capacitance per unit area according to Eqn 3.

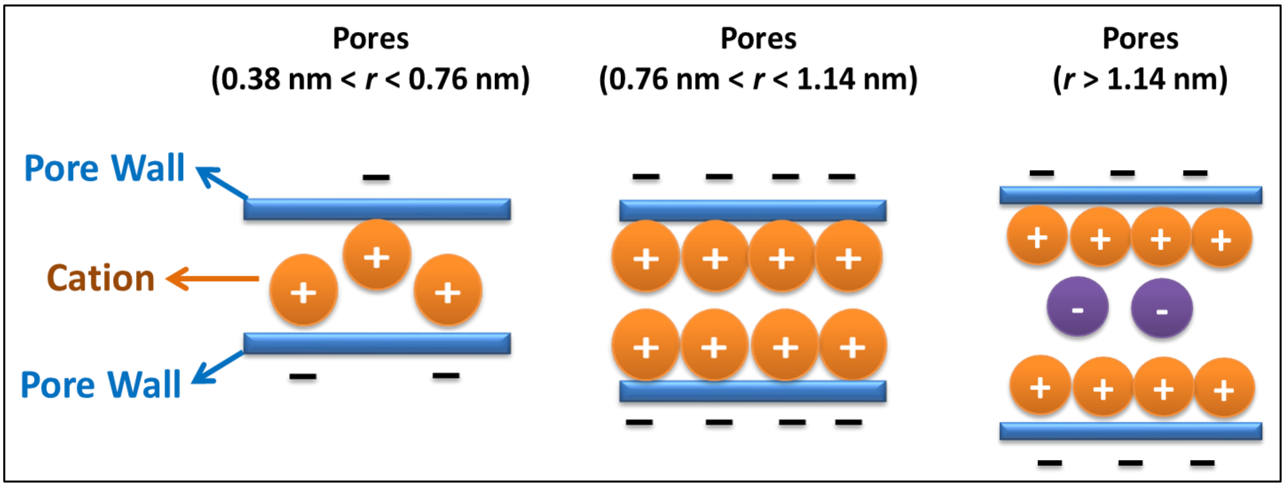

Fig. 6 Schematic explaining effects of ion configuration on capacitance in different pores.

Then we come to the fitting results for BF_4^-. As shown in Fig 7 and Table 7, the variation trend of capacitance per unit area in different pores is similar to that of EMI^+. The result indicates that the model we build can be applied in both cation and anion in ionic liquids. Besides, the capacitance per unit area is smaller that of EMI^+ in all kinds of pores. It is also corresponding to our assumption that the anionic behaviors in the form of ion-pair or ion-cluster. Considering the size of pores with the largest capacitance per unit area, we suppose that anions is more likely to move as ion-pairs instead of ion clusters since the size of two BF_4^- with one EMI^+ is 0.86 nm.

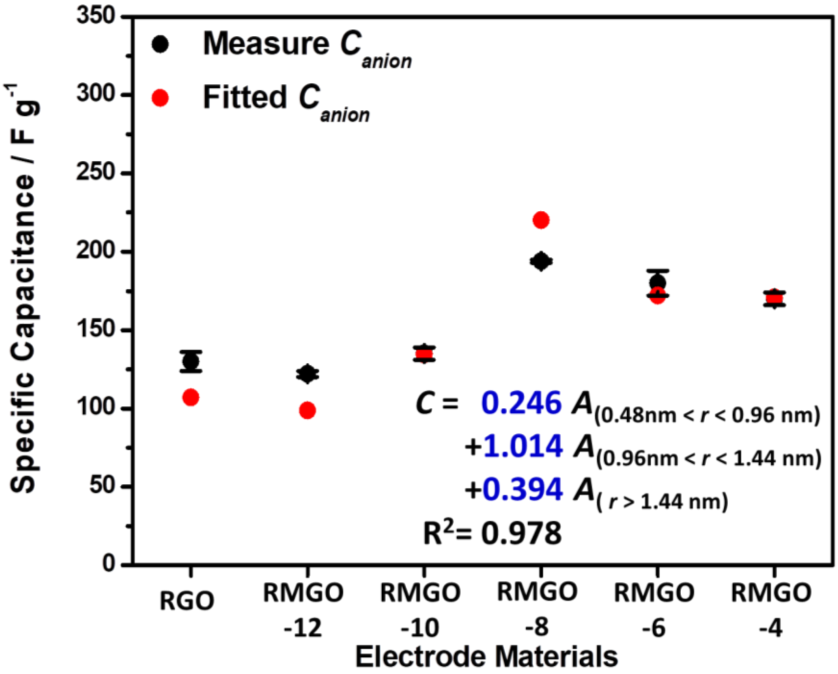

Fig.7 Measured specific capacitance (black) and fitted specific capacitance (red) of BF_4^- by multi-linear fitting method. The coefficient of determination (R^2) is 0.978.

Table 7 Fitted Specific Capacitance of BF_4^-

Electrode Materials	Fitted Specific Capacitance / F g^{-1}	Deviation from Measure Value / F g^{-1}
RGO	107	17
RMGO-12	99	25
RMGO-10	135	5
RMGO-8	220	25
RMGO-6	172	0
RMGO-4	171	3

It should be mentioned that certain deviation still exists between fitted capacitance and measure value. We suggest that it were due to the existence of ink-bottle pores [22, 23]. The "neck" of the ink-bottle pore is exposed to electrolyte while the other end of the pore is closed [24]. If the width of "necks" is smaller than the electrolyte ions, the ink-bottle pores are difficult to be accessed even though the "bottles" are larger than the electrolyte ions (Fig. 8). Considering the larger surface area of pores ($r < 0.38$ nm) in RMGO composites (Table 4), some of these pores may have narrow "necks" and make the larger pores inaccessible to electrolyte.

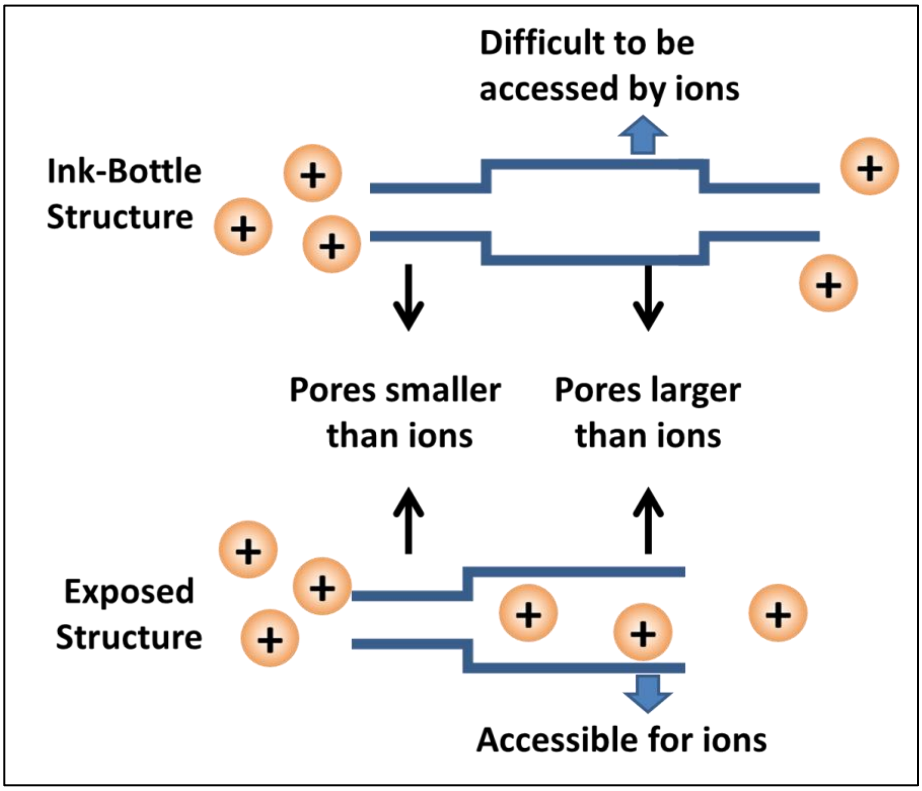

Fig.8. Schematic of ink-bottle structure and exposed structure of pores. Pores larger than ions would become difficult to be accessed by ions since the smaller "necks" hinder ions.

4.4. Conclusions

In summary, we have discussed the ionic behaviors in pores with different sizes by two kind of fitting method. According to the linear fitting between $C/A_{(0.38\ \mathrm{nm} < r < 0.76\ \mathrm{nm})}$ and $A_{(r > 0.76\ \mathrm{nm})} / A_{(0.38\ \mathrm{nm} < r < 0.76\ \mathrm{nm})}$, pores with r larger than 0.76 nm, namely twice of the size of EMI^+ ions, contributed more to the specific capacitance than pores with other sizes. A model has been proposed that the pores with r in the range of 0.38 nm to 0.76 nm result stronger ion-ion correlations due to the shorter distance between the electrolyte ions. The stronger ion-ion correlations would reduce the contributions to capacitance and make the capacitance more dependent on the current density. Then we have analyzed the behavior of cation and anion separately by the multi-linear fitting method. Firstly, anions prefer to move in the form of ion-pairs while cations move as the isolated ions. Secondly, for both cations and anion-pairs, pores with radii in the range of two to three times of cation and anion-pairs are the most efficient pores. It is due to the changed ion packing configuration in different pores. In addition, pores smaller than the ion sizes could hinder the utilization of larger pores when the ink-bottle structure is present.

References

[1] R. Hayes, G. G. Warr, and R. Atkin, “Structure and Nanostructure in Ionic Liquids,” *Chemical Reviews*, vol. 115, no. 13. pp. 6357–6426, 2015.

[2] W. S. Hummers and R. E. Offeman, “Preparation of Graphitic Oxide,” *J. Am. Chem. Soc.*, vol. 80, no. 6, pp. 1339–1339, 1958.

[3] J. Song, X. Wang, and C.-T. Chang, “Preparation and characterization of graphene oxide paper,” *J. Nanomater.*, vol. 448, no. 7152, pp. 457–60, 2007.

[4] J. Chmiola, C. Largeot, P. L. Taberna, P. Simon, and Y. Gogotsi, “Desolvation of ions in subnanometer pores and its effect on capacitance and double-layer theory,” *Angew. Chemie - Int. Ed.*, vol. 47, no. 18, pp. 3392–3395, 2008.

[5] J. Huang, B. G. Sumpter, and V. Meunier, “A universal model for nanoporous carbon supercapacitors applicable to diverse pore regimes, carbon materials, and electrolytes,” *Chem. - A Eur. J.*, vol. 14, no. 22, pp. 6614–6626, 2008.

[6] N. Jackel, M. Rodner, A. Schreiber, J. Jeongwook, M. Zeiger, M. Aslan, D. Weingarth, and V. Presser, “Anomalous or regular capacitance? The influence of pore size dispersity on double-layer formation,” *J. Power Sources*, vol. 326, pp. 660–671, 2016.

[7] J. Chmiola, C. Largeot, P. L. Taberna, P. Simon, and Y. Gogotsi, “Desolvation of ions in subnanometer pores and its effect on capacitance and double-layer theory,” *Angew. Chemie - Int. Ed.*, vol. 47, no. 18, pp. 3392–3395, 2008.

[8] C. Largeot, C. Portet, J. Chmiola, P. L. Taberna, Y. Gogotsi, and P. Simon, “Relation between the ion size and pore size for an electric double-layer capacitor,” *J. Am. Chem. Soc.*, vol. 130, no. 9, pp. 2730–2731, 2008.

[9] Z.-X. Luo, Y.-Z. Xing, Y.-C. Ling, A. Kleinhammes, and Y. Wu, “Electroneutrality breakdown and specific ion effects in nanoconfined aqueous electrolytes observed by NMR.” *Nat. Comm.*, vol. 6, p. DOI:10.1038/ncomms7358, 2015.

[10] W.-Y. Tsai, P.-L. Taberna, and P. Simon, “Electrochemical Quartz Crystal Microbalance (EQCM) Study of Ion Dynamics in Nanoporous Carbons,” *J. Am. Chem. Soc.*, vol. 136, no. 24, pp. 8722–8728, 2014.

[11] C. Merlet *et al.*, “On the molecular origin of supercapacitance in nanoporous carbon electrodes,” *Nat. Mater.*, vol. 11, no. 4, pp. 306–310, 2012.

[12] J. Huang, B. G. Sumpter, and V. Meunier, “A universal model for nanoporous carbon supercapacitors applicable to diverse pore regimes, carbon materials, and electrolytes,” *Chem. - A Eur. J.*, vol. 14, no. 22, pp. 6614–6626, 2008.

[13] N. Jackel, M. Rodner, A. Schreiber, J. Jeongwook, M. Zeiger, M. Aslan, D. Weingarth, and V. Presser, “Anomalous or regular capacitance? The influence of pore size dispersity on double-layer formation,” *J. Power Sources*, vol. 326, pp. 660–671, 2016.

[14] W. Hsieh, T.-L. A. Horng, H.-C. Huang, and H. Teng, “Facile simulation of carbon with wide pore size distribution for electric double-layer capacitance based on Helmholtz models,” *J. Mater. Chem. A*, vol. 3, no. 32, pp. 16535–16543, 2015.

[15] G. Gryglewicz, J. Machnikowski, E. Lorenc-Grabowska, G. Lota, and E. Frackowiak, “Effect of pore size distribution of coal-based activated carbons on double layer capacitance,” *Electrochim. Acta*, vol. 50, no. 5, pp. 1197–1206, 2005.

[16] J. Chmiola, G. Yushin, R. Dash, and Y. Gogotsi, “Effect of pore size and surface area of carbide derived carbons on specific capacitance,” *J. Power Sources*, vol. 158, no. 1, pp. 765–772, 2006.

[17] C. Largeot, C. Portet, J. Chmiola, P. L. Taberna, Y. Gogotsi, and P. Simon, “Relation between the ion size and pore size for an electric double-layer capacitor,” *J. Am. Chem. Soc.*, vol. 130, no. 9, pp. 2730–2731, 2008.

[18] J. Vatamanu, M. Vatamanu, and D. Bedrov, “Non-Faradaic Energy Storage by Room Temperature Ionic Liquids in Nanoporous Electrodes,” *ACS Nano*, vol. 9, no. 6, pp. 5999–6017, 2015.

[19] X. Wang, H. Zhou, E. Sheridan, J. C. Walmsley, D. Ren, and D. Chen, “Geometrically confined favourable ion packing for high gravimetric capacitance in carbon–ionic liquid supercapacitors,” *Energy Environ. Sci*, vol. 232, no. 9, pp. 232–239, 2016.

[20] K. N. Kudin, B. Ozbas, H. C. Schniepp, R. K. Prudhomme, I. A. Aksay, and R. Car, “Raman spectra of graphite oxide and functionalized graphene sheets,” *Nano Lett.*, vol. 8, no. 1, pp. 36–41, 2008.

[21] P. Azaïs, L. Duclaux, P. Florian, D. Massiot, M.-A. Lillo-Rodenas, A. Linares-Solano, J.-P. Peres, C. Jehoulet, and F. Beguin, “Causes of supercapacitors aging in organic electrolyte,” *J. Power Sources*, vol. 171, no. 2, pp. 1046–1053, 2007.

[22] P. I. Ravikovitch and A. V. Neimark, “Experimental confirmation of different mechanisms of evaporation from ink-bottle type pores: Equilibrium, pore blocking, and cavitation,” *Langmuir*, vol. 18, no. 25, pp. 9830–9837, 2002.

[23] C. Fan, D. D. Do, and D. Nicholson, “On the cavitation and pore blocking in slit-shaped ink-bottle

pores," *Langmuir*, vol. 27, no. 7, pp. 3511–3526, 2011.

[24] P. T. M. Nguyen, C. Fan, D. D. Do, and D. Nicholson, "On the cavitation-like pore blocking in ink-bottle pore: Evolution of hysteresis loop with neck size," *J. Phys. Chem. C*, vol. 117, no. 10, pp. 5475–5484, 2013.

[25] W. Hsieh, T.-L. A. Horng, H.-C. Huang, and H. Teng, "Facile simulation of carbon with wide pore size distribution for electric double-layer capacitance based on Helmholtz models," *J. Mater. Chem. A*, vol. 3, no. 32, pp. 16535–16543, 2015.

[26] B. Schwenzer, S. N. Kerisit, and M. Vijayakumar, "Anion pairs in room temperature ionic liquids predicted by molecular dynamics simulation, verified by spectroscopic characterization," *RSC Adv.*, vol. 4, no. 11, pp. 5457–5464, 2014.

[27] K. Fumino, V. Fossog, P. Stange, D. Paschek, R. Hempelmann, and R. Ludwig, "Controlling the subtle energy balance in protic ionic liquids: Dispersion forces compete with hydrogen bonds," *Angew. Chemie - Int. Ed.*, vol. 54, no. 9, pp. 2792–2795, 2015.

[28] K. Fumino, A. M. Bonsa, B. Golub, D. Paschek, and R. Ludwig, "Non-ideal mixing behaviour of hydrogen bonding in mixtures of protic ionic liquids," *Chem. Phys. Chem.*, vol. 16, no. 2, pp. 299–304, 2015.

[29] I. V. Voroshylova, F. Teixeira, R. Costa, C. M. Pereira, and M. N. D. S. Cordeiro, "Interactions in the ionic liquid [EMIM][FAP]: a coupled experimental and computational analysis," *Phys. Chem. Chem. Phys.*, vol. 18, no. 4, pp. 2617–2628, 2016.

[30] C. Merlet, B. Rotenberg, P. A. Madden, P.-L. Taberna, P. Simon, Y. Gogotsi, and M. Salanne, "On the molecular origin of supercapacitance in nanoporous carbon electrodes," *Nat. Mater.*, vol. 11, no. 4, pp. 306–310, 2012.

[31] M. Z. Bazant, B. D. Storey, and A. A. Kornyshev, "Double layer in ionic liquids: Overscreening versus crowding," *Phys. Rev. Lett.*, vol. 106, no. 4, pp. 6–9, 2011.

[32] Y. Shim and H. J. Kim, "Nanoporous carbon supercapacitors in an ionic liquid: A computer simulation study," *ACS Nano*, vol. 4, no. 4, pp. 2345–2355, 2010.

Chapter 5

Ionic behaviors in Different Pores at Different Voltage and Their Different Contributions to Specific Capacitance

5.1. Introduction

To enhance the energy density of supercapacitors, two apparent strategies have been explored intensively according to Eqn 1: $E = CU^2/8$ that governs the energy density E with C being the specific capacitance of single electrode materials, and U being the working voltage across the positive and negative electrode.

One strategy is to increase the specific capacitance (C). Recently, graphene has been recognized as an attractive material to provide large specific capacitance due to its excellent conductivity and large specific surface area [1]. In our continuing study on graphene supercapacitors, great efforts have been invested to develop the CNT and graphene (CNT/graphene) composites for supercapacitor applications [2-5]. The specific capacitance has been enlarged since the specific surface area has been increased by using CNT to prevent re-stacking between graphene layers. The resulting electrode materials are porous CNT/graphene materials we synthesized in Chapter 3.

Another approach to enlarge the energy density E is to increase the working voltage (U). Using an electrolyte with a wider electrochemical stability window is a direct way to reach a larger U. Ionic liquid has been investigated as a new-type electrolyte since its electrochemical window is usually much wider than both aqueous electrolyte and the commonly used organic electrolytes [6]. In this study, we has preferred a kind of ionic liquid, 1-methyl-1-propylpiperidinium bis (trifluoromethyl sulfonyl) imide (MPPp-TFSI), since its electrochemical stability window is larger than the ionic liquids, 1-ethyl-3-methylimidazolium tetrafluoroborate (EMI-BF_4), we used in Chapter 3 and Chapter 4. Considering some reported discussions [7-9], ionic behaviors in pores would be different when voltage increases. Therefore, we have taken multiple-linear fittings between specific surface area of different pores and specific capacitance of when supercapacitors are charged to 4.0V and 4.5V respectively. The fitting results could help us figure out the behaviors of cation and anion of MPPp-TFSI in our porous CNT/graphene at different voltage. A hypothesis has been made that more ions are likely to be squeezed into accessible pores by increased voltage. In addition, some smaller pores could be expanded by ions at high voltage (4.5 V), which lead to the increase of specific capacitance.

5.2. Experimental

The electrode materials are synthesized by co-reduction of oxidized multi-wall carbon nanotubes (MWNTs) and graphene oxide (GO). The resulting CNT/graphene composites are designated as RMGO. Details of the synthesis have been described in Chapter 3.The ionic liquid electrolytes, 1-ethyl-3-methylimidazolium tetrafluoroborate (EMI-BF_4) and 1-methyl-1-propylpiperidinium bis (trifluoromethyl sulfonyl) imide (MPPp-TFSI), were purchased commercially from Toyo-Gosei. The purity of ionic liquids is 99.9%.

The electrochemical stability windows of EMI-BF_4 and MPPp-TFSI are measured in a three-electrode system with Pt as both working electrode and counter electrode, and silver-silver ion (Ag/Ag^+) as reference electrode. The potential limitations of electrode materials in MPPp-TFSI is measured in a three electrode system a three-electrode system with RMGO composites as working electrode, Pt as counter electrode, and Ag/Ag^+ as reference electrode. The electrochemical stability window is characterized by the linear scan voltammetry at 5 mV s^{-1} from the open-circuit potential to positive and negative potential, respectively. The potential limitations of RMGO composites are measured by charging process with the constant current density, 0.2 A g^{-1}.

In order to figure out the specific capacitance on both positive and negative electrodes at the same time, the charging-discharging process was performed using a three-electrode system with Ag/Ag+ as the reference electrode and RMGO composite as both the positive and negative electrode. The voltage between two electrodes is from 0 to 4.0V and 4.5V, respectively. The current density of charging-discharging process is 1.0 A g^{-1}.

5.3. Results and Discussions

5.3.1. Electrochemical Stability Window of Electrolytes and Electrochemical Window of Electrode Materials in MPPp-TFSI

According to the results of linear scan voltammetry (Fig 1), it is obvious that the stability window of MPPp-TFSI (5.8V) is much larger that of EMI-BF_4 (4.6) V as shown in Table 1. The potentials corresponding to inflection points are the decomposition potentials of ions in electrolytes.

Table 1. Electrochemical Stability Windows of Electrolytes

Electrolytes	Electrochemical Window
EMI-BF_4	-2.8V ~ 1.8 V (Δ=4.6 V)
MPPp-TFSI	-3.4 V ~ 2.4 V (Δ=5.8 V)

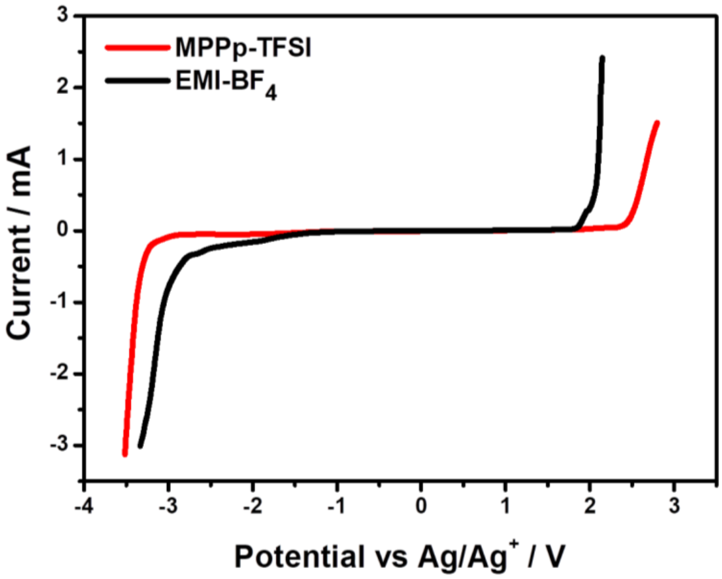

Fig.1 Electrochemical stability windows of EMI-BF4 (black) and MPPp-TFSI (red). The MPPp-TFSI has the larger stability window.

However, the electrochemical window of electrode materials in MPPp-TFSI, namely the difference between positive and negative potential limitation (2.23 V and – 2.67V), is only 4.9V, which is much smaller than the stability window of the electrolyte. Considering a reported work of our group, is attributed to the reactions between MPPp-TFSI and the oxygen-containing groups in the SWNT/graphene electrodes [10]. The charging-discharging curves used to characterize the potential limitation of RMGO-4 are shown in Fig.2.

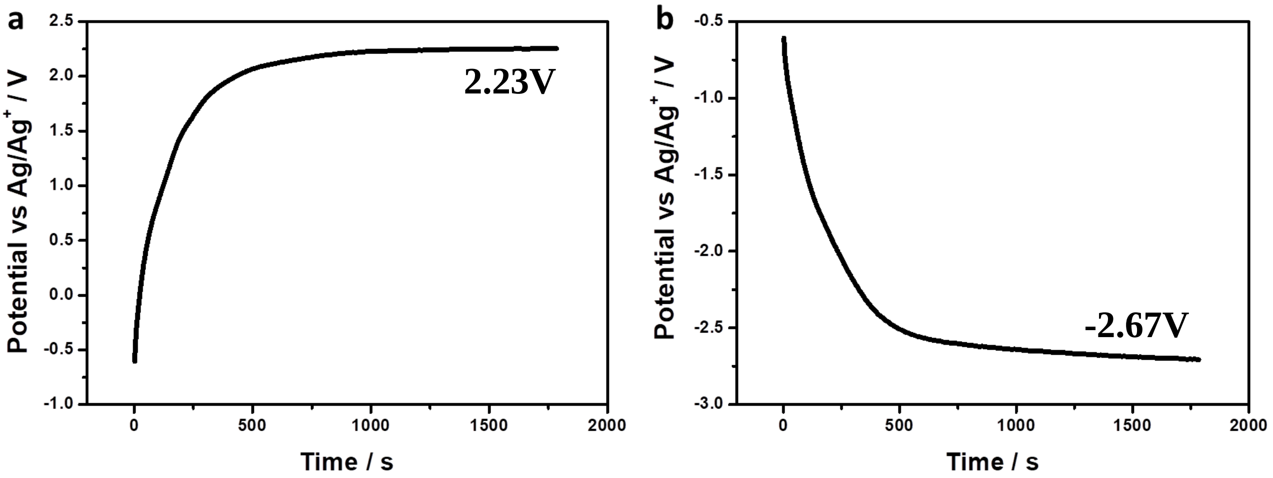

Fig 2. (a) Positive and (b) negative potential limitations of RMGO-4 in MPPp-TFSI.

5.3.2 Performance of Electrode Materials in MPPp-TFSI at Different Voltage

The energy density of supercapacitors based on RMGO composites in MPPp-TFSI shown in Table 2 are calculated from the charging-discharging curves in Fig.3. The current density is 1.0 A g^{-1} and the applied voltage is 4.0 V and 4.5 V. The highest energy density, 73 Wh kg^{-1}, is achieved in RMGO-8 at 4.5V. We also have characterized the performance of positive and negative electrode, separately in a three-electrode system. The charging-discharging curves are shown in Fig 4 and Fig 5. Since the positive electrode approximates to its potential limitation when the applied voltage is 4.5 V (Fig.5), supercapacitors based on RMGO composite can't be further charged to higher voltage even though their electrochemical window is 4.8 V.

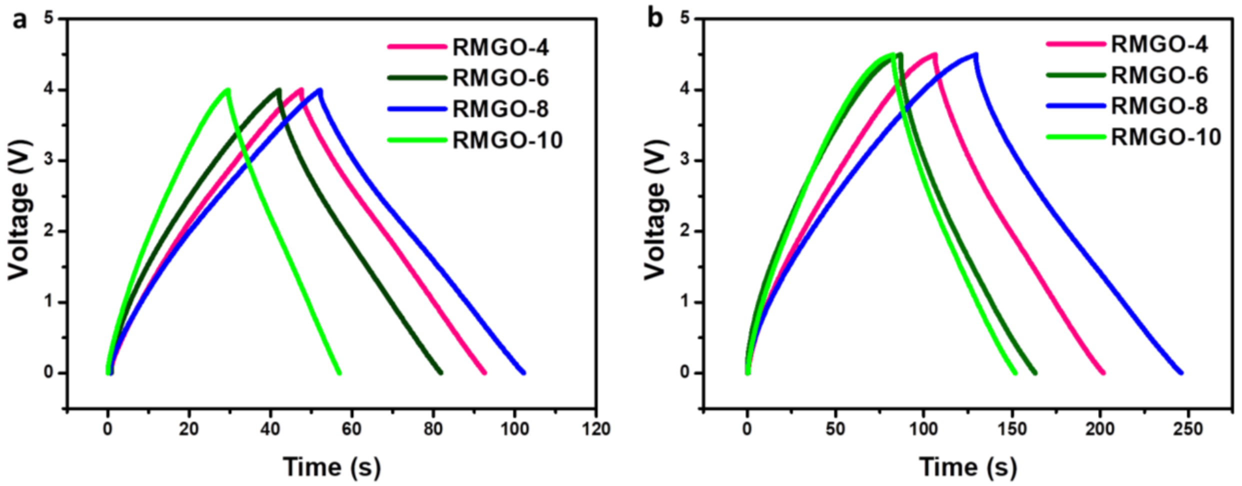

Fig.3 Charging-discharging curves in MPPp-TFSI at (a) 4.0 V and (b) 4.5 V. The current density is 1.0 A g^{-1}.

Table 2 Energy Density of Supercapacitors at 4.0V and 4.5V

Electrode Materials	Energy Density at 4.0 V /Wh kg^{-1}	Energy Density at 4.5 V /Wh kg^{-1}
RMGO-10	15	43
RMGO-8	29	73
RMGO-6	22	46
RMGO-4	25	60

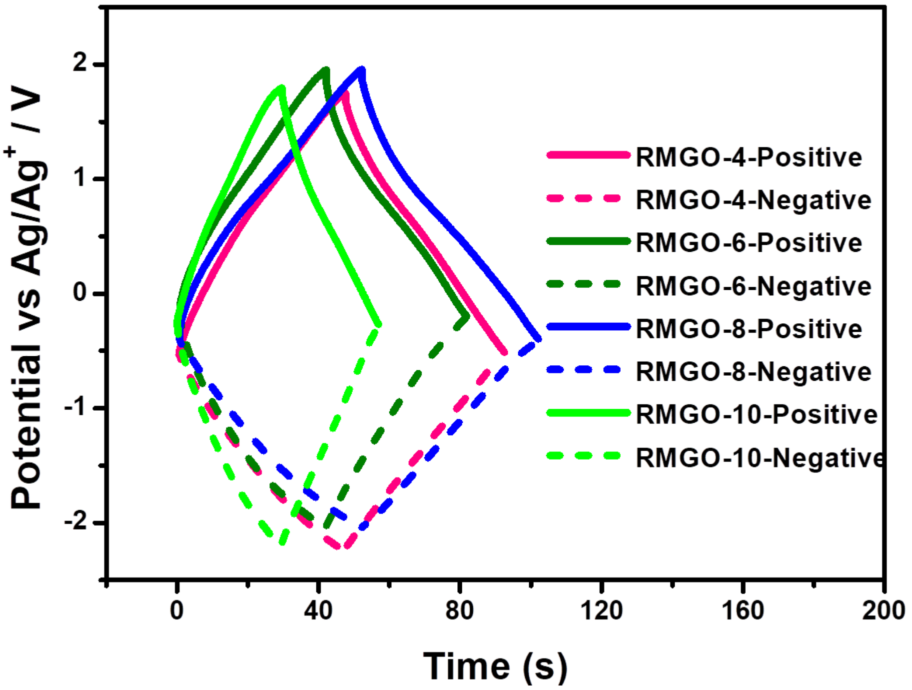

Fig. 4 Charging-discharging curves at 1.0 A g^{-1} in a three-electrode system. The applied voltage is 4.0V.

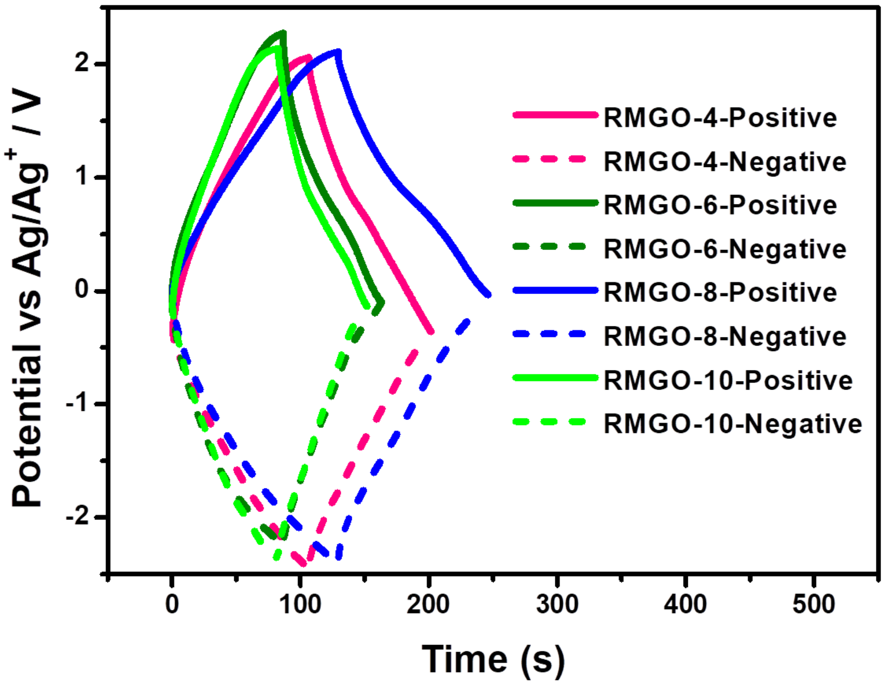

Fig. 5 Charging-discharging curves at 1.0 A g^{-1} in a three-electrode system. The applied voltage is 4.5V.

Table 3 Specific Capacitance of Cation and Anion (Applied Voltage: 4.0V)

Electrode Materials	Specific Capacitance of MPPp$^+$ /F g^{-1}	Specific Capacitance of TFSI$^-$ /F g^{-1}
RMGO-10	28	29
RMGO-8	57	51
RMGO-6	44	39
RMGO-4	55	42

Table 4 Specific Capacitance of Cation and Anion (Applied Voltage: 4.5V)

Electrode Materials	Specific Capacitance of MPPp$^+$ /F g^{-1}	Specific Capacitance of TFSI$^-$ /F g^{-1}
RMGO-10	64	63
RMGO-8	104	116
RMGO-6	73	67
RMGO-4	95	85

It is worth noting that specific capacitance of both cation and anion have increased when applied voltage increase from 4.0 to 4.5 V (Table 3 and Table 4). Since all charging-discharging processes are in the range of electrochemical window, we suppose that the excessive specific capacitance is not from the trigger redox process at higher voltage. Therefore, an assumption has been made that the ionic behaviors could be affected by voltage and the changed behaviors in pores lead to the increase of specific capacitance [7-9].The detailed discussions are shown in the next section.

5.3.3 Behaviors of Cation and Anion in Different Pores at Different Voltage

To clarify the influence of voltage on ionic behaviors, the multi-linear fittings have been taken between specific surface area of different pores and specific capacitance when the applied voltage is 4.0V and 4.5V, separately. Considering the size of $MPPp^+$ (0.34 nm) and $TFSI^-$ (0.32 nm) as well as the higher viscosity of MPPp-TFSI compared with $EMI\text{-}BF_4$ [7-9, 11, 12], the models of cation and anion used for fittings are built as below:

$$C_{cation}=C_{(r<0.68nm)}\ A_{(r<0.68nm)}\ +\ C_{(r>0.68nm)}\ A_{(r>0.68nm)} \tag{2a}$$

$$C_{anion}=C_{(r<0.96nm)}\ A_{(r<0.96nm)}\ +\ C_{(r>0.96nm)}\ A_{(r>0.96nm)} \tag{2b}$$

in which $A_{\ (range\ of\ r)}$ are the specific surface area of different types of pores described above, $C_{\ (range\ of\ r)}$ are capacitance per unit surface area of the corresponding type of pores. The specific surface areas of different pores are shown in Table 5, which are calculated from the pore distribution shown in Fig. 6 (Chapter 3). The threshold size 0.68 nm and 0.96 nm are twice the size of $MPPp^+$ and triple the size of $TFSI^-$, respectively. It should be noted that since all pores in RMGO composites are smaller than 2.5nm, the pores (r > 0.68 nm) and pores (r > 0.96) are pores (0.68nm < r < 2.5nm) and pores (0.96nm < r < 2.5nm), actually.

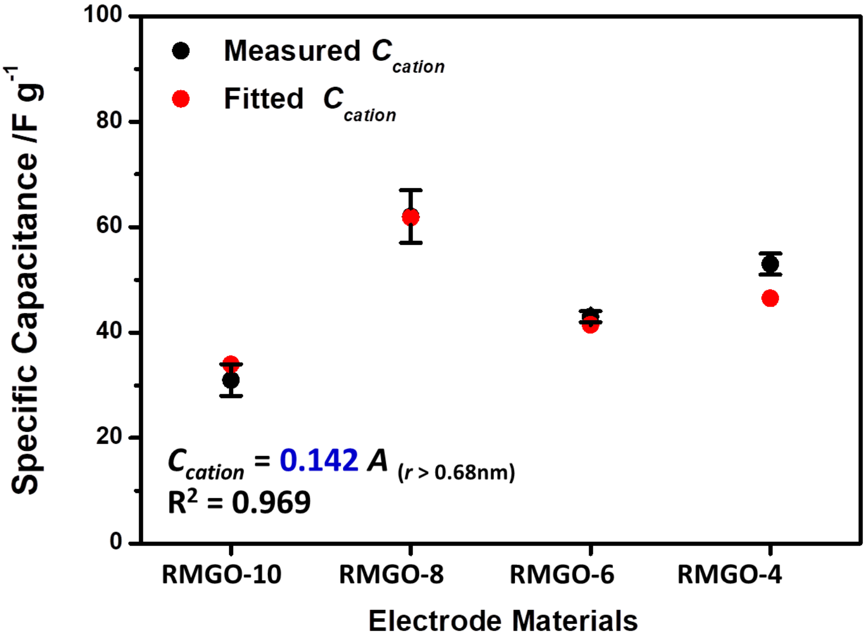

Fig. 6 Measured specific capacitance (black) and fitted specific capacitance (red) of $MPPp^+$ by multi-linear fitting method. The applied voltage is 4.0 V and R^2 is the coefficient of determination. The error bar is the deviation.

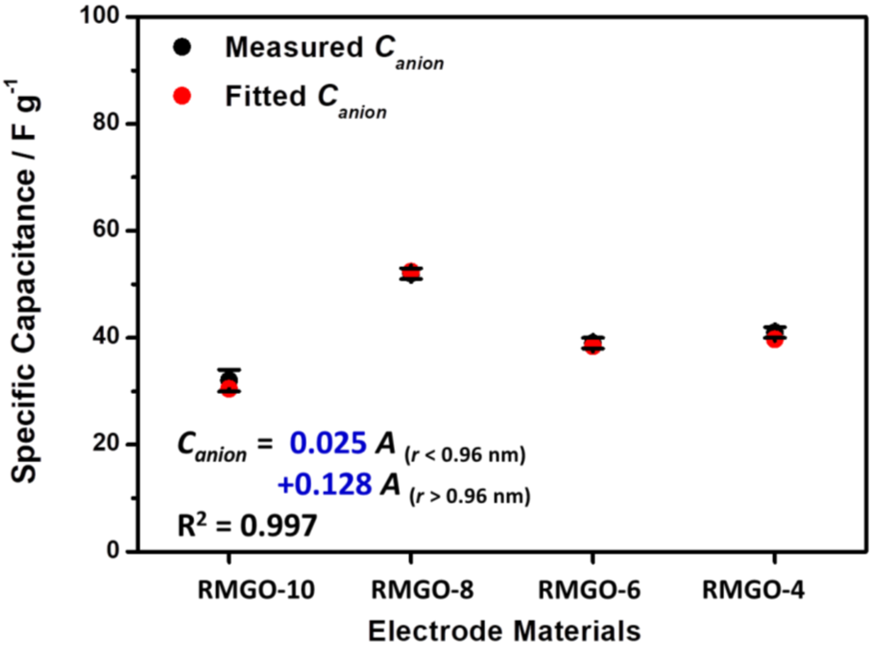

Fig. 7 Measured specific capacitance (black) and fitted specific capacitance (red) of TFSI$^-$ by multi-linear fitting method. The applied voltage is 4.0 V and R^2 is the coefficient of determination. The error bar is the standard deviation.

Table 6 Fitted Specific Capacitance (Applied Voltage: 4.0V)

Electrode Materials	Fitted Specific Capacitance of Cation /F g^{-1}	Fitted Specific Capacitance of Anion /F g^{-1}
RMGO-10	31	32
RMGO-8	62	52
RMGO-6	43	39
RMGO-4	53	41

The fitting results at 4.0 V are shown in Fig.6, Fig.7 and Table 6. For cations, the pores smaller than 0.68 nm have little contributions to specific capacitance. It implies that MPPp$^+$ moves as ion-clusters rather than isolated ions. Then for anions, the capacitance pre unit area in pores pores (0.96nm < r < 2.5nm) is much larger than that in pores (r < 0.96 nm). Similarly, TFSI$^-$ also moves as ion-clusters due to the higher viscosity of MPPp-TFSI.

When the applied voltage increases to 4.5 V, the capacitance per unit of pores (0.68nm < r < 2.5nm) increases from 0.142 to 0.256 F m^{-2} for cations. It is supposed that more ions could be pushed into ions due to higher voltage (Fig 10). Similarly, the capacitance per unit of pores (0.96nm < r < 2.5nm) increases from 0.128 to 0.324 F m^{-2} for anions partially from the same reason. In the contrary, the value of capacitance in pores (r <0.96nm) decreases from 0.025 to 0.012 F m^{-2}. According some reported discussions [8, 11, 12], a possible reason is that some pores slightly smaller than 0.96nm are expanded by ion-clusters forced by higher voltage (Fig 11). This behavior of anion-clusters also leads to the increase of fitted capacitance per unit area in pores larger than 0.96nm. The fitting results at 4.5 V are shown in Fig.8, Fig.9 and Table 7. Combining with the conclusions for ionic behaviors in EMI-BF_4 discussed in Chapter 4, the deviations between fitted and measured values are due to the ink-bottle structures, which hinder the access of ions into larger pores.

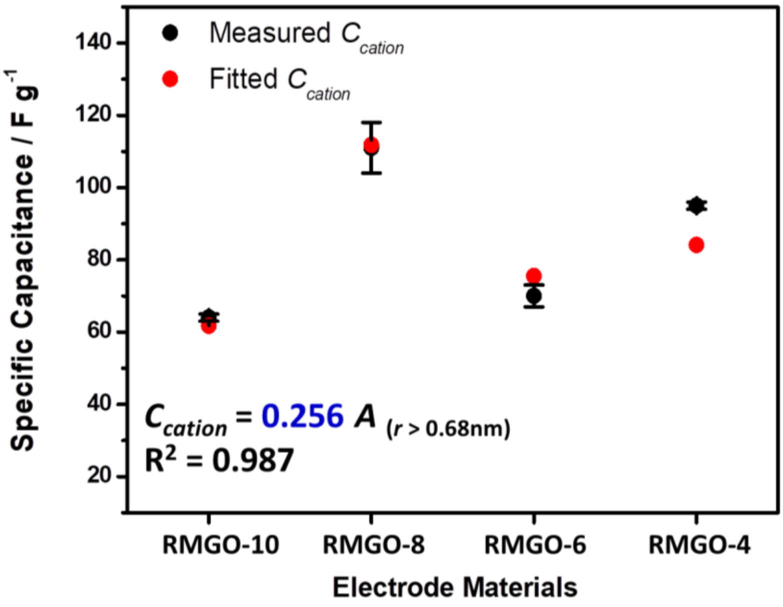

Fig. 8 Measured specific capacitance (black) and fitted specific capacitance (red) of $MPPp^+$ by multi-linear fitting method. The applied voltage is 4.5 V and R^2 is the coefficient of determination. The error bar is the deviation.

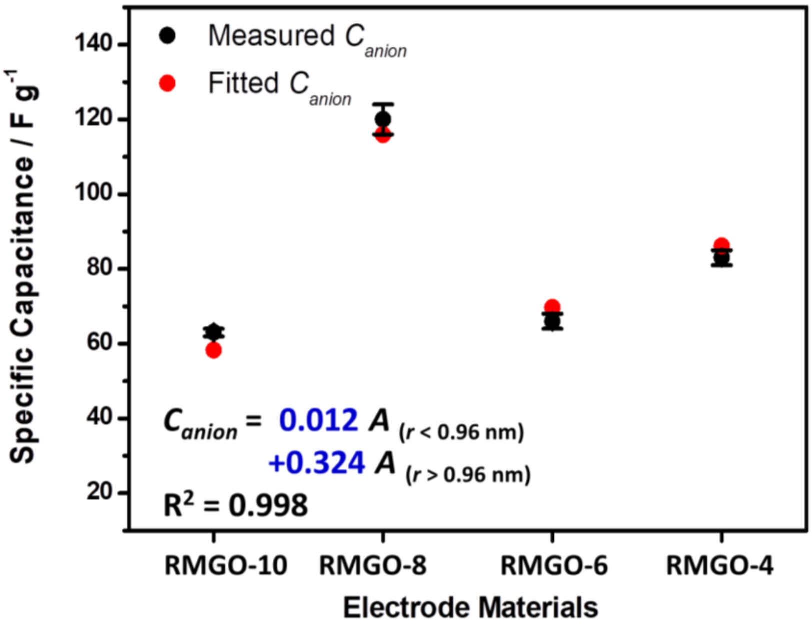

Fig. 9 Measured specific capacitance (black) and fitted specific capacitance (red) of $TFSI^-$ by multi-linear fitting method. The applied voltage is 4.5 V and R^2 is the coefficient of determination. The error bar is the deviation.

Table 7 Fitted Specific Capacitance (Applied Voltage: 4.5V)

Electrode Materials	Fitted Specific Capacitance of Cation /F g^{-1}	Fitted Specific Capacitance of Anion /F g^{-1}
RMGO-10	64	63
RMGO-8	111	120
RMGO-6	70	66
RMGO-4	95	83

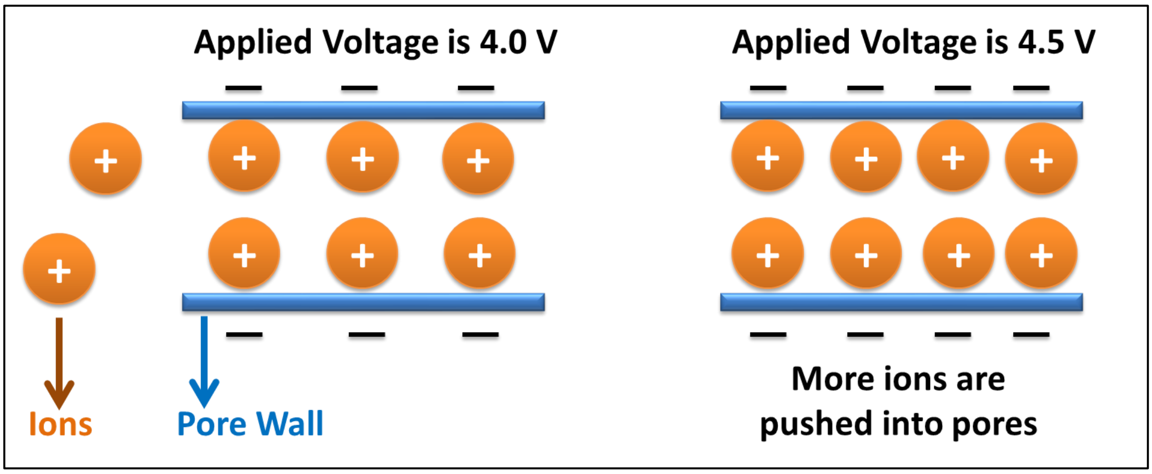

Fig 10 Schematic of increased specific capacitance due to increased amount of ions in pores when applied voltage increases from 4.0 to 4.5 V.

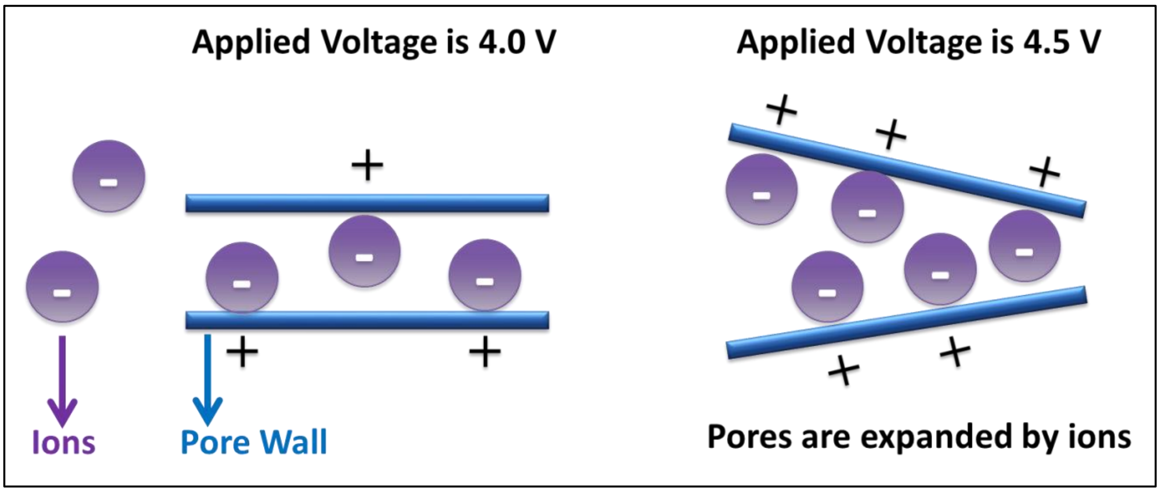

Fig 11 Schematic of increased specific capacitance due to expansion of smaller pores when applied voltage increases from 4.0 V to 4.5 V.

5.4. Conclusions

According to the results of multi-linear fittings, the most efficient pores for cations are pores (0.68nm < r < 2.5nm) while those are pores (0.96nm < r < 2.5nm) for anions. It is due to the existence of ion-clusters in MPPp-TFSI electrolyte due to its high viscosity. In addition, we have also figured out the change of ionic behaviors when applied voltage increases. For both cations and anions, more ions can be pushed into accessible pores by voltage. And for anions, some smaller pores can be expanded by anion-clusters forced by higher voltage. The two behaviors above are the reasons for the larger specific capacitance at the higher applied voltage of supercapacitors.

References

[1] G. Wang, L. Zhang, and J. Zhang, “A review of electrode materials for electrochemical supercapacitors,” *Chem. Soc. Rev.*, vol. 41, no. 2, pp. 797–828, 2012.

[2] Q. Cheng, J. Tang, J. Ma, H. Zhang, N. Shinya, and L.-C. Qin, “Graphene and carbon nanotube composite electrodes for supercapacitors with ultra-high energy density,” *Phys. Chem. Chem. Phys.*, vol. 13, no. 39, pp. 17615–17624, 2011.

[3] Q. Cheng, J. Tang, N. Shinya, and L.-C. Qin, “Polyaniline modified graphene and carbon nanotube composite electrode for asymmetric supercapacitors of high energy density,” *J. Power Sources*, vol. 241, pp. 423–428, 2013.

[4] Q. Shao, J. Tang, Y. Lin, J. Li, F. Qin, J. Yuan, and L.-C. Qin, “Carbon nanotube spaced graphene aerogels with enhanced capacitance in aqueous and ionic liquid electrolytes”, *J. Power Sources*, vol. 278, pp. 751–759, 2015.

[5] F. Zhang, J. Tang, N. Shinya, and L. C. Qin, “Hybrid graphene electrodes for supercapacitors of high energy density”, *Chem. Phys. Lett.*, vol. 584, pp. 124–129, 2013.

[6] F. Béguin, V. Presser, A. Balducci, and E. Frackowiak, *Adv. Mater.*, 2014, 26, 2219-2251.

[7] J. Vatamanu, M. Vatamanu, and D. Bedrov, “Non-Faradaic Energy Storage by Room Temperature Ionic Liquids in Nanoporous Electrodes,” *ACS Nano*, vol. 9, no. 6, pp. 5999–6017, 2015.

[8] C. M. Yang, H. J. Jung, and Y. J. Kim, “Anomalous cyclic voltammetric response from pores smaller than ion size by voltage-induced force,” *J. Colloid Interface Sci.*, vol. 446, pp. 208–212, 2015.

[9] N. Jackel, B. Krüner, K. L. V. Aken, M. Alhabeb, B. Anasori, F. Kaasik, Y. Gogotsi, and V. Presser, “Electrochemical in Situ Tracking of Volumetric Changes in Two-Dimensional Metal Carbides (MXenes) in Ionic Liquids,” *ACS Appl. Mater. Interfaces*, vol. 8, no. 47, pp. 32089–32093, 2016.

[10] J. Li, J. Tang, J. Yuan, K. Zhang, Q. Shao, Y. Sun, and L.-C. Qin, “Interactions between Graphene and Ionic Liquid Electrolyte in Supercapacitors,” *Electrochim. Acta*, vol. 197, pp. 84–91, 2016.

[11] Y. Yang, F. Lu, Z. Zhou, W. Song, Q. Chen, and X. Ji, “Electrochemically cathodic exfoliation of graphene sheets in room temperature ionic liquids N-butyl, methylpyrrolidinium bis(trifluoromethylsulfonyl)imide and their electrochemical properties,” *Electrochim. Acta*, vol. 113, pp. 9–16, 2013.

[12] P. W. Ruch, M. Hahn, F. Rosciano, M. Holzapfel, H. Kaisera, W. Scheifele, B. Schmitt, P. Novák, R.

Kötz, and A. Wokaun, “In situ X-ray diffraction of the intercalation of (C2H5)4N+ and BF4- into graphite from acetonitrile and propylene carbonate based supercapacitor electrolytes,” *Electrochim. Acta*, vol. 53, no. 3, pp. 1074–1082, 2007.

Chapter 6

Enhancement of Energy Density of CNT/Graphene Supercapacitors by Improved Pore Structure and Asymmetric Configuration

6.1. Introduction

To enhance the energy density of supercapacitors, enlarging the working voltage has been considered as an effective way according to Eqn 1: $E = CU^2/8$, in which E is the energy density, C is the specific capacitance of single electrode materials, and U is the working voltage across the positive and negative electrode.

Except for choosing ionic liquid electrolyte with wider electrochemical stability window, asymmetric configurations of a supercapacitor can also raise U by making a full use of the different potential windows of the two electrodes [1]. The term “asymmetric” here means either using two different electrode materials in one device or using the same electrode material in both electrodes with unequal mass [2]. The latter is often considered to be more practical as it can be easily implemented in industrial production [3].

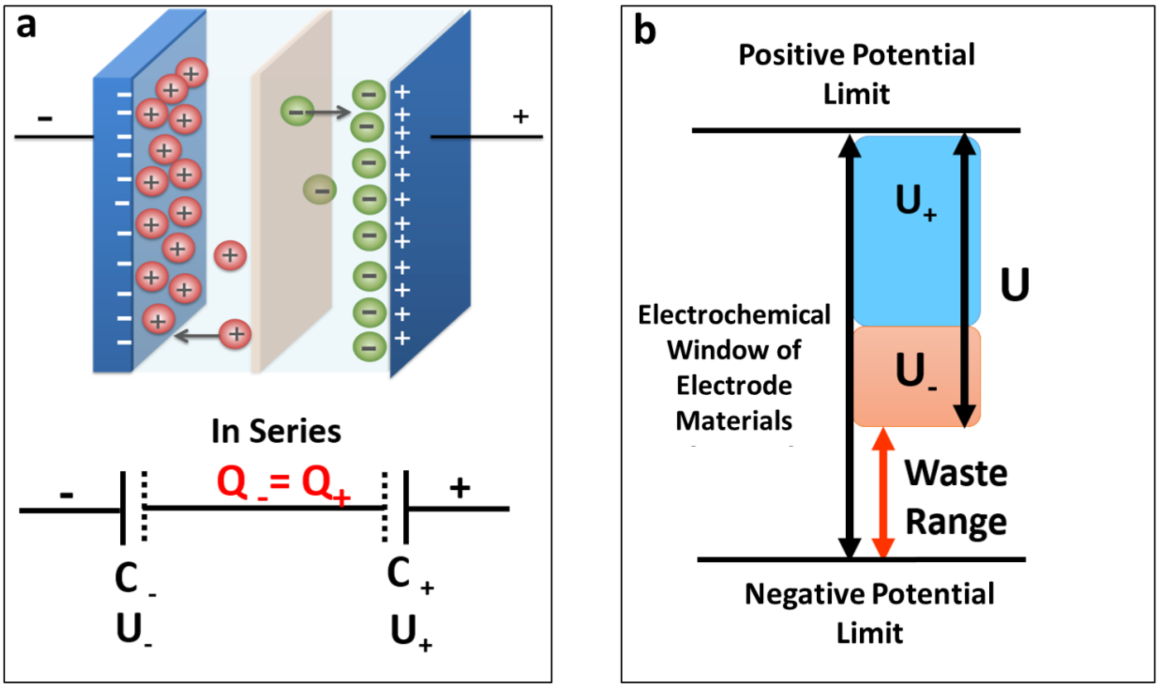

Fig. 1 (a) Schematic of supercapacitor and (b) potential ranges of two electrodes. The two EDLCs on two electrodes are in series so that the electric charge is the same. When one electrode reaches the potential limit before the other does, a potential range will be unutilized so that the actual working voltage (U) is smaller than the electrochemical window of electrode materials.

The mechanism for raising working voltage U using unequal electrode mass is illustrated in Fig. 1 and Eqn. (2-5) below:

$$Q_+ = Q_- \tag{2}$$

$$Q = mCU \tag{3}$$

$$m_+ C_{anion} U_+ = m_- C_{cation} U_- \tag{4}$$

$$\frac{U_+}{U_-} = \frac{m_+ C_{anion}}{m_- C_{cation}} \tag{5}$$

in which Q_+ and Q_- represent the electric charge on the positive and negative electrodes, respectively, U_+ and U_- are potential windows for the two electrodes, respectively, C_{anion} and C_{cation} are the specific capacitance of the two electrodes, respectively, and m_+ and m_- are the mass of the two electrodes, respectively. Since the two single EDLCs on the positive and negative are connected in series in a full supercapacitor device, the electric charge on the two electrodes is the same (Eqn. 2). Then the potential windows for the two electrodes are determined by the specific capacitance and mass of the two electrodes (Eqn. 5).

In a symmetric supercapacitor, a situation has been reported by several literatures [4-13] that the specific capacitance of two electrodes could be different since the behaviors of cation and anion are different in supercapacitors. As a result, one electrode will reach the potential limit sooner than the other. In such a case a range of potential on the opposite electrode will not be utilized in charging/discharging. Therefore, by adjusting the mass ratio of the two electrodes, the potential window for each electrode could be utilized fully – the operating voltage U on the device is also uplifted.

In the present study we have improved the pore structure of CNT/graphene compared with the ones we used in previous chapters by eliminating the pores accessible for neither cations nor anions, which are supposed to have negative effect on specific capacitance. It is realized by the better dispersion of CNTs in water by using a surfactant. And a greater working voltage has been achieved using unequal carbon nanotube (CNT)/graphene electrodes in ionic liquid 1-methyl-1-propylpiperidinium bis (trifluoromethyl sulfonyl) imide (MPPp-TFSI). When the ratio of m_- to m_+ was set to 1.5, the supercapacitor could be charged to 4.7 V and a high energy density of 118 Wh kg^{-1} was obtained at a charging/discharging current density of 1.0 A g^{-1}.

6.2. Experimental

Graphene oxide (GO) was synthesized from graphite using the Hummers' method [14]. Carbon nanotubes (CNTs) were dispersed in aqueous solution of sodium dodecylbenzenesulfonate (SDBS), which serves as the surfactant, by sonication. And GO was dispersed in deionized water by the same method. The mass ratio of CNTs to GO is 1/4. After mixing the two dispersions by sonication, CNT/GO composite was obtained and then was reduced by hydrazine at 98 ℃ for 24 hours. The reduced material was rinsed with deionized water for several times until it became neutral and SDBS removed. The CNT/graphene composite was eventually obtained as black powders. The schematic of the co-reduction is shown in Fig.2.

Scanning electron microscope (SEM, JEOL JSM-6500F) was used to observe the morphology of electrode materials. Surface chemistry of the electrode materials was characterized by x-ray photoelectron spectroscopy (XPS, ULVAC-PHI Quantera SXM) with a twin anode Al Kα x-ray source and hemispherical energy analyzer. The energies were calibrated against the aliphatic carbon C1s peak at 284.5 eV.

In order to find out the potential limitation on both the positive and negative electrode, the charging process was conducted using a three-electrode system with Pt as the counter electrode, silver-silver ion (Ag/Ag+) as the reference electrode, and SWNT/graphene composite as the working electrode. In order to reach designed values of U_+ and U_- at the same time, the charging-discharging process was performed using a three-electrode system with Ag/Ag+ as the reference electrode and CNT/graphene composite as both the positive and negative electrode.

All electrochemical characterization was carried out using an electrochemical workstation (Biologic VSP-300). The ionic liquid electrolyte used in our study, 1-methyl-1-propylpiperidinium bis (trifluoromethyl- sulfonyl) imide (MPPp-TFSI) with purity 99.9%, was purchased commercially from Toyo-Gosei. Graphite was purchased commercially from Alfa Aesar and CNTs were purchased from Cheap Tubes Inc. Other chemicals were purchased from Wako Pure Chemical Industries, Ltd.

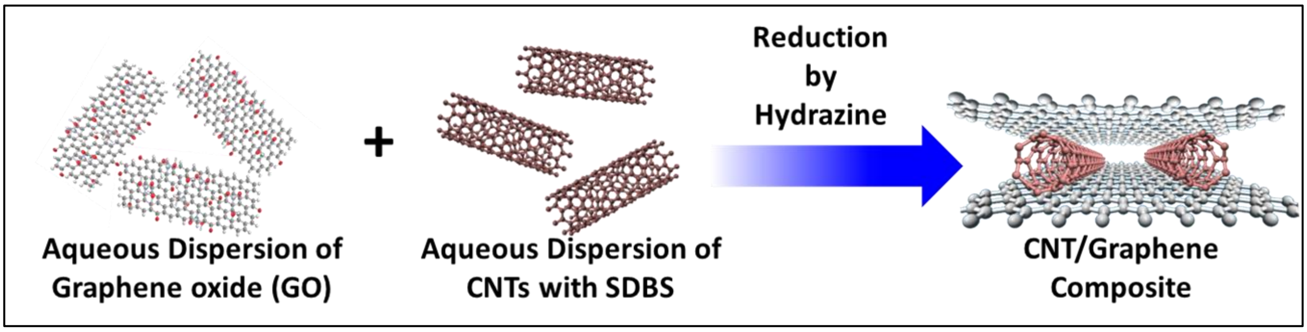

Fig.2 Schematic of co-reduction of CNT and GO

6.3. Results and Discussion

6.3.1 Characterization of Electrode Materials

After chemical reduction of the SWNT/GO composite, there remain some oxygen-containing functional groups on the surface of the SWNT/graphene composite according to XPS analysis (Fig 3). The existential forms were C-O (286.5 eV) and C=O (287.8 eV) [15]. The atomic ratio of oxygen to carbon (Table 1) is similar in CNT/graphene composite and RMGO-4 composite, indicating that we have realized the modification the pore structure without the change of chemical structures.

Table 1. Ratio of oxygen to carbon in materials characterized by XPS

Materials	Ratio of O to C (%)
CNT/graphene	12.5
RMGO-4	11.7

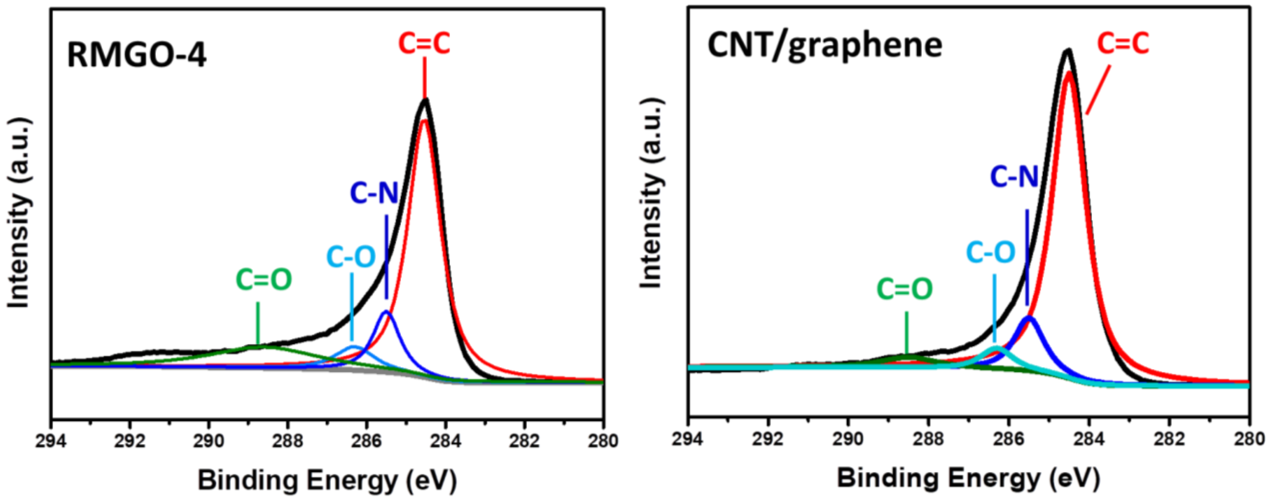

Fig. 4 C 1s spectra of XPS showing the chemical structures of RMGO-4 and CNT/graphene composites

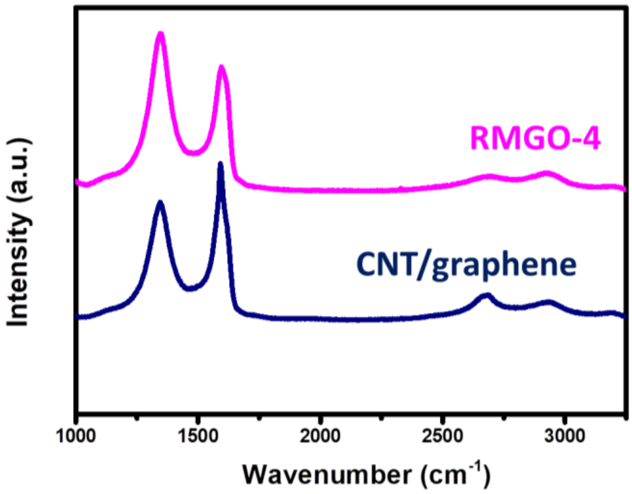

Fig. 4 Raman spectra of RMGO-4 (pink) and CNT/graphene (dark blue) composites.

Fig. 4 shows the Raman spectra of SWNT/graphene composite and RMGO-4 composite, which reflect the structural defects of materials. The ratio of intensity of D peak to G peak (I_D/I_G) is 0.73 and 1.27 in

SWNT/graphene and RMGO-4, respectively. The less defects in SWNT/graphene, which is indicated by the smaller value of I_D/I_G, is mainly due to the less defects on SWNTs since they are not oxidized before co-reduction process. Fig 5 shows the morphology of SWNT/graphene composite and RMGO-4 composite. The CNTs could be seen clearly in both of the two composite as indicated in the SEM image.

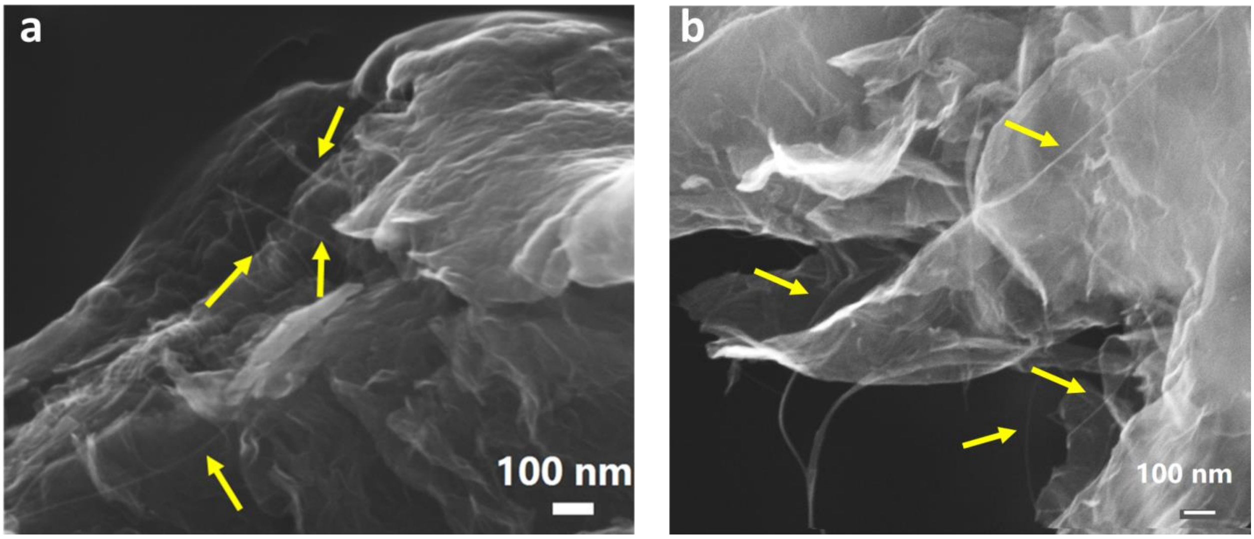

Fig.5 SEM image reveals the presence of CNTs in (a) RMGO-4 and (b) SWNT/graphene composite.

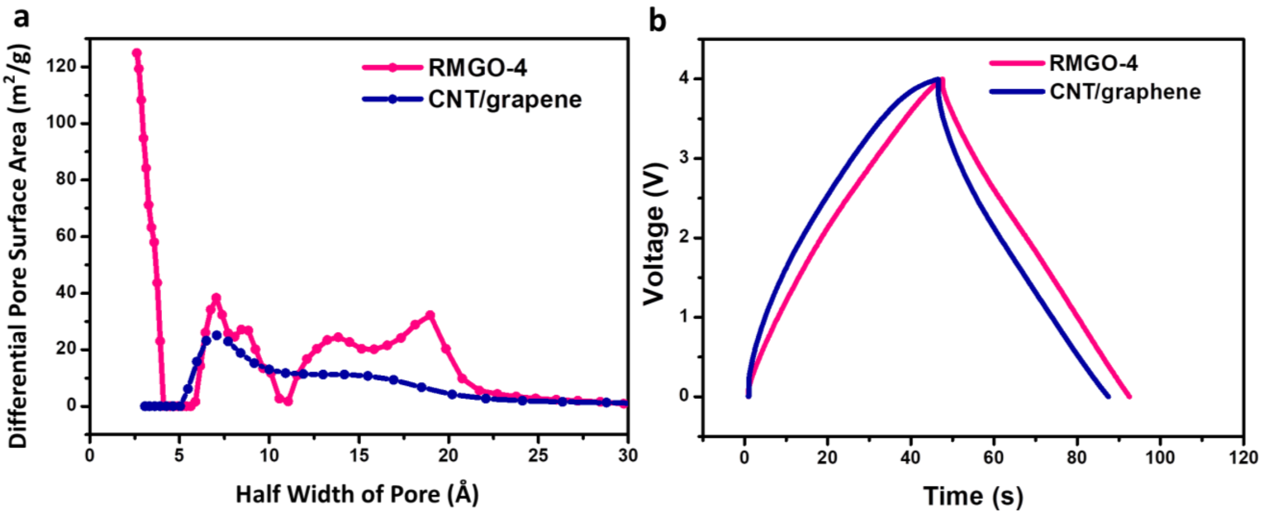

Fig. 6 (a) Pore distribution and (b) charging-discharging curves of RMGO-4 (pink) and CNT/graphene (dark blue). The current density is 1.0 A g^{-1} and the applied voltage is 4.0 V.

Compared with the reduced oxidized multi-wall carbon nanotube/graphene oxide (RMGO) composite, the pores smaller than 0.54nm are eliminated due to the well-dispersed CNTs (Fig 6a). Considering the analysis of ionic behaviors of MPPp-TFSI in pores with different sizes, the pores smaller 0.68nm are accessible for neither MPPp$^+$ nor TFSI$^-$. By decreasing pores in this range, we can decreases the negative effect of ink-bottle structure due to the inaccessible pores. The effect improved pore structure is reflected in the performance in MPPp-TFS as shown in Fig 6b and Table 2. The specific capacitance of RMGO-4 and

CNT/graphene is almost the same at 4.0 V and 1.0 A g^{-1} even though the specific surface area of CNT/graphene (219 m^2 g^{-1}) is much smaller than that of RMGO-4 (542 m^2 g^{-1}). However, it is worth noting that the pores in the range from 0.68 nm to 0.96 nm, which are mainly accessible for $MPPp^+$ rather than TFSI-, still exist in CNT/graphene composite. This kind of pores is possible to result in the unequal specific capacitance of cation and anion

Table 2. Specific Capacitance and Specific Surface Area of Electrode Materials

Electrode Materials	Specific Capacitance /F g^{-1}	Specific Surface Area /m^2 g^{-1}
CNT/graphene	46	219
RMGO-4	48	542

6.3.2 Potential Limits

The positive and negative potential limits were characterized separately by a charging process at current density of 0.2 A g^{-1}. As shown in Fig. 7, the positive potential limit was 2.45 V and the negative limit was –2.33 V. Therefore, the electrochemical window of electrode in MPPp-TFSI was 4.8 V, though it is still much smaller than the electrochemical stability window of MPPp-TFSI (5.8 V) as shown in Fig 1 (Chapter 5). The smaller electrochemical window of electrode materials is attributed to the reactions between MPPp-TFSI and the oxygen-containing groups in the CNT/graphene electrodes [16].

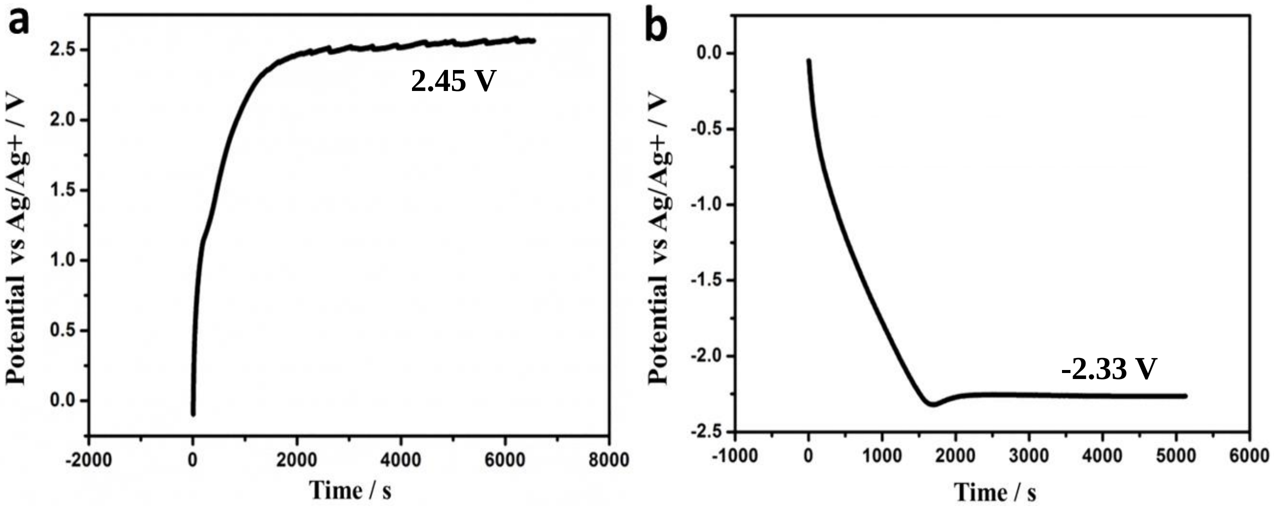

Fig. 7 (a) The positive and (b) negative potential limit measured in three-electrode system. The upper limit is 2.45 V and the lower limit is –2.33 V.

6.3.3 Underutilization of Potential Window in Symmetric Supercapacitor

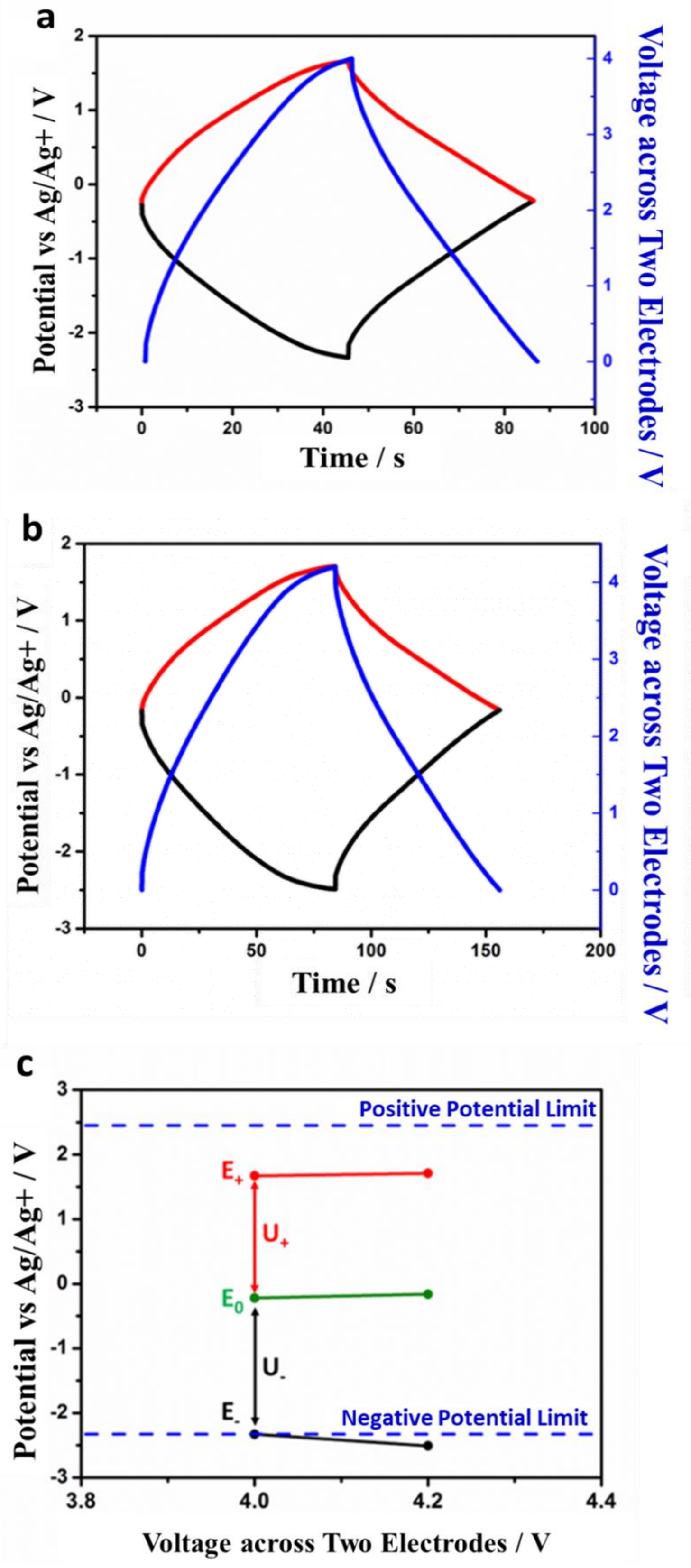

Fig. 8 Charge-discharge process of symmetric supercapacitors at (a) 4.0 V and (b) 4.2 V measured in three-electrode system. The current density is 1.0 A g^{-1}. (c) The positive potential (E_+) and negative potential (E_-) show that the largest working voltage of symmetric supercapacitor is 4.0 V because the negative electrode would reach first its lower limit.

We applied the charging/discharging process in a three-electrode system at 1.0 A g^{-1} as shown in Fig. 8. The values of U_+ and U_- were calculated using Eqn. 6:

$$U_+ = E_+ - E_0 \tag{6a}$$

$$U_- = E_- - E_0 \tag{6b}$$

in which E_+ and E_- are the anodic potential and cathodic potential, respectively, and E_0 is the potential of electrodes when the voltage between the positive and negative was zero. When the working voltage reached 4.0 V, the negative electrode would almost reach the potential limit though there was still a small gap between the positive potential and its upper limit, *i.e.*, the potential range from 1.67 to 2.45 V was not utilized. Even though the supercapacitor could be charged to 4.2 V, some reactions would be triggered because E_- (–2.51 V) exceeded the negative limit (–2.33 V). Since the smaller working voltage was due to the larger U_- (2.12 V) for the supercapacitor, we could lower it by increasing the mass ratio m_-/m_+ according to Eqn (5).

6.3.4 Different Capacitance of Positive and Negative Electrode

The unutilized potential range in the symmetric supercapacitor was due to the larger U_-, which was determined by larger C_{anion} as shown in Table 2. If the capacitance on the positive and negative electrode were solely due to the adsorption of anions and cations, respectively, this phenomenon means that the specific capacitance of the $MPPp^+$ layer is smaller than that of $TFSI^-$ layer. However, this conclusion is inconsistent with fitting results we mentioned in previous chapters in which C_{anion} should be the smaller one. This seemingly contradictory phenomenon may be attributed to different charging mechanism. As having reported in the literature, desorption of ions of the same charges and ion exchanges also existed in the charging process [12-18]. For example, Forse et al. reported that the electrolyte ions behaved differently on anode and cathode in Py13-TFSI, which has a similar structure to MPPp-TFSI [12]. The electrode capacitance would also be impacted when ions diffuse differently in MPPp-TFSI [16-18]. We suggest that the different charging mechanisms exist on the positive and negative electrode in our supercapacitors and it is one of the reasons causing the different capacitance on the two electrodes. More research is needed to validate this hypothesis and to find out the fundamental contributions to the different capacitance of each electrode.

6.3.5 Asymmetric Supercapacitor Using Unequal Electrodes

Table 3 shows the results of electrochemical characterization of supercapacitors with different ratio of electrode mass. The selected current density was 1.0 A g^{-1}, calculated basing on the total mass of two electrodes. When same voltage was applied on the supercapacitor, U_- was lowered with increasing ratio m_-/m_+. As a result, the supercapacitor using unequal electrodes could be charged to a voltage higher than 4.0 V before either the positive electrode or the negative electrode reached its potential limit.

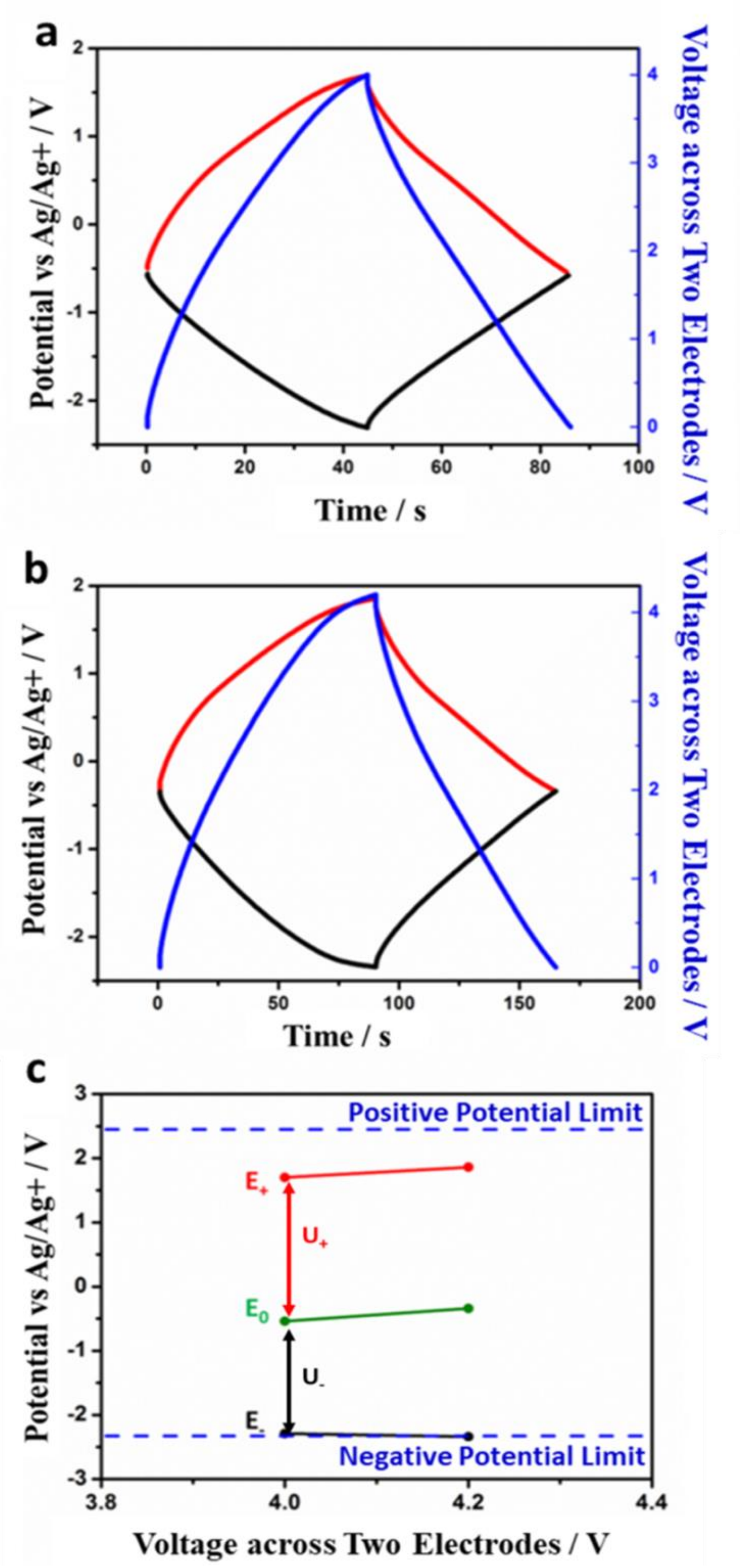

Fig. 9 Charge-discharge process of supercapacitor at (a) 4.0 V and (b) 4.2 V when electrode mass ratio m_-/m_+ is 4/3. The current density is 1.0 A g^{-1}. (c) The positive potential and negative potential show that U_- becomes smaller compared with symmetric configuration (Fig. 8). The largest working voltage of supercapacitor with this configuration is 4.2 V before the negative electrode reaches its limit.

Table 3 Electrochemical Characterizations of Supercapacitor with Different Electrode Mass Ratio of m_-/m_+.

m_-/m_+	Applied Voltage / V	U_- / V	U_+ / V	C_{cation} / F g^{-1}	C_{anion} / F g^{-1}
1 : 1	4.0	2.11 (-0.22 ~ -2.33)	1.89 (-0.22 ~ 1.67)	43	48
	4.2	2.35 (-0.16 ~ -2.51)	1.85 (-0.16 ~ 1.71)	71	77
4 : 3	4.0	1.74 (-0.54 ~ -2.30)	2.26 (-0.54 ~ 1.70)	45	48
	4.2	2.00 (-0.34 ~ -2.34)	2.20 (-0.34 ~ 1.86)	75	94
3 : 2	4.0	1.59 (-0.48 ~ -2.09)	2.41 (-0.48 ~ 1.90)	45	45
	4.2	1.80 (-0.37 ~ -2.17)	2.40 (-0.37 ~ 2.03)	83	93
	4.7	1.93 (-0.35 ~ -2.28)	2.77 (-0.35 ~ 2.42)	158	165

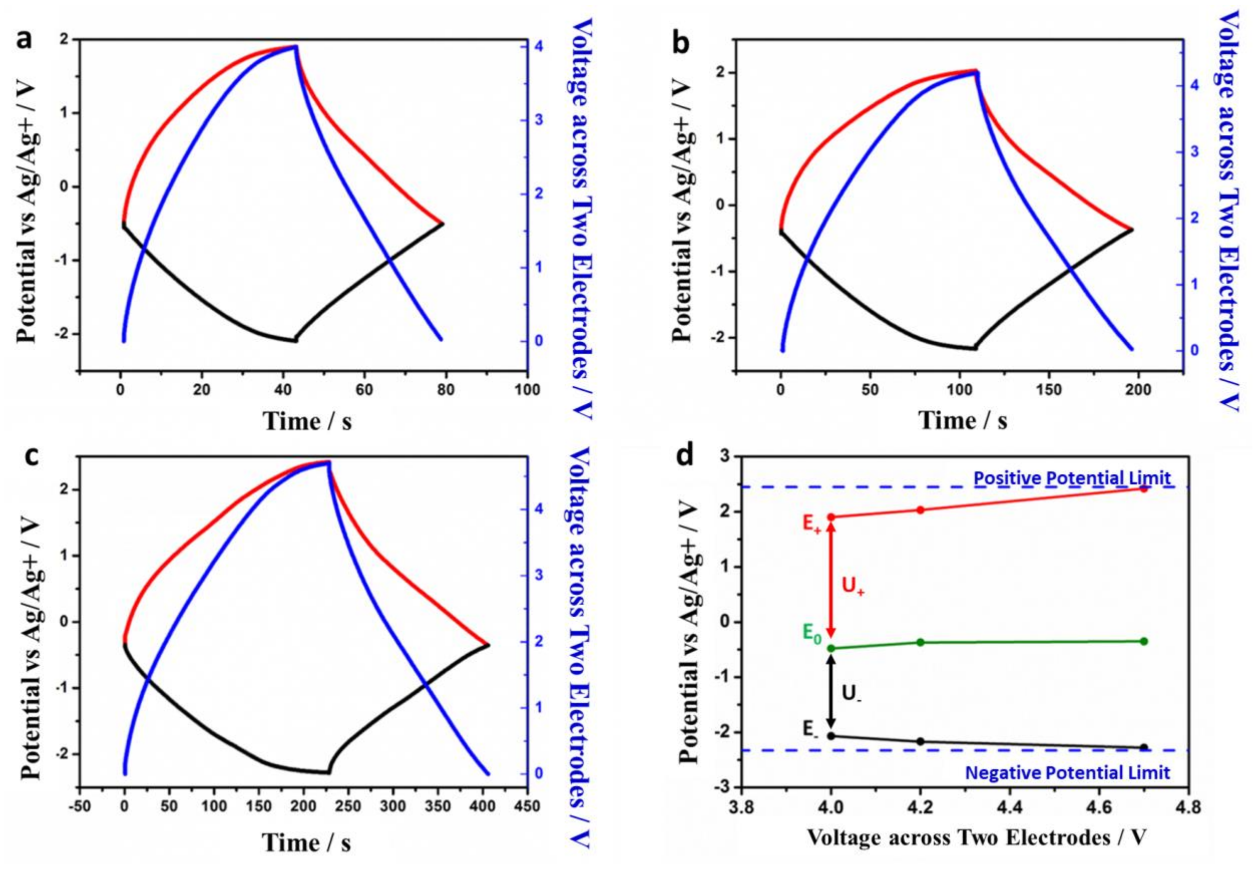

Fig. 10 Charge-discharge process of supercapacitor at (a) 4.0 V, (b) 4.2 V, and (c) 4.7 V with electrode mass ratio m_-/m_+ = 3/2. The current density is 1.0 A g^{-1}. (d) The positive potential and negative potential show further reduced U_- and the largest working voltage is 4.7 V, close to the electrochemical window of electrode materials (4.8 V).

Table 4 Energy Density of Supercapacitor with Different Electrode Mass Ratio of m_-/m_+

m_-/m_+	Energy Density (Wh kg^{-1})		
	4.0 V	4.2 V	4.7 V
1:1	25	45	-
4:3	25	50	-
3:2	24	52	118

For the supercapacitor with an electrode mass ratio of 4/3, the largest working voltage was 4.2 V. It is still smaller than the electrochemical window of the electrode materials (4.8 V) since the negative electrode would reach the lower limit before the positive electrode would its own upper limit (Fig. 9). When we further increased the electrode mass ratio from 4/3 to 3/2, the lowest potential of the negative electrode was changed from –2.34 to –2.27 V owing to the reduced U_- (Fig. 10b). The largest working voltage was therefore raised to 4.7 V when the electrode mass ratio was 3/2 (Fig. 10c) and the energy density was increased from 25 Wh kg^{-1} at 4.0 V in symmetric configuration to 118 Wh kg^{-1} at 4.7 V for the supercapacitor with unequal electrodes (Table 4).

The increased energy density due to improve pore structures and asymmetric configuration was shown in Fig 11a. The energy density of the asymmetric supercapacitor based on CNT/graphene at 4.5 V was 102 Wh kg^{-1}, increased by 85% compared with the symmetric supercapacitor based on RMGO-4. And the energy density could be further enlarged since the asymmetric CNT/graphene supercapacitor could be charged to 4.7V. The cycle stability of this asymmetric at 4.7V and 1.0 A g-1 was shown in Fig 11b. The retention ratio of energy density was 92% after 6000 cycles, indicating the good stability of our supercapacitors.

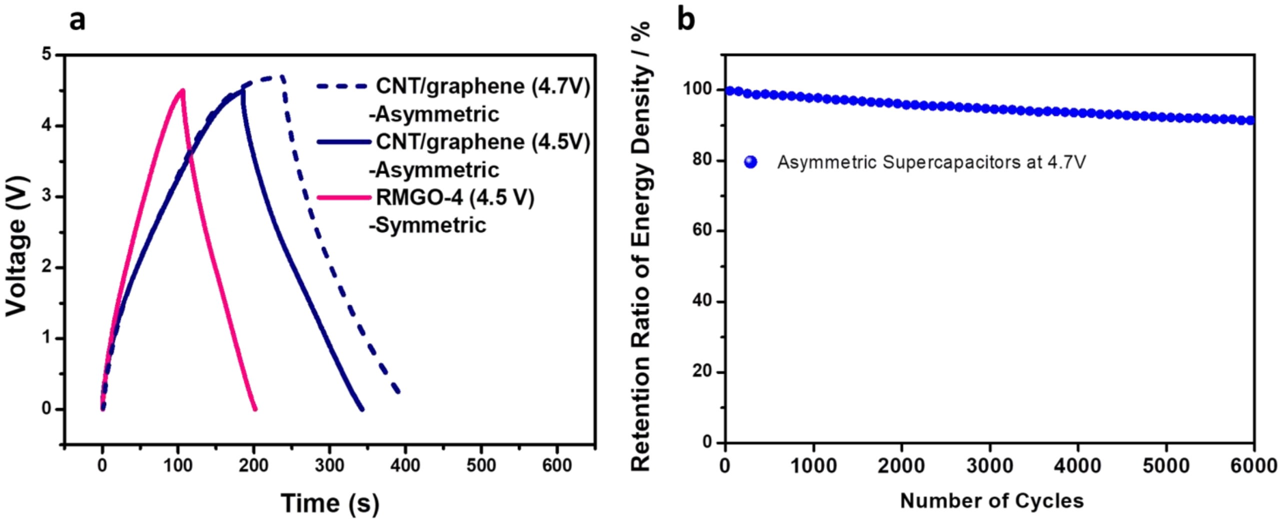

Fig. 11 (a) Charge-discharge curves of supercapacitors in MPPp-TFSI at 1.0 A g^{-1} and (b) the cycle stability of asymmetric supercapacitor measured at operation voltage of 4.7 V and current density of 1.0 A g^{-1}. The mass ratio of the electrodes is $m_-/m_+ = 1.5$. The retention ratio of energy density is 92% after 6000 cycles, indicating a good stability of the supercapacitor.

6.4. Conclusions

The pore structure has been improved in SWNT/graphene composite compared with RMGO composite since the pores smaller than 0.54 nm, which may have negative effects on specific capacitance, are eliminated. As a result, these two kinds of materials have the similar specific capacitance at 4.0 V even though the specific surface area of SWNT/graphene composite is much smaller than that of RMGO-4 composite.

The electrochemical measurement showed that the positive and negative electrostatic potential limits of SWNT/graphene electrode in MPPp-TFSI electrolyte were 2.45 and –2.33 V, respectively, and the electrochemical window of electrode materials in MPPp-TFSI was 4.8 V. However, the largest working voltage of symmetric supercapacitors using SWNT/graphene electrode is only 4.0 V due to the unutilized potential range on the negative electrode and unequal voltage on the positive and negative electrode are owing to the different specific capacitance of the two electrodes. According to the analysis of ionic behaviors in MPPp-TFSI in Chapter 5, the unequal specific capacitance is due to the pores (0.68 nm $< r < 0.96$ nm), which are mainly accessible for MPPp$^+$ rather TFSI$^-$.

To fully utilize the potential range for each electrode, we have optimized the respective voltage U_+ on positive electrode and U_- on negative electrode by adjusting the electrode mass ratio m_-/m_+. When the electrode mass ratio was changed from 1 to 1.5, the working voltage window was raised from 4.0 to 4.7 V and the energy density was increased from 25 to 118 Wh kg^{-1} with good cycle stability (92 %) by taking advantage of both higher working voltage and larger capacitance.

References

[1] C. Peng, S. Zhang, X. Zhou, and G. Z. Chen, “Unequalisation of electrode capacitances for enhanced energy capacity in asymmetrical supercapacitors,” *Energy Environ. Sci.*, vol. 3, no. 10, p. 1499, 2010.

[2] J. H. Chae and G. Z. Chen, “1.9 V Aqueous Carbon-Carbon Supercapacitors With Unequal Electrode Capacitances,” *Electrochim. Acta*, vol. 86, pp. 248–254, 2012.

[3] I. Pineiro-Prado, D. Salinas-Torres, R. Ruiz-Rosas, E. Morallon, and D. Cazorla-Amoros, “Design of Activated Carbon/Activated Carbon Asymmetric Capacitors,” *Front. Mater.*, vol. 3, no. March, pp. 1–12, 2016.*Frontiers in Materials*, 2016, 3, 16.

[4] D. Cericola, R. Kötz, and A. Wokaun, “Effect of electrode mass ratio on aging of activated carbon based supercapacitors utilizing organic electrolytes,” *J. Power Sources*, vol. 196, no. 6, pp. 3114–3118, 2011.

[5] P. Staiti, A. Arenillas, F. Lufrano, and J. Á. Menéndez, “High energy ultracapacitor based on carbon xerogel electrodes and sodium sulfate electrolyte,” *J. Power Sources*, vol. 214, pp. 137–141, 2012.

[6] E. G. Calvo, F. Lufrano, A. Arenillas, A. Brigandì, J. A. Menéndez, and P. Staiti, “Effect of unequal load of carbon xerogel in electrodes on the electrochemical performance of asymmetric supercapacitors,” *J. Appl. Electrochem.*, vol. 44, no. 4, pp. 481–489, 2014.

[7] M. Lazzari, F. Soavi, and M. Mastragostino, “High voltage, asymmetric EDLCs based on xerogel carbon and hydrophobic IL electrolytes,” *J. Power Sources*, vol. 178, no. 1, pp. 490–496, 2008.

[8] L. Xing, J. Vatamanu, O. Borodin, and D. Bedrov, “On the atomistic nature of capacitance enhancement generated by ionic liquid electrolyte confined in subnanometer pores,” *J. Phys. Chem. Lett.*, vol. 4, no. 1, pp. 132–140, 2013.

[9] M. D. Levi, N. Levy, S. Sigalov, G. Salitra, D. Aurbach, and J. Maier, “Electrochemical quartz crystal microbalance (EQCM) studies of ions and solvents insertion into highly porous activated carbons,” *J. Am. Chem. Soc.*, vol. 132, no. 38, pp. 13220–13222, 2010.

[10] W.-Y. Tsai, P.-L. Taberna, and P. Simon, “Electrochemical Quartz Crystal Microbalance (EQCM) Study of Ion Dynamics in Nanoporous Carbons,” *J. Am. Chem. Soc.*, vol. 136, no. 24, pp. 8722–8728, 2014.

[11] F. W. Richey, C. Tran, V. Kalra, and Y. A. Elabd, “Ionic liquid dynamics in nanoporous carbon nanofibers in supercapacitors measured with in operando infrared spectroelectrochemistry,” *J. Phys. Chem. C*, vol. 118, no. 38, pp. 21846–21855, 2014.

[12] A. C. Forse, C. Merlet, J. M. Griffin, and C. P. Grey, “New perspectives on the charging mechanisms of

supercapacitors," *J. Am. Chem. Soc*., vol. 138, no. 18, pp. 5731–5744, 2016.

[13] H. Sakaebe and H. Matsumoto, "N-methyl-N-propylpiperidinium bis(trifluoromethanesulfonyl)imide (PP13-TFSI) - Novel electrolyte base for Li battery," *Electrochem. commun*., vol. 5, no. 7, pp. 594–598, 2003.

[14] W. S. Hummers and R. E. Offeman, "Preparation of Graphitic Oxide," *J. Am. Chem. Soc*., vol. 80, no. 6, pp. 1339–1339, 1958.

[15] D. R. Dreyer, S. Park, C. W. Bielawski, and R. S. Ruoff, "The chemistry of graphene oxide," *Chem. Soc. Rev*., vol. 39, pp. 228-240, 2010.

[16] J. Li, J. Tang, J. Yuan, K. Zhang, Q. Shao, Y. Sun, and L.-C. Qin, "Interactions between Graphene and Ionic Liquid Electrolyte in Supercapacitors," *Electrochim. Acta*, vol. 197, pp. 84–91, 2016..

[17] W. Hsieh, T.-L. A. Horng, H.-C. Huang, and H. Teng, "Facile simulation of carbon with wide pore size distribution for electric double-layer capacitance based on Helmholtz models," *J. Mater. Chem. A*, vol. 3, no. 32, pp. 16535–16543, 2015..

[18] N. Terasawa and K. Asaka, "High performance polymer actuators based on single-walled carbon nanotube gel using ionic liquid with quaternary ammonium or phosphonium cations and with electrochemical window of 6 V," *Sensors Actuators B Chem.*, vol. 193, no. 0, pp. 851–856, 2014.

Chapter 7

Conclusions and Prospective

7.1. Conclusions

7.1.1 Carbon Nanotube/Graphene Composite with Adjustable Porous Structures as Electrode Materials in Supercapacitors

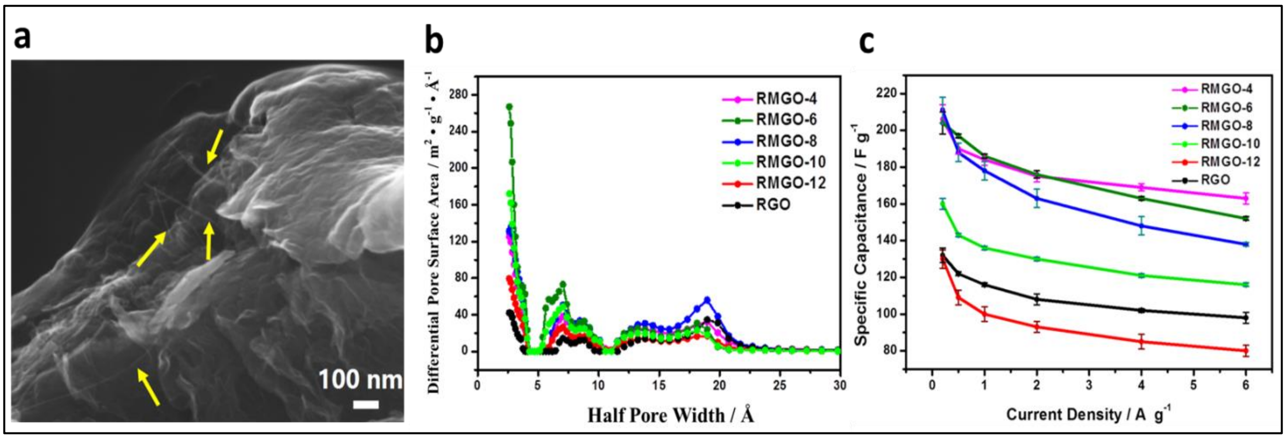

Fig. 1 (a) SEM image of RMGO-4, (b) pore distribution and (c) rate performance of RMGO composites. The current density in rate performance is from 0.2 to 6.0 A g^{-1} and the electrolyte is EMI-BF_4.

(1) CNT/graphene composites, designated as reduced oxidized MWNT/GO composite (RMGO), with different pore structures (Fig. 1a and Fig. 1b) are designed by adjusting the CNT/graphene mass ratios.

(2) The improved dispersity of oxidized MWNTs in water contributes to the enlarged specific surface area (A) of the resulting CNT/graphene composite. The value of A increases with the ratio of spacers until 1/16 and largest one from RMGO-6 is 742 m^2 g^{-1}.

(3) RMGO-4 shows a high specific capacitance of 206 F g^{-1} at current density of 0.2 A g^{-1} and the best rate capability with 79% capacitance retention at 6.0 A g^{-1} in an EMI-BF_4 electrolyte (Fig 1c), even though its specific surface area is smaller than that of RMGO-6. An explanation of this phenomenon is that the capacitance is also affected by pore distribution except for the specific surface area of total pores.

7.1.2 Ionic behaviors in Different Pores and Their Different Contributions to Specific Capacitance

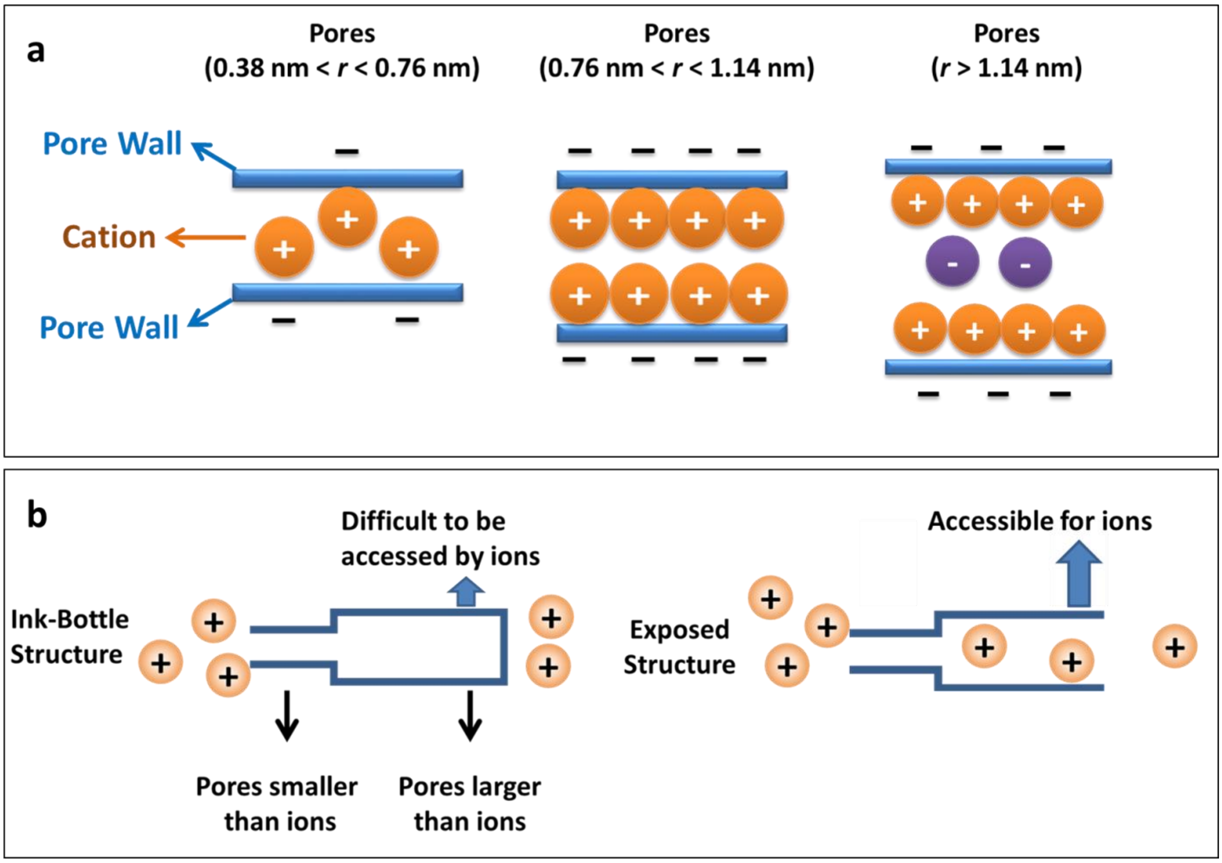

Fig.2 Schematic showing the influence of (a) ion packing and (b) ink-bottle structure on specific capacitance in pores with different sizes.

(1) The behaviors of EMI^+ and $BF4^-$ in pores with different sizes have been discussed by two kind of fitting method. The linear fitting between $C/A_{(0.38\ \mathrm{nm} < r < 0.76\ \mathrm{nm})}$ and $A_{(r > 0.76\ \mathrm{nm})} / A_{(0.38\ \mathrm{nm} < r < 0.76\ \mathrm{nm})}$ is based on the assumption that the behaviors of cation and anion is the same. While the multi-linear fitting between specific capacitance and specific surface area of different pores is applied for cation and anion separately.

(2) Combining the fitting results of the two methods, a model has been built that anions prefer to move in the form of ion-pairs while cations move as the isolated ions.

(3) For both cations and anion-pairs, pores with radii in the range of two to three times of cation and anion-pairs are the most efficient pores. It is due to the changed ion packing configuration in different pores (Fig 2a). In addition, pores smaller than the ion sizes could hinder the utilization of larger pores when the ink-bottle structure is present (Fig 2b).

7.1.3 Ionic behaviors in Different Pores at Different Voltage and Their Different Contributions to Specific Capacitance

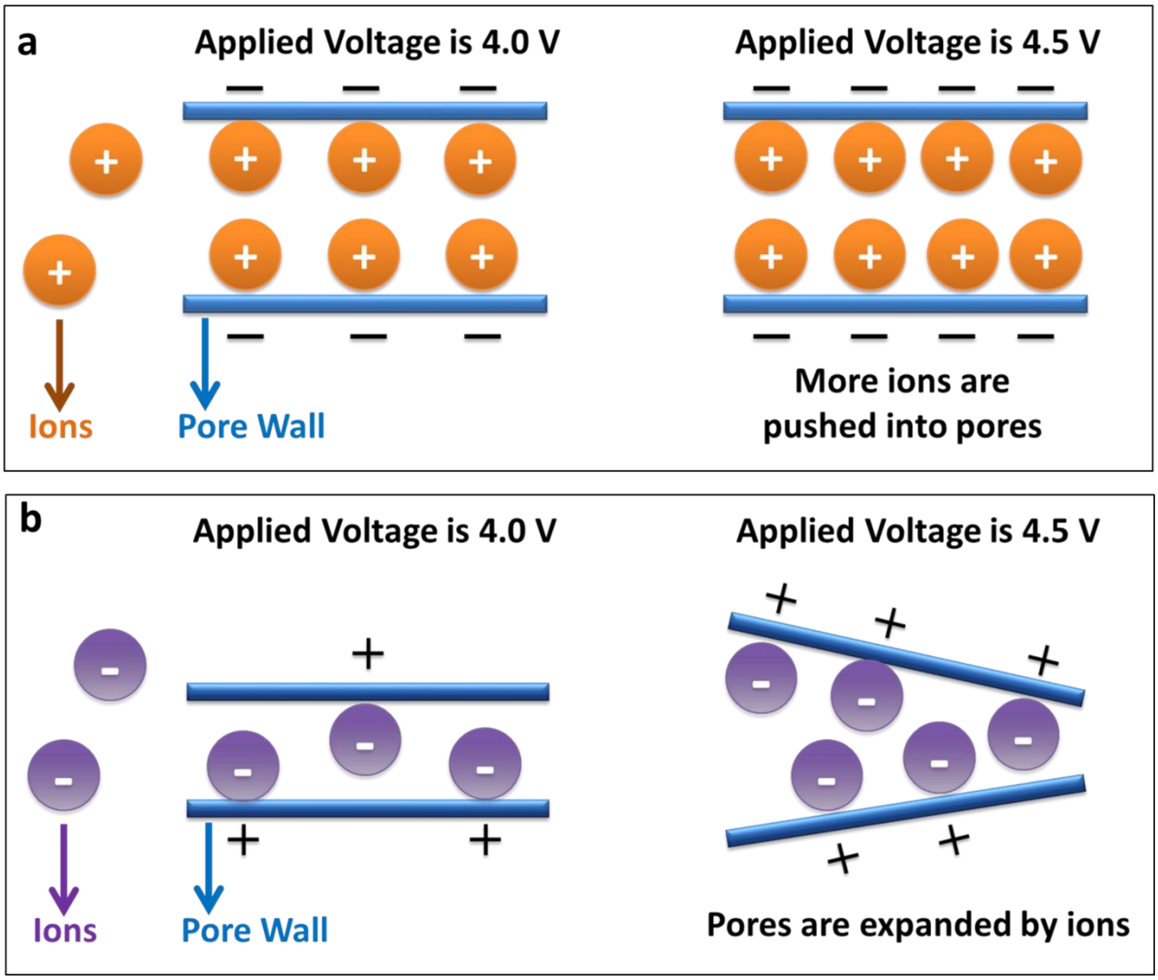

Fig. 3 Schematic of higher specific capacitance due to (a) more ions pushed into pores and (b) the expansion of pores forced by voltage.

(1) According to the results of multi-linear fittings, the most efficient pores for cations are pores (0.68nm < *r* < 2.5nm) while those are pores (0.96nm < *r* < 2.5nm) for anions. It is due to the existence of ion-clusters in MPPp-TFSI electrolyte due to its high viscosity.

(2) The changes of ionic behaviors when applied voltage increases have been figured out. For both cations and anions, more ions can be pushed into accessible pores by voltage. And for anions, some smaller pores can be expanded by anion-clusters forced by higher voltage (4.5 V). The two behaviors shown in Fig 3 are the reasons for the larger specific capacitance at the higher applied voltage of supercapacitors.

7.1.4 Enhancement of Energy Density of CNT/Graphene Supercapacitors by Improved Pore Structure and Asymmetric Configuration

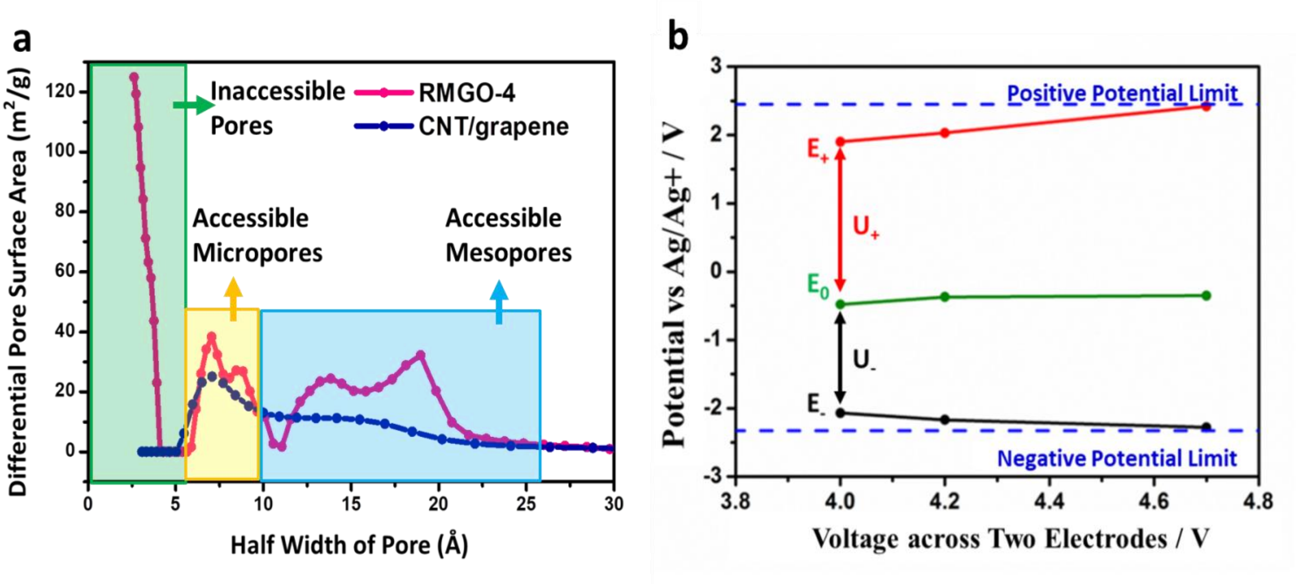

Fig. 4 (a) Pore distribution of CNT/graphene and RMGO-4 composites, and (b) voltage distribution of asymmetric supercapacitors when the mass ratio of two electrodes is 1.5.

(1) The pore structure has been improved in CNT/graphene composite compared with RMGO composite since the pores smaller than 0.54 nm, which may have negative effects on specific capacitance, are eliminated as shown in Fig 4a.

(2) The largest working voltage of symmetric supercapacitors using CNT/graphene electrode (4.0 V) is smaller than the electrochemical window of electrode in MPPp-TFSI (4.8 V) due to the unutilized potential range on the negative electrode owing to the different specific capacitance of the two electrodes.

(3) The largest working voltage of supercapacitors has been realized in a designed asymmetric configuration when the electrode mass ratio is 1.5 (Fig 4b). The working voltage window has been raised from 4.0 to 4.7 V and the energy density has been increased from 25 to 118 Wh kg^{-1} with good cycle stability (92 %) by taking advantage of both higher working voltage and larger capacitance.

7.1.5 Summary

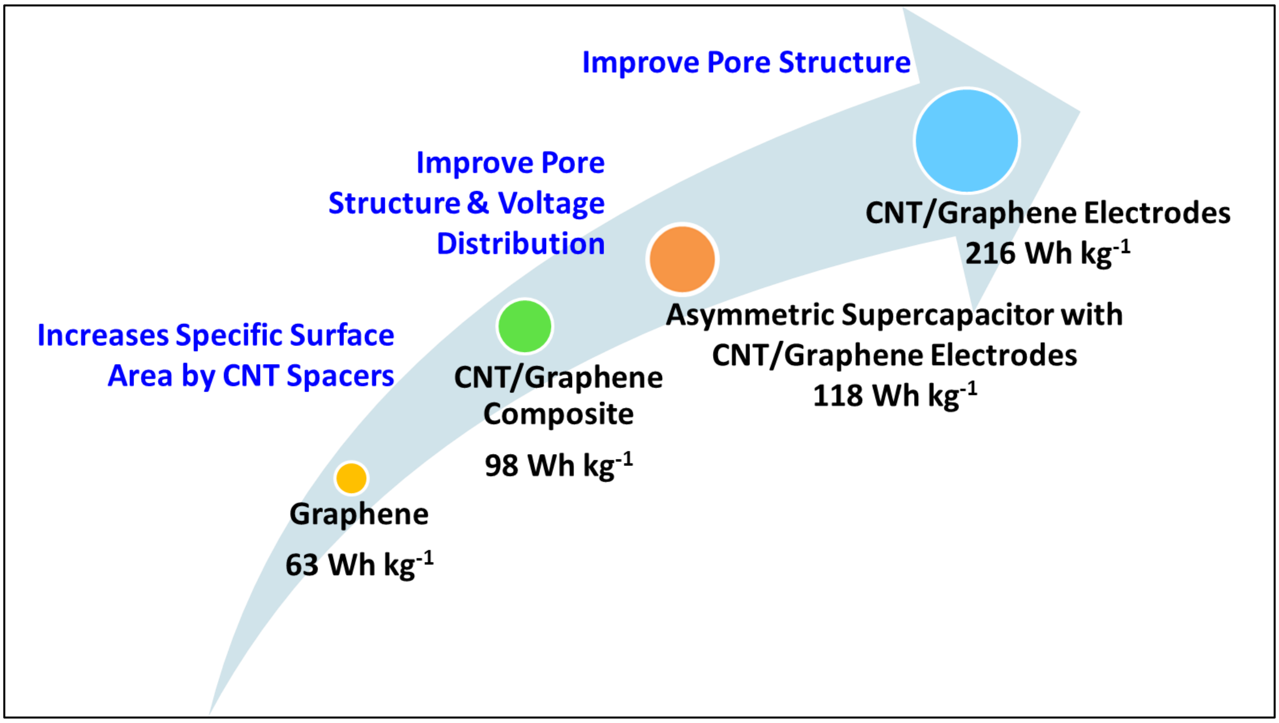

Fig. 5 Schematic showing the realization of high energy density in supercapacitors by improved CNT/graphene materials and designed asymmetric configuration. The improvement of materials is based on the clarified ionic behaviors in this study.

In this study, we firstly enlarge the specific capacitance of graphene-based electrode materials by using carbon nanotubes (CNTs) as spacers. The improved dispersion of CNTs treated by oxidization method has effectively prevented the aggregations between nanotubes. Subsequently, we have modified the pore structure of CNT/graphene composite according to the ionic behaviors in different pores, which has been figured out by the fitting analysis between various pore surface area and specific capacitance of different ions. The inaccessible pore, which may hinder the contribution of accessible pores, has been eliminated in the improved materials. Finally, the energy density has been enhanced by designing an asymmetric configuration of supercapacitors based on the improved CNT/graphene composite. The high energy density, 118 Wh kg^{-1}, is realized by both increased specific capacitance and the designed voltage distribution on electrodes (Fig. 5).

7.2. Future Prospect

The porous graphene composites have attracted tremendous attentions due to its potential in the application of energy storage. The study of ionic behaviors in supercapacitors and design of suitable pore structures of materials are two crucial points to improve the performance of supercapacitors based on porous graphene composites.

Since the methods we used to figure out the ionic behaviors are indirectly ones, more directly experimental tools will be explored in the future. Recently, nuclear magnetic resonance (NMR) method and quartz crystal microbalance (QCM) method have been applied in the investigation of ionic behaviors and charging mechanism in supercapacitors, which have provided some guidance for the future work in the field. For the design of pore structures, many methods have been developed to realize the more precise control of pore size, such as using templates and further improve the dispersion of spacers in shear flows. Combining the clarified ionic behaviors, the breakthrough in the performance of supercapacitors can be realized by the design of porous graphene composite with suitable pore structures. The supercapacitors with larger power density and enhanced energy density can be applied in many fields, such as the constitution of smart city.

Chapter 8

Achievements

8.1. Publications

1. J. Li, J. Tang, J. Yuan, K. Zhang, X. Yu, Y. Sun, H. Zhang, and L.-C. Qin, *" Porous carbon nanotube/graphene composites for high-performance supercapacitors"*, Chemical Physics Letters, 693, 60-65 (2018)
2. J. Li, J. Tang, J. Yuan, K. Zhang, Y. Sun, H. Zhang, and L.-C. Qin, *" Enlarging Energy Density of Supercapacitors Using Unequal Graphene Electrodes and Ionic Liquid Electrolyte ",* Electrochimica Acta, 258, 1053-1058 (2017)
3. J. Li, J. Tang, J. Yuan, K. Zhang, Q. Shao, Y. Sun, and L.-C. Qin, *"Interactions between Graphene and Ionic Liquid Electrolyte in Supercapacitors ",* Electrochimica Acta, 197, 84–91 (2016)
4. Q. Saho, J. Tang, Y. Sun, J. Li ,K. Zhang, J. Yuan, D.-M. Zhu, and L.-C. Qin, *"Unique interconnected graphene-SnO2 nanoparticle spherical multilayers for lithium-ion battery applications"*, Nanoscale, 9, 4439 (2017).
5. Y. Sun, J. Tang, F. Qin, J. Yuan, K. Zhang, J. Li, D.-M. Zhu, and L.-C. Qin, *“Hybrid lithium-ion capacitors with asymmetric graphene electrodes”* J. Mater. Chem. A, 5, 13601-13609 (2017)
6. Y. Sun, J. Tang, K. Zhang, J. Yuan, J. Li, D.-M. Zhu, K. Ozawa, and L.-C.Qin, *"Comparison of Reduction Products from Graphite Oxide and Graphene Oxide for Anode Applications in Lithium-ion Batteries and Sodium-ion Batteies "*, Nanoscale, 9, 2585-2595 (2016)
7. Q. Shao, J. Tang, Y. Lin, J. Li, F. Qin, K. Zhang, J. Yuan, and L.-C. Qin, *"Ionic Liquid Modified Graphene for Supercapacitors with High Rate Capability* "Electrochim. Acta 176 (2015) 1441-1446.
8. Q. Shao, J. Tang, Y. Lin, J. Li, F. Qin, J. Yuan, and L.-C. Qin, *"Carbon Nanotube Spaced Graphene Aerogels with Enhanced Capacitance in Aqueous and Ionic Liquid Electrolyte"*; Journal of Power Sources 278, 751-759 (2015)

8.2. Verbal Presentations

1. Jing Li, Jie Tang, Jinshi Yuan, Kun Zhang, Yige Sun, Lu-Chang Qin, *"A Study on Interactions between Ionic Liquids and Graphene-Based Electrodes",* Student Poster Presentation on Materials Research, Tsukuba Global Science Week, Tsukuba, Japan, Sep. 17, 2016

2. Jing Li, Jie Tang, Jinshi Yuan, Kun Zhang, Qingguo Shao, Yige Sun, Lu-Chang Qin, *"A Study on Interaction between Ionic Liquids and Electrodes in Graphene Supercapacitors"*, 2015 MRS Fall Meeting, Boston, USA, Nov. 29 – Dec. 4, 2015

3. Jing Li, Jie Tang, Feifei Zhang, Jinshi Yuan, Faxiang Qin, Lu-Chang Qin, *"The effect of oxidation time on performance of supercapacitor based on graphene"* , 23rd Annual Meeting of MRS-J, Yokohama, Japan, Dec. 9-11, 2013

4. Jing Li, Jie Tang, Feifei Zhang, Jinshi Yuan, Faxiang Qin, Lu-Chang Qin, *"The effect of oxidation time and size on performance of supercapacitor based on graphene"*, The Nanofiber Society, 4th Annual Meeting, Tsukuba, Japan, Jul. 5, 2013

8.3. Patents and Awards

1. 唐捷、張坤、李　婧、元金石、秦禄昌、新谷紀雄、「グラフェンとカーボンナノチューブとの積層体の製造方法、グラフェンとカーボンナノチューブとの積層体からなる電極材料、および、それを用いた電気二重層キャパシター」、公開日: 2017年9月28日、公告番号: WO2017163464 A1

2. 唐捷、張坤、リー ジン、松葉 頼重、畑 憲明、「二次元物質と繊維状物質の複合材料の製造方法」、公開日： 2017年6月29日、公告番号：WO2017110295 A1。

3. Best Presentation Award, Nanotechnology Students' Summer School 2015, Tsukuba, Japan, Jun. 29 – Jul. 2, 2015

Acknowledgements

I wish to express my deep sense of gratitude to my supervisor Prof. Jie Tang for her supervision throughout the three years' doctoral program. During the period of this study, Prof. Tang has devoted herself to instructing my research from designing the proposal to providing advices and composing the thesis. Her scientific spirit is a model of virtues for my career and life. And her innovation, expertise and generosity have encouraged me not only for my scientific research but also for my daily life. It is my honor to study and work in her group. Hence, I am taking the opportunity to giving my utmost thanks to her.

I really appreciate Prof. Lu-Chang Qin from North Carolina University at Chapel Hill for his guidance and advices throughout my graduated research. His invaluable comment, inspiriting and encouraging have guided me to deeper understanding of my study.

I also wish to express my sincere gratitude to all my group members, Dr. Han Zhang, Dr. Kun Zhang, Dr. Jinshi Yuan, Dr. Qingguo Shao, Dr. Yige Sun, Dr. Xiaoliang and Mr. Youcheng Zhang for their valuable assistance and suggestion. And I would like to give thanks to the secretaries of our group, Mrs Kawamura Yoiko and Mrs Furuzawa Sachiko for their kindly help.

I am highly indebted to my committee members: Prof. Kiyoto Matsuishi, Prof. Yoshihiko Takeda, and Prof. Kenji Sakurai.

Love and very special thanks to my parents, Mr. Shanchun Li and Mrs. Xiaoqing Yao, who are always supporting me with their selfless love.

This work was performed at Materials Processing Unit, National Institute for Materials Science and Graduate School of Pure and Applied Science of University of Tsukuba. Thanks for NIMS Junior Researcher Assistantship for supporting my research in Japan.